Synthesis and Characterization of Titania Nanotubes for Photocatalytic Water-Splitting and Carbon Dioxide Methanation

By

Elizabeth Grace Ranney

A dissertation submitted in partial fulfillment
of the requirements for the degree of
Doctor of Philosophy
(Chemical Engineering)
in the University of Michigan
2011

Doctoral Committee:

Professor Johannes W. Schwank, Chair
Professor H. Scott Fogler
Professor John W. Halloran
Professor Phillip E. Savage

To My Mom, Dad, Brother, and Husband

ACKNOWLEDGEMENTS

First, I would like to thank my committee for their wisdom and guidance throughout the last few years. I would like to especially thank my advisor, Professor Johannes W. Schwank for his advice and support throughout this journey. Professor Schwank has been an excellent mentor to whom I am extremely grateful. Next, I would like to thank the members of the Schwank lab for their ideas and encouragement. In particular, I would like to acknowledge Dr. Xiaoyin Chen , Dr. Andrew Tadd, Dr. Joseph Mayne, and Thomas Westrich for their insight.

I would like to acknowledge Dr. Lumin Wang, Dr. John F. Mansfield, and Dr. Kai Sun for teaching me about microscopy and for assisting me in the Electron Microbeam Analysis Laboratory. I would also like to thank Dr. Matthew W. Oonk for teaching me about thin film deposition. In addition, I would like to acknowledge the University of Michigan Lurie Nanofabrication Facility. I would also like to acknowledge Harold Eberhart, the Master Glassblower for the Department of Chemical Engineering, who fixed glassware for me. I would also like to thank Nicholas Kaylor with his assistance in the lab.

Next, I would like to thank my friends who have supported me throughout the years. In particular, I would like to thank Theresa Ledbetter, Joseph Cheng, Dr. Michael Senra, Dr. Joseph Mayne, Megan Mayne, Dr. Neil Schweitzer, and Amanda Hickman for their moral support.

I would like to thank my parents and my brother for their love and support. I can never thank them enough for their encouragement, wisdom, and insight. I am truly blessed to have them as my family. Finally, I would like to thank my husband for his love, support, and encouragement despite being 2,300 miles from me for the past four years. Thank you to my family and husband for walking along side me always.

TABLE OF CONTENTS

LIST OF FIGURES

Figure

LIST OF TABLES

Table

LIST OF APPENDICES

Appendix

ABSTRACT

As carbon dioxide emissions from coal-based electricity generation increase, new technologies are required to convert carbon dioxide to useable fuels, such as methane and hydrogen. The Sabatier reaction would be a useful method of reducing carbon dioxide emissions; however, the generation of the hydrogen needed for this reaction involves the use of fossil fuels. Therefore, a simultaneous method of generating hydrogen from non-fossil fuel sources and subsequent reduction of carbon dioxide to useable fuels, such as hydrogen and methane, is greatly desired. Metal-supported titania nanotubes are of particular interest due to their photocatalytic properties and high surface area for reactant adsorption. In particular, ruthenium-doped titania nanotubes are of interest because ruthenium is a highly active carbon dioxide methanation catalyst and titania offers a wide band gap.

In this study, the properties and photocatalytic activity of titania nanotubes are studied as a function of synthesis conditions. Using the anodic oxidation method, titania nanotube dimensions are tailored based on synthesis conditions. In addition, correlations between the synthesis conditions and oxygen content, conductivity, and photocatalytic activity of titania nanotubes are established. Titania nanotube formed in low fluoride-containing electrolytes exhibited high oxygen content, reduced conductivity, and superior photocatalytic activity.

Ruthenium-doped titania nanotubes are evaluated for use as a thermal catalyst for the Sabatier reaction and are compared ruthenium-supported alumina catalyst, the industry standard. A mechanism for simultaneous water-splitting and carbon dioxide methanation over Ru-doped titania nanotubes under UV light illumination is hypothesized based on Diffuse Reflectance Infrared Fourier Transform Spectrometry. Methane forms over Ru-doped titania nanotubes at 65°C under UV light illumination, which proves that water splitting and carbon dioxide methanation reaction can occur simultaneously over this photocatalyst.

Finally, the water-splitting reaction is evaluated over Ru-doped anatase titania, Ru-doped amorphous titania nanotubes, un-doped anatase titania nanotubes, Ru-impregnated Degussa P25, and un-doped Degussa P25 photocatalysts. The physical addition of activated carbon to a flow reactor resulted 44% hydrogen generation from photocatalytic water vapor splitting over 7 cm^2 of UV-illuminated Ru-doped titania nanotubes. This is a record photocatalytic conversion of water vapor to hydrogen in a non-microreactor, titania-based system.

Chapter 1

Introduction

In 2009, carbon dioxide created from fossil fuel combustion represented 79% of greenhouse gas emissions [1]. Since 1990, carbon dioxide emissions have been increasing by approximately 0.4% per year. This trend can be explained by an increase in the number of domestic industrial processes and the rising demand for electricity and transportation energy due to a growing population. Electricity generation alone accounted for 41% of carbon dioxide emissions in 2009.

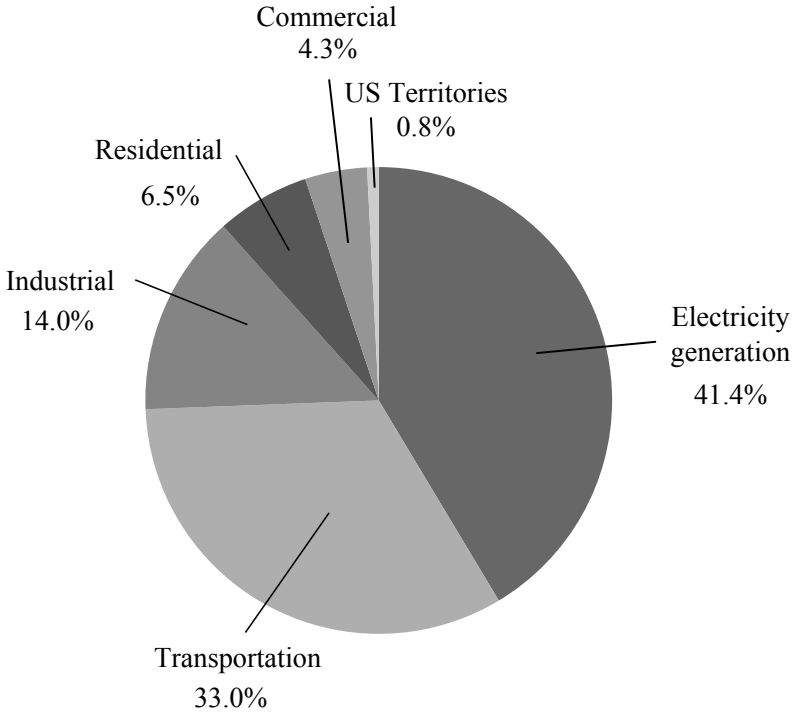

Figure 1.1: Breakdown of sources of carbon dioxide emissions generated fossil fuel sources. Electricity generation is the largest source of carbon dioxide emissions.

1.1 The Sabatier Reaction

The increase in greenhouse gas emissions has created a need for carbon capture and sequestration or for subsequent reduction of carbon dioxide to useable fuel. The Sabatier reaction (Equation 1.1) produces methane and water from carbon dioxide and hydrogen. The Sabatier reaction usually occurs above 200°C over a metal catalyst, such as nickel or ruthenium on an alumina support [2]. Ruthenium has been found to be more active than nickel for the Sabatier reaction [3]. If the carbon dioxide is used as a reactant in the Sabatier reaction, instead of being directly vented into the atmosphere, it not only can reduce carbon dioxide emissions, but it can be converted back to a useable fossil fuel for other processes. For example, if hydrogen is the desired fuel, methane can be used as a means of hydrogen storage.

$$CO_2 + 4H_2 \rightarrow CH_4 + 2H_2O \qquad (1.1)$$

The use of the Sabatier reaction presents a few technical challenges if it is to be used for carbon dioxide removal and methane generation in an energy-saving and economical way. The first problem is the creation of several byproducts from the Sabatier reaction. Carbon monoxide, solid carbon, and methanol are a few of the possible byproducts. Methanation catalysts are able to further convert these products to methane via other reaction pathways, but these products, especially solid carbon, can

deactivate the metal catalyst. Figure 1.2 shows product distribution of the Sabatier reaction as a function of reaction temperature.

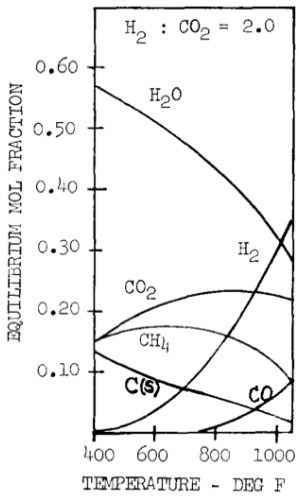

Figure 1.2: Product distribution of the Sabatier reaction as a function of reactor temperature for a 2:1 H_2 to CO_2 feed ratio over a 0.5 wt.% ruthenium on alumina catalyst. Image courtesy of Lunde, et al. [2]. The maximum production of methane occurs at 345°C. Carbon monoxide forms at 425°C and increases with temperature.

A second drawback of the Sabatier reaction is the use of a ruthenium-based catalyst for the Sabatier reaction. Ruthenium is a highly reactive methanation catalyst [2], but is expensive [3] and toxic. Nickel is also an active methanation catalyst, but also presents health hazards during its synthesis.

The third and most formidable problem is the creation of hydrogen for the Sabatier reaction. 95% of hydrogen is produced by steam reforming of fossil fuels, mainly methane, oil, or coal [4]. During steam reforming, the fossil fuel reacts with water under high temperatures and pressures to create hydrogen and carbon dioxide. Overall, fossil fuels, such as methane, would react with water to create hydrogen and carbon dioxide so that the hydrogen can then react with more carbon dioxide to form a

smaller amount of methane than was originally present. This circular reaction pathway is expensive and wasteful; thus, other methods of hydrogen generation must be conceived for the Sabatier reaction to be economically, energetically, and environmentally beneficial.

1.2 Alternative Methods for Hydrogen Generation

Alternative methods of hydrogen generation, such as water electrolysis, fuel cells, and photocatalysis, have been suggested. Photocatalytic water splitting for hydrogen generation has attracted interest since the use of solar energy as the only energy input would be both economically and environmentally sound. Extensive research has been done to study water splitting in photoelectrochemical cells over various catalysts, such as silicon nanowires, Pt-doped titania powder, and CdSe films on titania [5-7] as well as metal-doped titania nanotubes [8-9]. Photoelectrochemical cells present the challenge of oxygen and hydrogen separation. The highest reported water splitting rate in a titania-based photoelectrochemical cell is approximately 1.6 umol/min from liquid water [10].

Eder and coworkers demonstrated water splitting over iron and platinum co-doped anatase and rutile titania nanotubes immersed in liquid water and illuminated by ultraviolet (UV) light [11]. This work suggested the possibility of direct water splitting over a metal catalyst in essentially one half of a photoelectrochemical cell.

Photocatalytic water splitting using water vapor, instead of liquid water, is another area of interest since water vapor can be used in a single-phase continuous flow process. Photocatalytic water splitting typically occurs over metal-doped materials with a

band gap above 2.43 eV [12], the amount of energy required to split water. During photocatalysis, a photon excites an electron from the valence band to the conduction band. The hole (h^+) remaining in the valence band participates in the formation of oxygen and two protons (H^+) (Equation 1.2) and the two protons interact with excited electrons (e^-) to create hydrogen gas (Equation 1.3) [13].

$$2OH^- + h^+ \rightarrow O_2 + 2H^+ \quad (1.2)$$

$$2H^+ + 2e^- \rightarrow H_2 \quad (1.3)$$

In particular, a one-step simultaneous water splitting and carbon dioxide methanation process is desired. A single step process would not only be more economically and energetically efficient, but would allow for a water vapor feed, instead of a hydrogen feed, to the Sabatier reaction for the creation of methane. In addition, methane can be used for hydrogen storage since it is more transportable. So, methane can be the desired fuel or it can be further oxidized to form a hydrogen fuel.

Varghese and coworkers examined the use of solar light to split water in a batch reactor in the presence of carbon dioxide using platinum, copper, and nitrogen-doped titania nanotube arrays [14]. The resulting products measured were methane, hydrogen, and carbon monoxide in addition to trace amounts of branched paraffins and olefins. Zhang and coworkers simultaneously split water and reduced carbon dioxide to form methane using platinum-doped titania nanotubes in a quartz batch reactor illuminated by UV light [15]. Still, simultaneous water splitting and carbon dioxide methanation would be more useful as a continuous process, instead of a batch process, for operation in an

industrial setting. In addition, Schlögl and coworkers demonstrated enhanced methane production over ruthenium-impregnated titania powder catalyst illuminated by UV light, suggesting the possibility that the UV light used to split water may also increase methane production [16].

Several major hurdles also exist for photocatalytic water splitting. First, creating a material with an optimum band gap for water splitting is a challenging task that could involve thousands of combinations of materials. The recombination of holes and electrons takes less than one nanosecond [17], requiring that the redox reactions in Equations 1.2 and 1.3 also happen quickly. Optimizing the band gap of the material can maximize the number of excited electrons. Hydrogen and oxygen also can recombine to form water due to the short distance between molecules. In addition, the separation of oxygen from hydrogen proves to be challenging since they are both gaseous products. Another challenge presented by most current photocatalysts tested is their ability to only absorb photons from the UV range instead of the entire solar spectrum. Since the UV range represents only about 3% of the solar spectrum, photocatalytic water splitting by these photocatalysts will not be very efficient.

The first major obstacle for simultaneous water splitting and carbon dioxide methanation is the possible combustion of methane to re-form carbon dioxide since water splitting generates both oxygen and hydrogen. Since the reduction of carbon dioxide is desired, methods of preventing the oxidation of methane must be found for the simultaneous water splitting and Sabatier process to be useful.

The second major obstacle for combining photocatalytic water splitting and carbon dioxide methanation is finding operating parameters that allow both reactions to

occur simultaneously. The work done by Varghese and Zhang show that water splitting occurred at room temperature (~25°C) [14-15]. The Sabatier reaction can occur between 200°C and 800°C [2]. In addition, a material capable of catalyzing both reactions is desirable.

Ruthenium-doped titania has attracted attention as a possible water splitting and carbon dioxide methanation catalyst. In particular, titania nanotubes are studied due to their high surface area to volume ratio, which allows for more exposed titania and metal particle surface area. Ruthenium-doped titania nanotubes were found to be a possible water splitting catalyst based on band gap measurements above 2.43 eV and photocatalytic methylene blue decomposition experiments [13]. Ruthenium-impregnated titania powder has been shown to act as a methanation catalyst in previous work [16,18]. Ruthenium is both expensive and toxic, but titanium is abundant, inexpensive, and non-toxic. However, based on the work by Khan, Ru-doped titania nanotubes may have the ability to split water using visible light [13] and UV light based on the amount of ruthenium in the nanotube array. Since visible light represents 41% of the solar spectrum, the use of Ru-doped titania nanotubes would be more efficient.

1.3 Thesis Objectives

The focus of this thesis is to utilize and understand Ru-doped titania nanotubes for simultaneous water splitting and carbon dioxide methanation. Chapter 2 gives an overview the anodic oxidation method for forming titania nanotubes and the current work done to understand the effects of synthesis conditions on titania nanotube properties.

Chapter 3 outlines the fabrication techniques and equipment used. The focus of Chapter 4 is to describe the properties of titania nanotubes as a function of synthesis conditions. This step is important for predicting the dimensions and properties of the titania nanotubes after synthesis and for understanding the behavior of titania nanotubes when used as a photocatalyst. Chapter 5 describes the use of Ru-doped titania nanotubes for use in the Sabatier reaction and discusses Diffuse Reflectance Infrared Fourier Transform Spectrometry experiments for understanding the simultaneous water splitting and carbon dioxide methanation mechanism. Chapter 6 details the use of Ru-doped titania nanotubes for photocatalytic water splitting in a continuous flow reactor. This section describes a possible method for preventing the combustion of methane to increase hydrogen production from water splitting. Finally, Chapter 7 contains a summary and recommendations for future studies.

References

[1] Executive Summary of the Inventory of U.S. Greenhouse Gas Emissions and Sinks: 1990–2009.

[2] P. Lunde and F.L. Kester, Rates of Methane Formation from Carbon Dioxide and Hydrogen Over a Ruthenium Catalyst, *Journal of Catalysis* 30 (1974) 423-429.

[3] Wei Wang and Jinlong Gong, Methanation of carbon dioxide: an overview, *Frontiers of Environmental Science & Engineering* 5 (2011) 2–10.

[4] Wise, Jeff. "The Truth About Hydrogen," Popular Mechanics 1 November 2006. Available online http://www.popularmechanics.com/science/energy/next generation/4199381.

[5] Kuiqing Peng, Xin Wang, and Shuit-Tong Lee, Silicon nanowire array photoelectrochemical solar cells, *Applied Physics Letters* 92 (2008) 92-94.

[6] S. Sato and J.M. White, Photodecomposition of water over Pt/TiO_2 catalysts, *Chemical Physics* 72 (1980) 83-86.

[7] D.J. Miller and D. Haneman, Preparation of stable efficient CdSe films for solar PEC cells, *Solar Energy Materials* 4 (1981) 223-231.

[8] Susanta K. Mohapatra, Mano Misra, Vishal K. Mahajan, and Krishnan S. Raja, Design of a Highly Efficient Photoelectrolytic Cell for Hydrogen Generation by Water Splitting: Application of $TiO_{2-x}C_x$ Nanotubes as a Photoanode and Pt/TiO_2 Nanotubes as a Cathode, *Journal of Physical Chemistry* 111 (2007) 8677–8685.

[9] Siguang Chen, Maggie Paulose, Chuanmin Ruan, Gopal K. Mor, Oomman K. Varghese, Dimitris Kouzoudis, and Craig A. Grimes, Electrochemically synthesized CdS nanoparticle-modified TiO_2 nanotube-array photoelectrodes: Preparation, characterization, and application to photoelectrochemical cells, *Journal of Photochemistry and Photobiology A: Chemistry* 177 (2006) 177-184.

[10] Gopal K. Mor, Karthik Shankar, Maggie Paulose, Oomman K. Varghese, and Craig A. Grimes, "Enhanced Photocleavage of Water Using Titania Nanotube Arrays," *Nano Letters* 5 (2005) 91-95.

[11] D. Eder, M. Motta and A.H. Windle, Iron-doped $Pt–TiO_2$ nanotubes for photo-catalytic water splitting, *Nanotechnology* 20 (2009) 1-6.

[12] J.F.M. Oudenhoven, F.J.E. Scheijen and M.Wolffs Fundamentals of Photocatalytic Water Splitting, *Chemistry of Catalytic System 2: Photocatalysis* (2004).

[13] M. Alam Khan, Do Hung Han, O.-Bong Yang, Enhanced photoresponse towards visible light in Ru doped titania nanotube, *Applied Surface Science* 255 (2009) 3687–3690.

[14] O. Varghese, M. Paulose, T. LaTempa, and C.A. Grimes, High-Rate Solar Photocatalytic Conversion of CO_2 and Water Vapor to Hydrocarbon Fuels, Nano Letters 9 (2009) 731-737.

[15] Q.H. Zhang, W.D. Han, Y.J. Hong, J.G. Yu, Photocatalytic reduction of CO_2 with H2O on Pt-loaded TiO2 catalyst, *Catalysis Today* 148 (2009) 335–340.

[16] J. Melsheimer, W. Guo, D. Ziegler, M. Wesemann and R. Schlögl, Methanation of carbon dioxide over Ru/Titania at room temperature: explorations for a photoassisted catalytic reaction, *Catalysis Letters* 11 (1991) 157-168.

[17] J. Ovenstone, Preparation of novel titania photocatalysts with high activity, *Journal of Materials Science* 36 (2001) 1325-1329.

[18] Yvonne Traa and Jens Weitkamp, Kinetics of the Methanation of Carbon Dioxide over Ruthenium on Titania, *Chemical Engineering and Technology* 21 (1999) 291-293.

Chapter 2

Background on Titania Nanotubes

Titania nanotubes are of particular interest due to their applications in gas sensing, solar cells, lithium ion batteries, and photocatalysis. Titanium is a stable, non-corrosive, abundant, and relatively low cost material that can be easily oxidized [1]. Titania is a photosensitive material in the UV range (320-400 nm) and offers a wide band gap (3.2 eV). These properties are highly beneficial in gas sensing and photocatalytic water splitting applications. In addition, if placed at the anode of a lithium ion battery, titania would allow for rapid discharge rates due to its favorable lithium ion intercalation properties [2-6].

A nanotube structure is highly desirable due to its high surface area to volume ratio. In the area of gas sensing, this high surface area could allow for greater sensitivity to target gases. In the area of photocatalytic water splitting, the increased area would allow for greater hydrogen generation and the nanotube walls allow for physical pathways for electron mobility [7]. Finally, a nanotube structure could increase the lithium ion capacity in batteries while providing physical pathways for ion transport.

2.1 Synthesis Methods

Of the several ways to synthesize titania nanotubes, the anodic oxidation method of preparation is used because it creates arrays of aligned nanotubes perpendicular to a substrate surface. Titania nanotubes formed by anodic oxidation are closed at the bottom and open at the top, which is the surface of the array. Variation in electrolyte composition, pH, anodization temperature, and electric potential allows for control of the nanotube dimensions. Other popular titania nanotube synthesis techniques are the sol-gel method and various templating methods. In the case of the sol-gel technique, nanotubes form in a powder form by hydrolysis of titanium (IV)-isopropoxide or titania powders, such as Degussa P25 titanium dioxide, in a water and acid solution [8-9]. Templating methods typically use nanowires as templates around which titania structures can be formed. This work, however, employs the anodic oxidation method for synthesizing titania nanotubes.

Titania nanotubes can be created by anodic oxidation from titanium foils or in thin titanium films, usually below 1 μm in thickness, deposited on substrates. Titanium foils can be of any thickness, but the synthesis conditions instead of the foil thickness determine the length of the titania nanotubes. DC-magnetron sputtering and E-beam evaporation are the two most common methods of titanium thin film deposition onto substrates prior to titania nanotube synthesis. Two common substrates used are silicon wafers and glass, although other substrates can be used. DC-magnetron sputtering has been used to form thin titanium films on silicon wafers and subsequently created titania

nanotubes from the thin titanium film [10-12]. When sputtering, the substrate and titanium are placed between two electrodes in a chamber under vacuum. Argon is then introduced into the chamber and a radio frequency (RF) source ionizes the argon to form plasma. The ions collide into titanium atoms, removing them from the target and depositing them onto the substrate.

When using the E-beam evaporation technique, a titanium source is heated by an electron beam under high vacuum. The titanium evaporates and deposits onto a substrate. The method of evaporation creates a smoother, more uniform surface than the sputtering method of thin film deposition. A smooth titanium film is more desirable for forming uniform titania nanotube arrays via anodic oxidation. In addition, the titanium surface created by E-beam evaporation is less dense than the surface created by DC-magnetron sputtering.

During the anodic oxidation method, titania nanotubes are prepared by applying an electrical potential through an electrolyte between a cathode, titanium, and an anode, usually a conductor such as copper or platinum. The electrolyte is typically composed of aqueous hydrofluoric acid, sodium fluoride, or ammonium fluoride and glycerol or ethylene glycol. Glycerol or ethylene glycol is usually added to increase the smoothness of the nanotube walls since they act as a buffer against the changing pH at the opening of the nanotube during synthesis [13]. Fluoride-containing electrolytes are used most commonly, although it has been shown that hydrochloric acid can be used instead to form nanotubes of similar dimensions and properties [7]. The use of hydrochloric acid is a preferred alternative to hydrofluoric acid due to safety issues associated with hydrofluoric acid, but other fluoride compounds are also safe alternatives.

Platinum is used most commonly as a cathode for anodic oxidation, although other materials such as palladium, carbon, tantalum, aluminum, tin, copper, cobalt, iron, nickel, and tungsten have successfully been used. Platinum and palladium are the most stable cathodes since they are the most resistant to the chemical conditions of the electrolyte and the applied electrical potential. The cathode material can also affect the photocatalytic properties of the titania nanotubes. Iron, cobalt, palladium, and carbon cathodes resulted in titania nanotubes with higher photocurrent efficiencies than tantalum, aluminum, tin, copper, nickel, tungsten, and platinum [14].

Titania nanotubes can also be used as a metal support when doped with other materials, such as carbon, gold, silver, platinum, and ruthenium, to functionalize them for thermal catalytic and photocatalytic applications. The most common method of doping titania nanotubes is wetness impregnation followed by a reducing step to result in small metal particles or true "doping" of the titania nanotubes.

2.2 Formation of Titania Nanotubes by Anodic Oxidation

The first step in the creation of titania nanotubes is the growth of an oxide layer on the titanium sheet according to the following reactions [11]:

$$2H_2O \rightarrow O_2 + 4e^- + 4H^+ \quad (2.1)$$

$$\underline{Ti + O_2 \rightarrow TiO_2} \quad (2.2)$$

$$\text{Total:} \quad Ti + 2H_2O \rightarrow TiO_2 + 4H^+ + 4e^- \quad (2.3)$$

The height of the oxide layer can be calculated using Equation 2.4 [15]:

$$h_{ox,i}(t) = \frac{\eta A_{ox}}{\rho_{ox} z F S_i} \int_0^t J_i(t) dt \tag{2.4}$$

where h_{ox} is height of oxide layer, η is the current efficiency (part of total current consumed in oxidation), A_{ox} is the oxide molar mass, ρ_{ox} is the oxide density, z is the number of electrons participating in the oxidation, F is Faraday's constant, S_i is the area of oxidized surface, and $J_i(t)$ is the current density as a function of time. Figure 2.1 is a scanning electron micrograph of the oxide layer that is formed during this step.

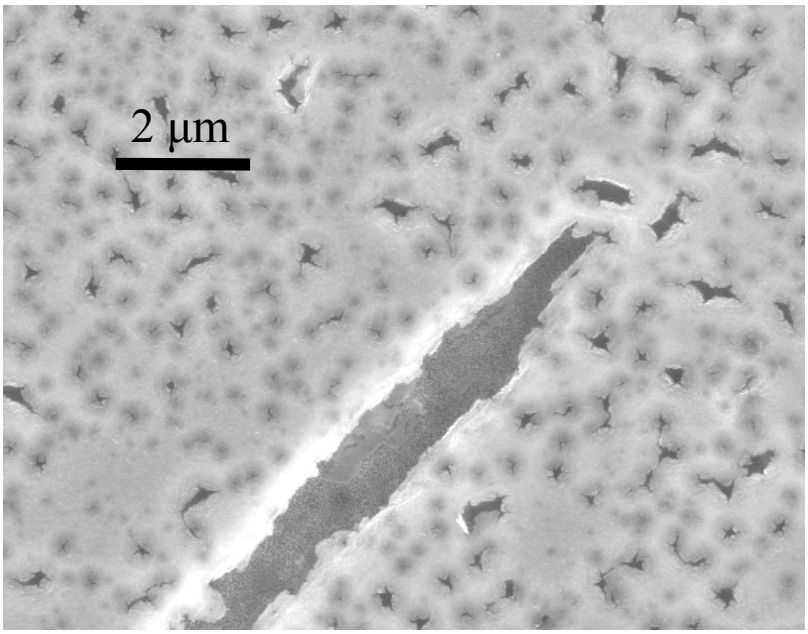

Figure 2.1: Scanning electron micrograph of the oxide layer formed during the first step of titania nanotube synthesis.

The next step after the formation of an oxide layer is pit formation. Pit formation begins on the oxide surface according to Equation 2.5 [11]. The pits expand to form pores that spread uniformly over the surface. In the case of thin Ti films, the smoother surface allows for greater uniformity of the pores and eventually the nanotube array.

$$TiO_2 + 6F^- + 4H^+ \rightarrow TiF_6^{2-} + 2H_2O \quad (2.5)$$

The last step is nanotube growth. Fluoride ions continue to bore into the titania to create tubes perpendicular to the surface. The electric field at the top of the tubes increases until pits, pores, and etching begins to create the voids between the nanotubes. The voids and tubes must grow in equilibrium to form an organized nanotube array [11]. Figure 2.2 is a schematic showing the top and side views of the titania nanotubes and voids.

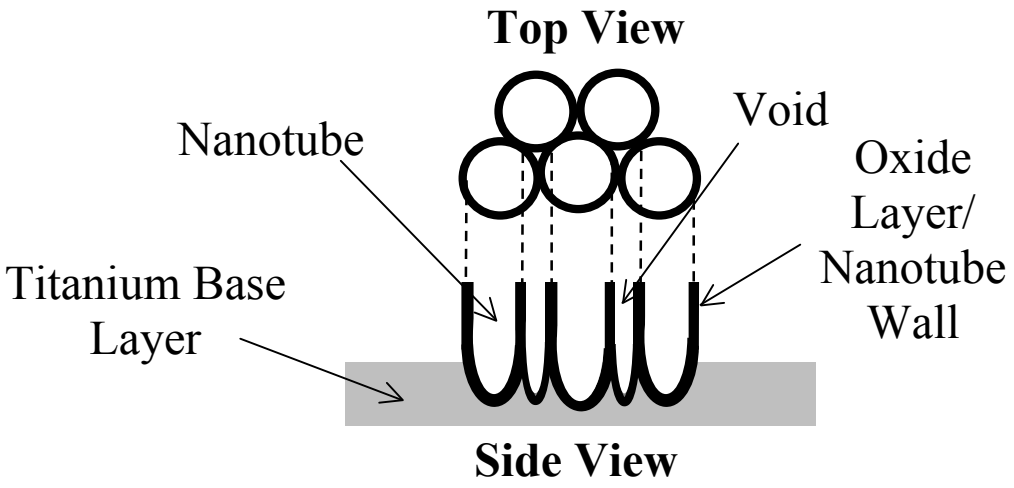

Figure 2.2: Diagram of the top view and side view of titania nanotubes and voids between the nanotubes formed during synthesis.

The dissolution of the oxide layer and creation of a new oxide layer allows for uniform wall thickness during the formation of the titania nanotubes. The reaction kinetics for oxide layer and nanotube formation are governed by the applied electric current and by the components of the electrolyte.

The titania nanotube synthesis process can be monitored by measuring the resulting current through the electrodes. Since the oxide layer is less electronically conductive than the titanium substrate, its formation can be observed by an exponential decrease in current [16]. After the oxide layer is formed, its dissolution and the formation of pits and pores is indicated by a slight increase in current since less of the oxide layer exists making the anode more conducting [16]. Finally, nanotube growth is denoted by a sharp decrease in the current followed by a slow, steady decrease in the current as oxide formation and dissolution occur at similar rates. When the nanotubes reach their maximum length, which is a length determined by the titanium substrate and electrolyte, the current begins to increase as the tops of the nanotubes begin to erode. Figure 2.3 is an illustration of the current during the titania nanotube synthesis process.

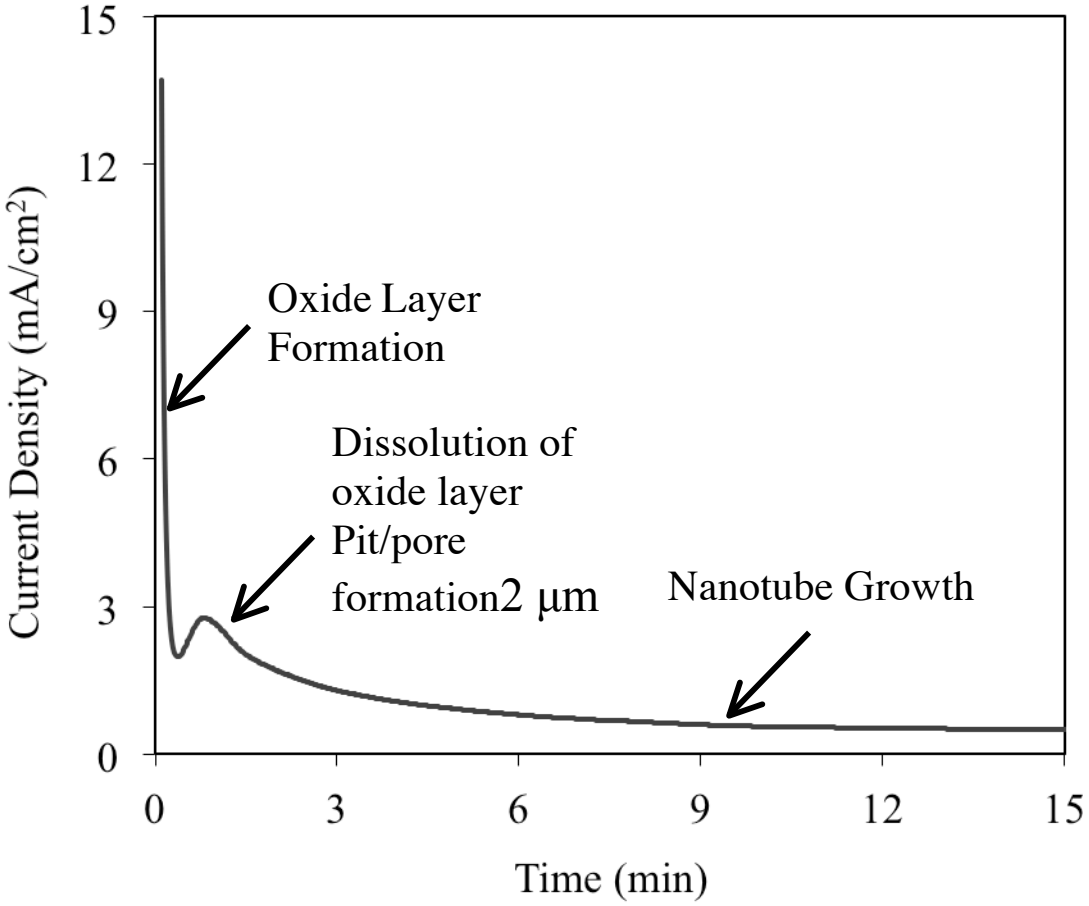

Figure 2.3: Measured current density due to the applied electrical potential as a function of time during the anodic oxidation process for titania nanotube synthesis. The oxide layer formation, dissolution of the oxide layer and pit/pore formation, and nanotube growth can be observed by measuring the current density.

2.3 Previous Work

Extensive studies have been done to correlate the anodic oxidation synthesis conditions with the dimensions and properties of titania nanotubes. The three most common variables in titania nanotube synthesis that have been studied are the electrolyte composition, applied electrical potential, and the anodization temperature. Kaneco and coworkers determined that adding methanol to an aqueous hydrofluoric acid electrolyte

can help to control the dimensions and number density of titania nanotubes [17]. Zhao and Xie studied the effect of adding phosphoric acid to an aqueous hydrofluoric acid electrolyte and observed that nanotubes formed from Ti foil [18-19]. Viscous electrolytes are preferred for nanotube synthesis since they can lower ion mobility at the opening of the nanotube to reduce local pH fluctuations to create a more homogeneous titania nanotube array. The longest nanotubes were formed from an electrolyte containing ammonium fluoride and a glycerol and water mixture, although ethylene glycol in water could also be used [13]. In this study, an aqueous sodium fluoride and glycerol electrolyte is used to study the direct effect of fluoride content and pH.

The applied electrical potential can also play a role in determining the dimensions and properties of titania nanotubes. A specific range of electrical potentials can be applied to form titania nanotubes depending on the synthesis electrolyte. For example, using an acetic acid, hydrofluoric acid, and water-containing electrolyte, titania nanotubes could only form using an applied electrical potential between 3-23 V. In addition, conical titania nanotubes could be formed if the applied electrical potential is increased at a constant rate during the synthesis process [11].

Electrolyte temperature during anodization has also been studied. Macak and coworkers determined that titania nanotubes could only form if the electrolyte temperature was between 0-40°C [13]. The Mor group observed that the titania nanotube wall thickness increased with decreasing anodization temperatures [11]. Titania nanotubes synthesized at 5°C were found to exhibit greater photocurrent density than titania nanotubes synthesized at higher temperatures [20]. The greater wall thickness caused by the lower anodization temperature allowed the nanotubes to absorb more

incident protons as measured by photocurrent density. This finding directly tied the synthesis conditions of titania nanotubes to their photocatalytic properties and suggests that titania nanotubes can be tailored to specific applications.

Some groups have also done some preliminary work to study the applicability of titania nanotubes in useful systems. Mor and coworkers have researched the ability of titania nanotubes to perform in a gas sensing system. This group demonstrated that the absorption and desorption of hydrogen gas can be measured by the change in resistance across a titania nanotube array. The nanotube array was able to detect hydrogen quickly and at room temperature without hysteresis. The Mor group also studied the use of light in cleaning gas sensors. Using titania nanotubes as a gas sensor, the researchers used ambient light to remove target gases from the array [11].

Ong and coworkers studied titania nanotubes in a solar cell application by performing a finite-difference time domain simulation. They found that a titania nanotube array serving as a negative electrode is applicable in solar cells. This group also determined that longer nanotubes are advantageous for this use [21]. Lee and coworkers studied the photocatalytic efficiency of TiO_2 nanotubes made by anodic oxidation in viscous electrolytes. This group characterized the resulting nanotubes using X-ray diffraction patterns and the photocatalytic efficiency using ultraviolet light irradiation. This work showed that viscous electrolytes allowed nanotubes to form without dissolving rapidly in solution and concluded that photocatalytic TiO_2 nanotubes are dependent on crystal structure [22].

Research has also been done to determine the lithium ion storage abilities of titania for battery applications. In particular, Hardwick and coworkers electrochemically

inserted lithium ions into anatase titania powders. This group investigated the phase change caused by lithium insertion/desertion and showed the cycleability of lithium ions in titania [23]. Also, Li and coworkers studied the ability of anatase titania nanotubes to store and release lithium ions. This group found that an anatase structure allows for a large lithium ion capacity and increased cycleability [24].

Titania nanotubes doped with metals such as gold, platinum, and ruthenium have been considered for thermal catalytic and photocatalytic applications. Titania nanotubes have been doped with gold and platinum by wetness impregnation to catalyze the oxidation of acetaldehyde [25]. Photocatalytic water splitting has been demonstrated using platinum, copper, and nitrogen dopants in titania nanotubes followed by carbon dioxide methanation [26-27].

References

[1] Meng Ni, Michael K.H. Leung, Dennis Y.C. Leung, K. Sumathy, A review and recent developments in photocatalytic water splitting using TiO_2 for hydrogen production, *Renewable and Sustainable Energy Reviews* (2005).

[2] P. Poizot, S. Laruelle, S. Grugeon, L. Dupont, J.M. Tarascon, Nano-sized transition metal oxides as negative-electrode materials for lithium-ion batteries, *Nature* 407 (2000) 496.

[3] Junrong Li, Zilong Tang, Zhongtai Zhang, Preparation and Novel Lithium Intercalation Properties of Titanium Oxide Nanotubes, *Electrochemical and Solid-State Letters* 8 (2005) A316-A319.

[4] H. Huang, W.K. Zhang, X.P. Gan, C. Wang, L. Zhang, Electrochemical investigation of TiO_2/carbon nanotubes nanocomposite as anode materials for lithium-ion batteries, *Materials Letters* 61 (2007) 296-299.

[5] Fangyi Cheng and Jun Chen, Storage of hydrogen and lithium in inorganic nanotubes and nanowires, *Journal of Materials Research* 21 (2006) 2744-2757.

[6] Mitsuhiro Hibino, Keiko Abe, Masafumi Mochizuki, Masaru Miyayama, Amorphous titanium oxide electrode for high-rate discharge and charge*, Journal of Power Sources* 126 (2004) 139-143.

[7] C.A. Grimes, Synthesis and application of highly ordered arrays of TiO_2 nanotubes, *Journal o f Materials Chemistry* 17 (2007) 1451–1457.

[8] Maryam Salari, Seyed Hamed Aboutalebi, Konstantin Konstantinov and Hua Kun Liu, A highly ordered titania nanotube array as a supercapacitor electrode, *Physical Chemistry Chemical Physics* 13 (2011) 5038-5041.

[9] Song-Zhu Chu, Satoru Inoue, Kenji Wada, Di Li, Hajime Haneda, and Satoshi Awatsu, Highly Porous (TiO_2−SiO_2−TeO_2)/Al_2O_3/TiO_2 Composite Nanostructures on Glass with Enhanced Photocatalysis Fabricated by Anodization and Sol−Gel Process, *Journal of Physical Chemistry B* 107 (2003) 6586–6589.

[10] Dae-Jin Yang, Ho-Gi Kim, Seong-Je Cho, and Won-Youl Choi, Vertically Oriented Titania Nanotubes Prepared by Anodic Oxidation on Si Substrates, *IEEE Transactions on Nanotechnology* 7 (2008) 131-134.

[11] Gopal K. Mor, Oomman K. Varghese, Maggie Paulose, Karthik Shankar, Craig A. Grimes, A review on highly ordered, vertically oriented TiO_2 nanotube arrays: Fabrication, material properties, and solar energy applications, *Solar Energy Materials and Solar Cells* 90 (2006) 2011-2075.

[12] J.M. Macak, H. Tsuchiya, S. Berger, S. Bauer, S. Fujimoto, P. Schmuki, On wafer TiO_2 nanotube-layer formation by anodization on Ti-films on Si, *Chemical Physics Letters* 428 (2006) 421-425.

[13] Jan M. Macak, Patrik Schmuki, Anodic growth of self-organized anodic TiO_2 nanotubes in viscous electrolytes, *Electrochimica Acta* 52 (2006) 1258-1264.

[14] N.K. Allam, C.A. Grimes, Effect of cathode material on the morphology and photoelectrochemical properties of vertically oriented TiO2 nanotube arrays, Solar Energy Materials and Solar Cells 92 (2008) 1468-1475.

[15] S. Lemeshko, S. Gavrilov, V. Shevyakov, V. Roschin, R. Solomatenko, Investigation of Tip-Induced Ultrathin Ti Film Oxidation Kinetics, *Nanotechnology* 12 (2001) 273-276

[16] V.M. Prida, E. Manova, V. Vega, M. Hernandez-Velez, P. Aranda, K.R. Pirota, M. Vazquez, E. Ruiz-Hitzky, Temperature influence on the anodic growth of self-aligned Titanium dioxide nanotube arrays, *Journal of Magnetism and Magnetic Materials* 316 (2007) 110–113.

[17] Satoshi Kaneco, Yongsheng Chen, Paul Westerhoff and John C. Crittenden, "Fabrication of uniform size titanium oxide nanotubes: Impact of current density and solution conditions," *Scripta Materialia* 56 (2007) 373-376.

[18] Jianling Zhao, Xiaohui Wang, Tieyu Sun, Longtu Li, Crystal phase transition and properties of titanium oxide nanotube arrays prepared by anodization, *Journal of Alloys and Compounds* 434-435 (2007) 792-795.

[19] Yibing Xie, Li Min Zhou, Haitao Huang, Enhanced photoelectrochemical current response of titania nanotube array, *Materials Letters* 60 (2006) 3558-3560.

[20] G. K. Mor, K. Shankar, M. Paulose, O. K. Varghese, and C. A. Grimes, Enhanced Photocleavage of Water Using Titania Nanotube Arrays, *Nano Letters* 5 (2005) 191-195.

[21] Keat G. Ong, Oomman K. Varghese, Gopal K. Mor, Karthik Shankar, Craig A. Grimes, Application of finite-difference time domain to dye-sensitized solar cells: The effect of nanotube-array negative electrode dimensions on light absorption, *Solar Energy Materials & Solar Cells* 91 (2007) 250-257.

[22] Jong Ho Lee, Misook Kang, Suk-Jin Choung, Kenji Ogino, Seizo Miyata, Moon-Sun Kim, Jong-Yul Park, Jin Bae Kim, The preparation of TiO_2 nanometer photocatalyst film by a hydrothermal method and its sterilization performance for Giarda lamblia, *Water Research* 38 (2004) 713-719.

[23] Laurence J. Hardwick, Michael Holzapfel, Petr Novak, Loic Dupont, Emmanuel Baudrin, Electrochemical lithium insertion into anatase-type TiO2: An in situ Raman microscopy investigation, *Electrochimica Acta* 52 (2007) 5357-5367.

[24] Junrong Li, Zilong Tang, Zhongtai Zhang, Preparation and Novel Lithium Intercalation Properties of Titanium Oxide Nanotubes, *Electrochemical and Solid-State Letters* 8 (2005) A316-A319.

[25] Zhaoyue Liu, Xintong Zhang, Shunsuke Nishimoto, Taketoshi Murakami and Akira Fujishima, Efficient Photocatalytic Degradation of Gaseous Acetaldehyde by Highly Ordered TiO2 Nanotube Arrays, *Environmental Science and Technology* 42 (2008) 8547–8551.

[26] Q.H. Zhang, W.D. Han, Y.J. Hong, J.G. Yu, Photocatalytic reduction of CO_2 with H_2O on Pt-loaded TiO2 catalyst, *Catalysis Today* 148 (2009) 335–340.

[27] O. Varghese, M. Paulose, T. LaTempa, and C.A. Grimes, High-Rate Solar Photocatalytic Conversion of CO_2 and Water Vapor to Hydrocarbon Fuels, *Nano Letters* 9 (2009) 731-737.

Chapter 3

Experiment Setup

In this chapter, titania nanotube synthesis via anodic oxidation method is described as well as the procedure for doping the titania nanotubes with ruthenium. Next, the equipment set-up for performing the Sabatier reaction is described. The use of the Diffuse Reflectance Infrared Fourier Transform spectrometry for studying the simultaneous water splitting and carbon monoxide methanation mechanism is outlined. The apparatus for photocatalytic water splitting experiments, namely the two-dimensional quartz plate reactor, is described.

3.1 Nanotube Synthesis

Titania nanotubes were formed via anodic oxidation from titanium foils (Sigma-Aldrich, 99.9% Ti) and from thin titanium films deposited on silicon wafers and glass by E-Beam evaporation. To form the thin titanium film substrates, 200 nm of SiO_2 were evaporated onto 2-inch diameter (100) silicon wafers in the chamber of an SJ-26 E-Beam evaporator at 2.0 X 10^{-6} torr in a clean room environment. The deposition took place at a rate of 10 Angstroms per second measured by crystal sensor. Next, 600 nm of titanium was evaporated onto the surface of the SiO_2 inside the chamber of an SJ-20 E-Beam

evaporator. The deposition took place at a pressure of approximately 1.0 X 10^{-6} torr and at a rate of 12 Angstroms per second measured by crystal sensor.

After film deposition, the wafers were diced into squares for use as anodes immersed in 50 mL of fluoride-containing electrolyte for anodic oxidation. During anodization, a 4 cm^2 platinum foil (Sigma-Adrich, 99.9% Pt) was used as a cathode. The anode and cathode had a separation distance of 3 cm during experiments. Figure 3.1 is a diagram showing the anodic oxidation setup. Figure 3.2 is a macroscopic image of a titania nanotube array synthesized using an aqueous sodium fluoride and glycerol electrolyte.

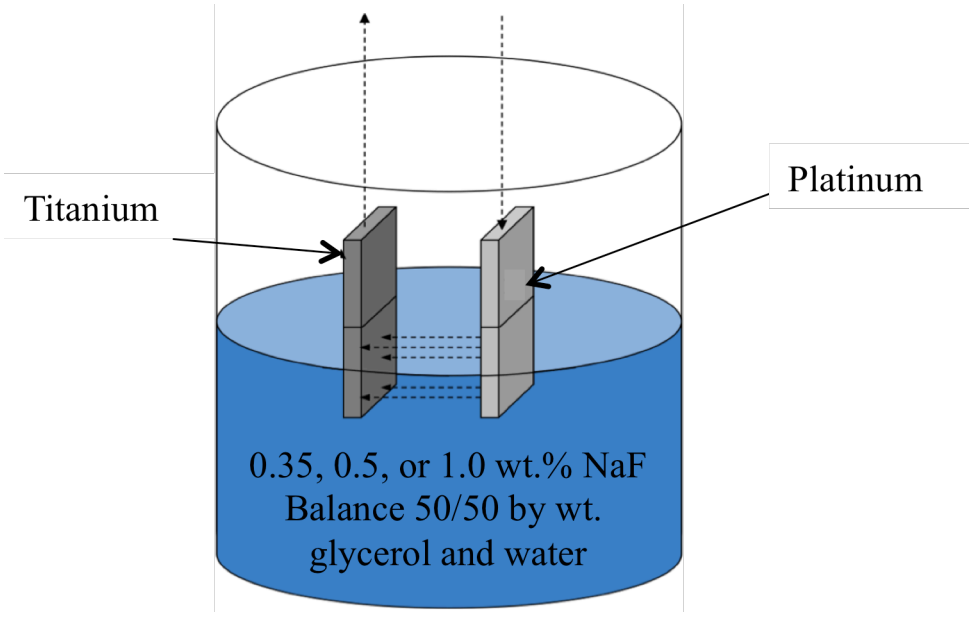

Figure 3.1: Diagram of the anodic oxidation reaction set-up for titania nanotubes. A platinum cathode and titanium substrate are immersed in electrolyte and an electrical potential is applied.

Figure 3.2: Macroscopic image of a titania nanotube array created from titanium foil. The top portion is the un-anodized titanium and the multicolored area is composed of titania nanotubes.

The electrolytes tested contained 0.35, 0.5, and 1.0 wt. % sodium fluoride, respectively, and the balance being equal amounts of deionized water and glycerol (Sigma-Aldrich, reagent grade 99.9% glycerol) by weight. Table 3.1 shows the pH values for each of the electrolytes tested. Figure 3.3 is a side-view illustration of the $Si/SiO_2/Ti$/Titania nanotube system.

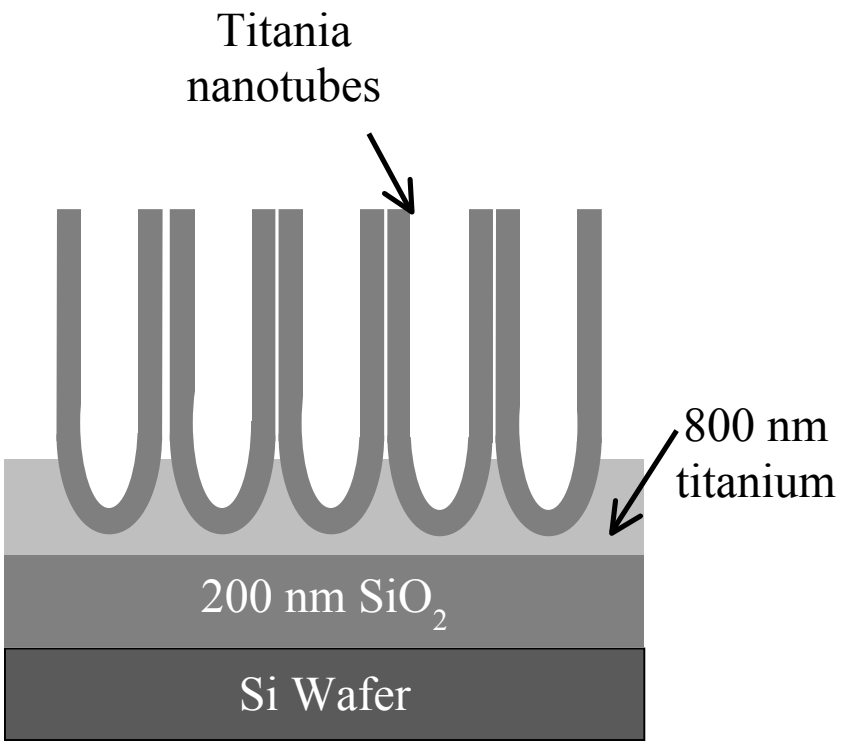

Figure 3.3: Side view illustration of the $Si/SiO_2/Ti$/Titania nanotube system.

Table 3.1: Synthesis electrolyte pH as a function of fluoride concentration.

F^- Concentration (wt.%)	Electrolyte pH
0.35	7.64
0.5	7.77
1.0	8.09

Anodizations were performed at room temperature and constant voltage using a DC power supply (Agilent, E3632A, 0-15V, 7A/0-30V, 4A). The current was monitored using a Data Acquisition/Switch Unit system (Agilent, 34970A) and Agilent BenchLink Data Logger software. After anodization, the samples were removed from the electrolyte, cleaned with deionized water, and dried. Please refer to Appendix A for a complete description of the titania nanotube synthesis steps.

3.2 Doping with Ruthenium

Titania nanotubes were doped with ruthenium by wetness impregnation via 0.025 M ruthenium (III) chloride hexahydrate (Sigma-Aldrich, 38.0-42.0% Ru basis). Ruthenium chloride was reduced to metallic ruthenium, as verified by X-Ray Photoelectron Spectroscopy (XPS), by annealing at 250°C for three hours. The same procedure was followed for impregnating Degussa P25 titanium dioxide with ruthenium.

3.3 Sabatier Reactor

Carbon dioxide methanation in the absence of UV light took place in a jacketed stainless steel tubular reactor with a volume of approximately 50 cm^3. A temperature controller regulated the temperature of the jacket. Mass flow controllers were used to deliver reaction gases to the tubular reactor. Quartz wool was placed at the entrance and exit of the catalyst bed to promote mixing. A Varian CP-3800 Gas Chromatograph (GC) equipped with two thermal conductivity detectors and a flame ionization detector measured products. Figure 3.4 is a schematic of the reactor setup. Please refer to Appendix G for a description of the gas chromatography method.

The reactions took place at 200-600°C. The catalysts were added to the tubular reactor with quartz wool to increase mixing of gases. Pre-purified nitrogen flowed through the reactor until the reactor jacket reached the temperature set-point. Once the set-point was reached, the reaction gases were added. The reactor feed consisted of

28.6% carbon dioxide by volume (20 sccm), 57.1% hydrogen by volume (40 sccm), and the balance nitrogen (10 sccm) as an internal gas standard. The approximate space time velocity was 1.5 min^{-1}.

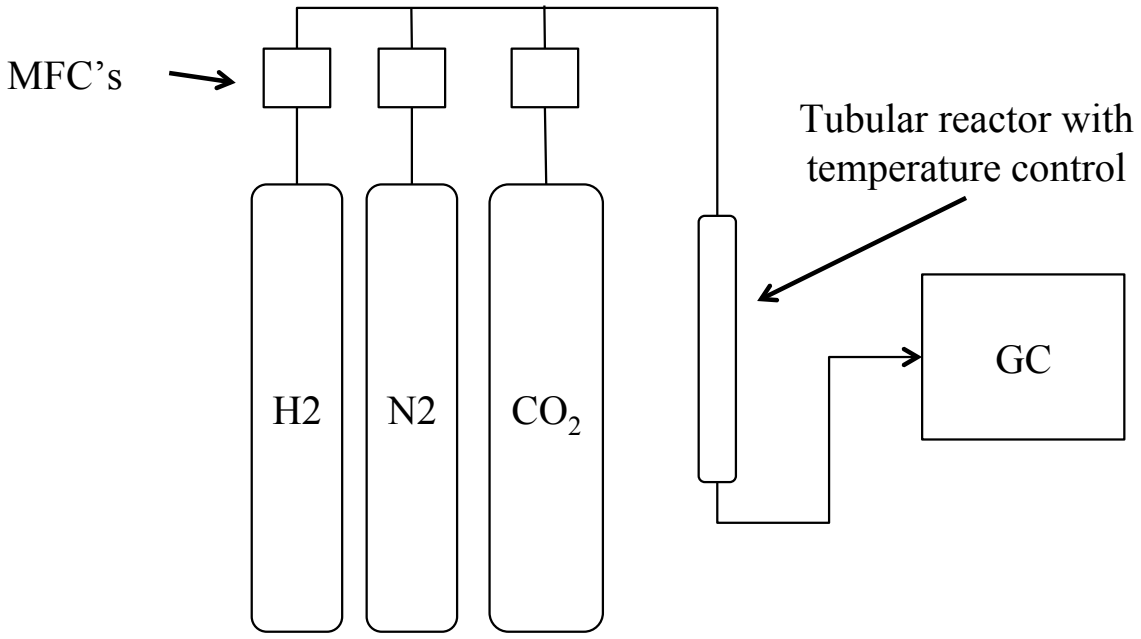

Figure 3.4: Diagram of the Sabatier reaction set-up. Hydrogen, nitrogen, and carbon dioxide flow to a jacketed stainless steel flow reactor and products are measured by GC.

3.4 Diffuse Reflectance Infrared Spectrometry of Simultaneous Water Splitting and Carbon Dioxide Methanation

To study simultaneous water splitting and carbon dioxide methanation *in-situ*, reaction intermediates and products were measured using the Diffuse Reflectance Infrared Fourier Transform Spectrometry (DRIFTS) mode of a Bruker FT-IR. A reaction chamber equipped with two ZnSe windows for infrared (IR) measurements and one quartz window for UV light to illuminate the catalyst surface. Therefore, the reactor chamber allowed for the detection and comparison of molecules that adsorb to the

catalyst surface when illuminated by UV light and in the absence of UV light. The reaction chamber was equipped with a heater to measure reaction intermediates at various catalyst temperatures. Figure 3.5 is a photograph of the introduction of UV light into the ZnSe reaction chamber for a DRIFTS study.

Figure 3.5: Photograph of the introduction of UV light by a 100 W Hg lamp into a DRIFTS ZnSe reaction chamber port.

Diffuse Reflectance Infrared Fourier Transform Spectrometry employs diffuse reflectance of light in the infrared region to measure intermediate species of a chemical reaction. Incident infrared light is partially reflected by the surface of the catalyst material. Molecules that adsorb to a surface absorb particular frequencies of light that match the particular vibrational mode. This resonant frequency (the reflected infrared light) can be measured by a detector to determine the bond type of reactive intermediates.

3.5 Two-Dimensional Quartz Plate Reactor

Photocatalytic water splitting occurred in a two-dimensional heated stainless steel flow reactor equipped with a 0.25-inch thick quartz plate to allow for the introduction of UV light. The reactor bed measured approximately 2 cm X 2 cm X 6.5 cm. The quartz plate allowed for catalyst illumination of approximately 7 cm^2. A heater attached to the bottom of the reactor allowed for temperature control by temperature controller. Figure 3.6 is a photograph of the two-dimensional quartz plate reactor. Appendix D provides detailed schematics for the quartz plate reactor.

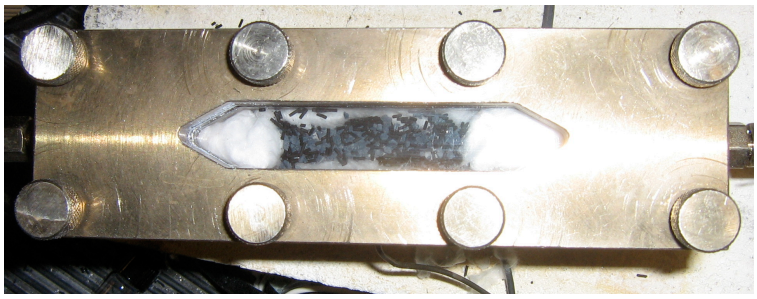

Figure 3.6: Photograph of the top view of the two-dimensional quartz plate flow reactor.

Mass flow controllers regulated the feed gases except for water vapor. Quartz wool was placed near the internal inlet and outlet of the quartz plate reactor to promote mixing. Pre-purified nitrogen flowed through the reactor until the reactor reached the temperature set-point. Approximately thirty minutes after the set-point was reached, the reaction gases were added. A stream of 20% carbon dioxide by volume (10 sccm) and the balance nitrogen (40 sccm) flowed through a saturator at 25°C so that the feed stream into the plate reactor contained 20 torr water vapor, 150 torr carbon dioxide, and the 590

torr nitrogen. The approximate space time velocity was 2 min^{-1}. After twenty minutes, the UV light was incorporated perpendicular to the catalyst surface. The reactions took place at 25-150°C.

Products traveled to a condenser before measurement by a Varian CP-3800 Gas Chromatograph equipped with two thermal conductivity detectors and a flame ionization detector. Please refer to Appendix E for detailed operating procedures for the quartz plate reactor. Also, please refer to Appendix F for calibration curves for the Varian CP-3800 Gas Chromatograph and Appendix G for the GC method. Figure 3.7 is a diagram of the experiment set-up.

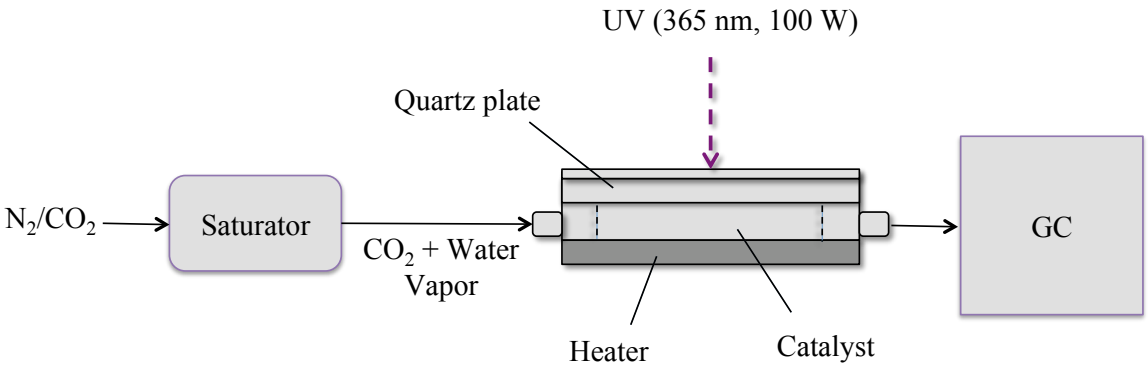

Figure 3.7: Experiment set-up for the water splitting reaction in a quartz plate reactor. CO2, N2, and water vapor are fed to the reactor where they react over photocatalyst illuminated by UV light and products are measured by GC.

References

[1] Michael P. Fuller, Peter R. Griffiths, Diffuse reflectance measurements by infrared Fourier transform spectrometry, *Analytical Chemistry* 50 (1978) 50 1906-1910.

Chapter 4

Characterization of Titania Nanotubes

The geometries and properties of titania nanotubes can be tailored by altering the synthesis conditions. Extensive work has been done to evaluate the effects of electrolyte composition, synthesis temperature, and applied electrical potential. For example, Mor and coworkers studied the effect of electrolyte composition and applied electrical potential on titania nanotube dimensions [1]. Macak and Schmuki studied the formation of titania nanotubes in viscous electrolytes, which was found to create smoother titania nanotubes [2].

The dimensions of titania nanotubes can also determine the catalytic properties of titania nanotubes. Mor and coworkers found that increasing the nanotube wall thickness also increases the effectiveness of titania nanotubes for the photocatalytic water splitting application. Lower synthesis electrolyte temperatures resulted in the thicker titania nanotube walls [3]. The possibility for "metallic-like" titania nanotubes was modeled by Enyashin and Ivanovskii, who predicted the possibility of TiO nanostructures [4].

In addition, previous work has examined the titania surfaces to determine the factors that affect photocatalytic activity. Nakamura and coworkers suggested that the electrical properties and hydrophilicity of amorphous titania films are determined by surface hydroxyl groups [5]. These two factors can determine the ability of the titania surface to adsorb hydroxyls during a water splitting reaction.

In this chapter, the correlation between the synthesis electrolyte composition, the photocatalytic properties, and the oxygen content of amorphous titania nanotubes will be discussed.

4.1 Titania Nanotube Formation

0.35 wt.%, 0.5 wt.%, and 1.0 wt.% sodium fluoride-containing electrolytes were effective in forming titania nanotubes using applied electrical potentials between 8 Volts and 12 Volts. For scanning electron microscopy (SEM) studies, samples were mounted to a metal stage and viewed under a Philips XL30 Field Emission Gun Scanning Electron Microscope. Compositional analysis by Energy Dispersive Spectroscopy (EDS) was performed using the SEM. Titania nanotube samples synthesized in 0.5 wt.% sodium fluoride-containing electrolyte with an applied electrical potential of 10 V were viewed under an FEI Magellan™ XHR SEM at FEI's Nanoport in Eindhoven, The Netherlands. The images were recorded with an in-lens secondary electron detector at an accelerating voltage of 2.02 kilovolts and a working distance of 2mm. Figure 4.1 is a top-view SEM image of a titania nanotube array [6].

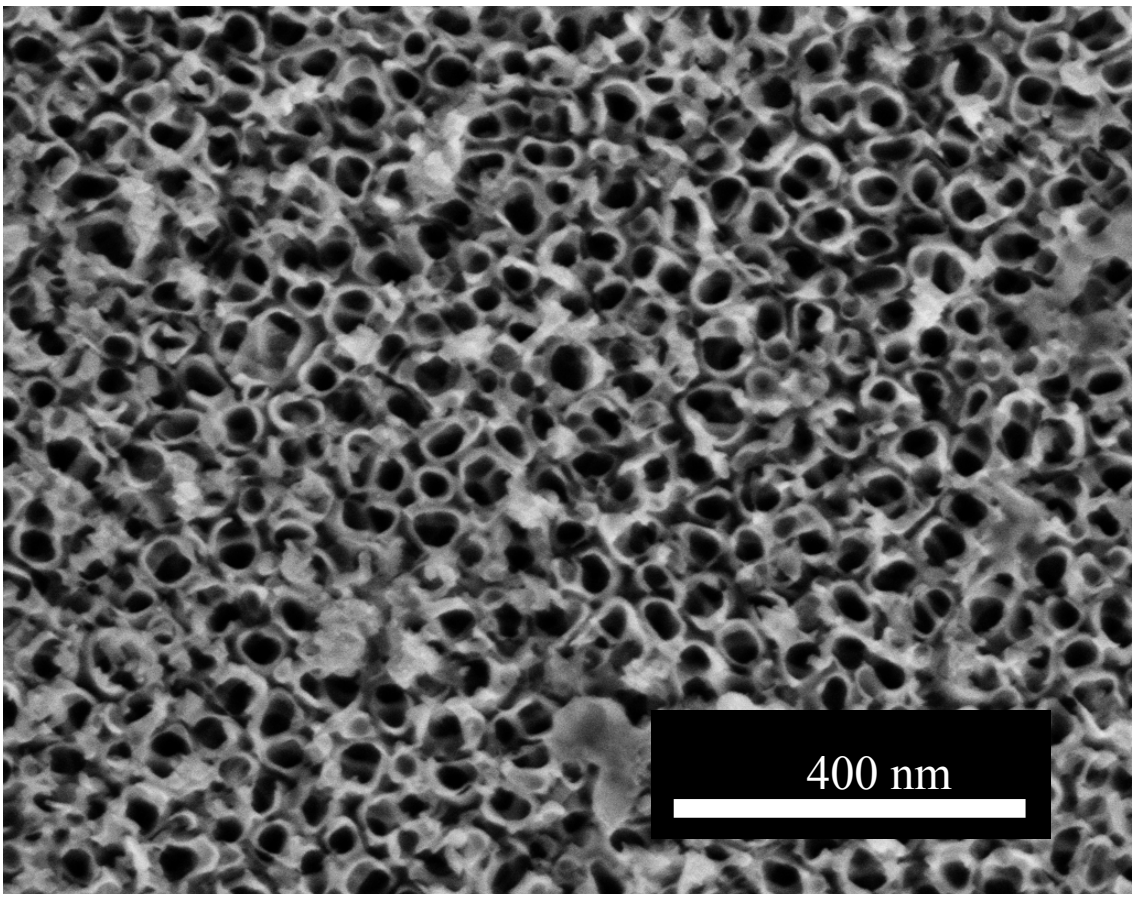

Figure 4.1: Top view image of a titania nanotube array take by Magellan high resolution scanning electron microscope at FEI's Nanoport in Eindhoven, The Netherlands [6].

The oxygen to titanium ratio appears to be a function of synthesis electrolyte fluoride concentration. EDS data measuring the oxygen to titanium ratio is shown in Figure 4.2. Samples that were synthesized in higher fluoride-containing electrolytes resulted in lower oxygen to titanium ratios than samples synthesized in lower fluoride-containing electrolytes. A possible source of error in the oxygen to titanium ratio measurements is the variation in nanotube length caused by the differences in electrolyte fluoride concentrations. Shorter titania nanotubes synthesized in lower-fluoride containing electrolytes may have also included a large amount of un-anodized titanium sub-layer in the EDS measurements. Longer titania nanotubes synthesized in higher

fluoride-containing electrolytes would have included less of the titanium sub-layer in the EDS measurements. As a result, the increase in oxygen to titanium ratio may be an underestimate of the actual oxygen to titanium ratio for the titania nanotubes synthesized in 0.35 wt.% sodium fluoride-containing electrolytes.

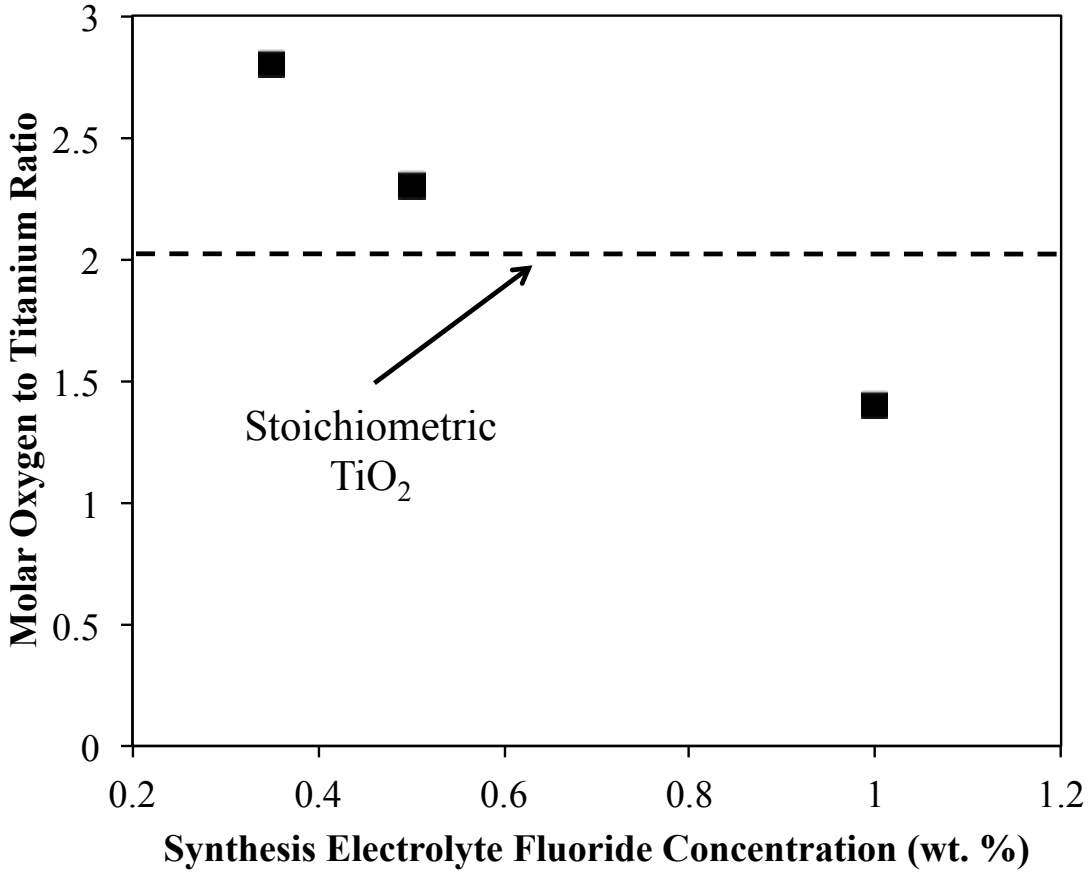

Figure 4.2: Molar ratio of oxygen to titanium as a function of fluoride concentration in the synthesis electrolyte as measured by EDS.

The increased oxygen to titanium ratio in titania nanotubes synthesized in lower fluoride-containing electrolytes may be due increased adsorbed hydroxyl groups. This hypothesis will be discussed more in the next sections of this chapter. Due to the variability in the EDS technique for measuring the oxygen to titanium ratio, the trend as a function of synthesis electrolyte fluoride concentration is of interest. EDS is not as exact

as other methods, such as Electron Energy Loss Spectroscopy, and the titania nanotubes create an irregular surface. However, concentrations of fluoride up to 4.0 wt.% in the titania nanotubes have been measured by EDS, which supports the possibility of sub-stoichiometric titania nanotubes. Fluoride, sodium, and carbon have also been detected in the titania nanotubes by X-ray photoelectron spectroscopy (XPS).

Recent terahertz spectroscopy studies have also suggested the existence of sub-stoichiometric titania nanotubes. The terahertz spectroscopy experiments were based on simulations and photoconductivity measurements. Richter and Schmuttenmaer observed Ti^{3+} states in titania nanotubes synthesized from Ti foil via anodic oxidation. The Ti^{3+} states can result from oxygen vacancies, titanium interstitials, or substitutional fluoride impurities resulting from the anodic oxidation synthesis technique [7]. Fluoride impurities were measured during the EDS experiments described above, which suggests that higher fluoride concentrations may result in fluoride ions taking the place of oxygen during synthesis causing the observed low O:Ti ratio.

Nanotubes synthesized from a thin titanium film on a silicon wafer in 0.5 wt.% sodium fluoride-containing electrolyte with an applied electrical potential of 10 Volts were viewed by high resolution transmission electron microscopy (TEM). The titania nanotubes were mechanically scraped from the silicon wafer onto a copper mesh TEM grid with carbon support. The side view images of the titania nanotubes were imaged by 200 kV electrons with a JEOL 2010F Field Emission Gun Analytical Electron Microscope (AEM) in the TEM and Scanning Transmission Electron Microscopy (STEM) modes.

Figure 4.3 shows the TEM and STEM images of the titania nanotubes formed at 10 Volts in the 0.5 wt.% sodium fluoride electrolyte. A side-view TEM image shows titania nanotubes oriented perpendicular to the titanium substrate (Figure 4.3A). The closed bottom of a titania nanotube is attached to the titanium sublayer as shown by High Resolution TEM (HR-TEM) (Figure 4.3B). Side-view bright field and dark field STEM images are shown in Figure 4.3C and Figure 4.3D. E-beam diffraction patterns show the amorphous nature of titania nanotubes that were not annealed in Figure 4.4. Figure 4.5 shows the polycrystalline structure of the titanium film deposited by E-beam evaporation.

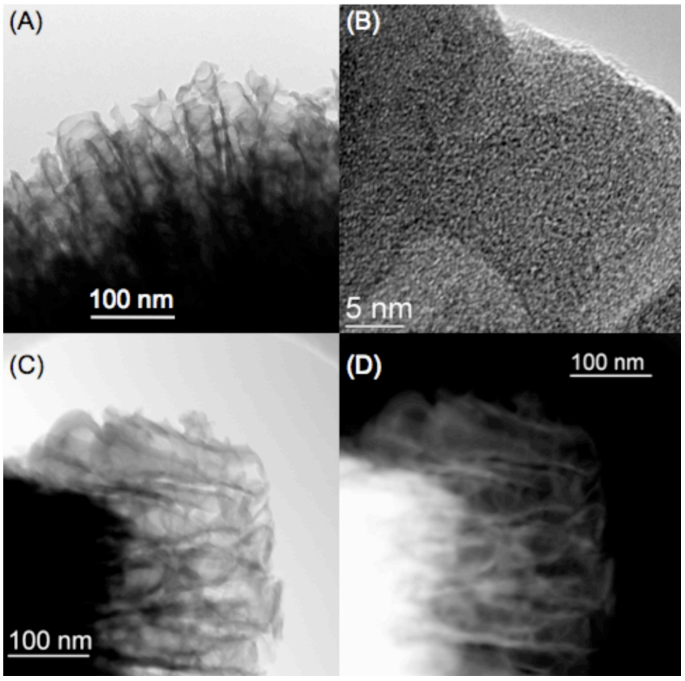

Figure 4.3: Titania nanotubes formed at 10 Volts in the 0.5 wt.% sodium fluoride electrolyte. (A) Side view TEM image, (B) individual nanotube wall HR-TEM image, (C) side view STEM bright field image, and (D) side view STEM dark field image [6].

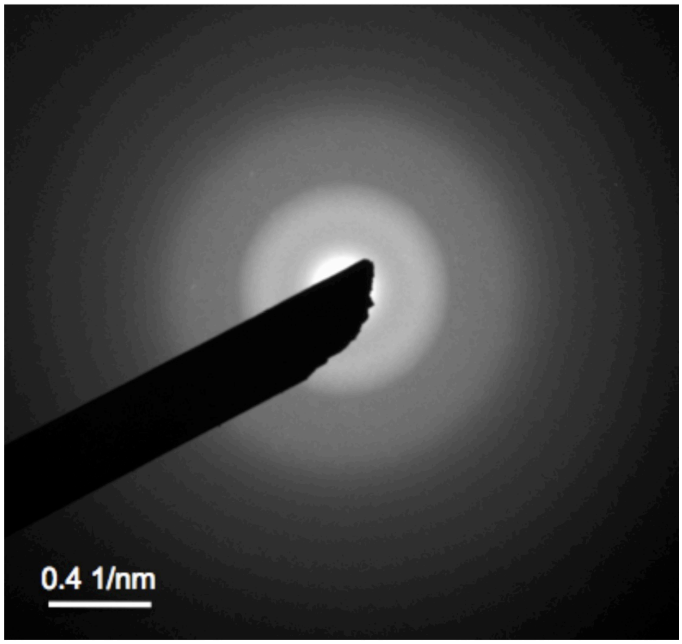

Figure 4.4: E-beam diffraction of a titania nanotube wall reveals that the nanotubes are amorphous after synthesis [6].

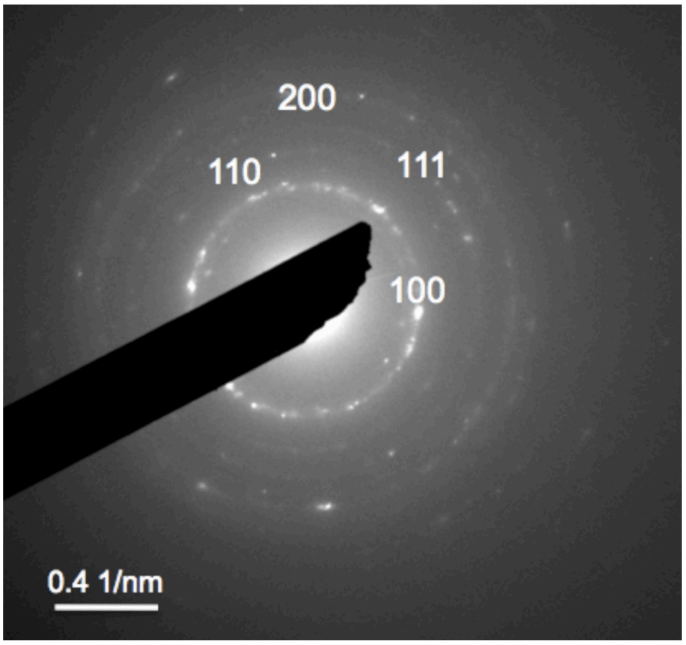

Figure 4.5: E-beam diffraction of the titanium sub-layer reveals that the starting material is polycrystalline titanium [6].

4.2 Trends in Nanotube Dimensions

Figure 4.6 and Figure 4.7 show the correlation between applied electrical potential and titania nanotube outer diameter and wall thickness. The applied electrical potential impacts the outer diameter and wall thickness because it affects the kinetics of the oxide formation and etching process during nanotube formation [8-9]. Figure 4.6 shows that the titania nanotube outer diameter decreases to a minimum and then increases with increasing applied electrical potential and constant electrolyte fluoride content of 0.5 wt.%. A steep increase in outer diameter between 10 and 12 V is observed most likely because the greater applied electrical potential created larger pores from which the nanotubes formed. Applied electrical potentials above 12 Volts failed to form nanotubes, which suggests that the fluoride etched away the surface of the titania and prevented the formation of new oxide. This indicated that 12 V is the top of the range of allowed applied electrical potentials for this system to form nanotubes.

Figure 4.7 shows that higher applied electrical potentials at a constant fluoride content of 0.5 wt.% during synthesis result in larger titania nanotube wall thicknesses. The trend in nanotube diameter and wall thickness presented here is consistent with previous work [10-11].

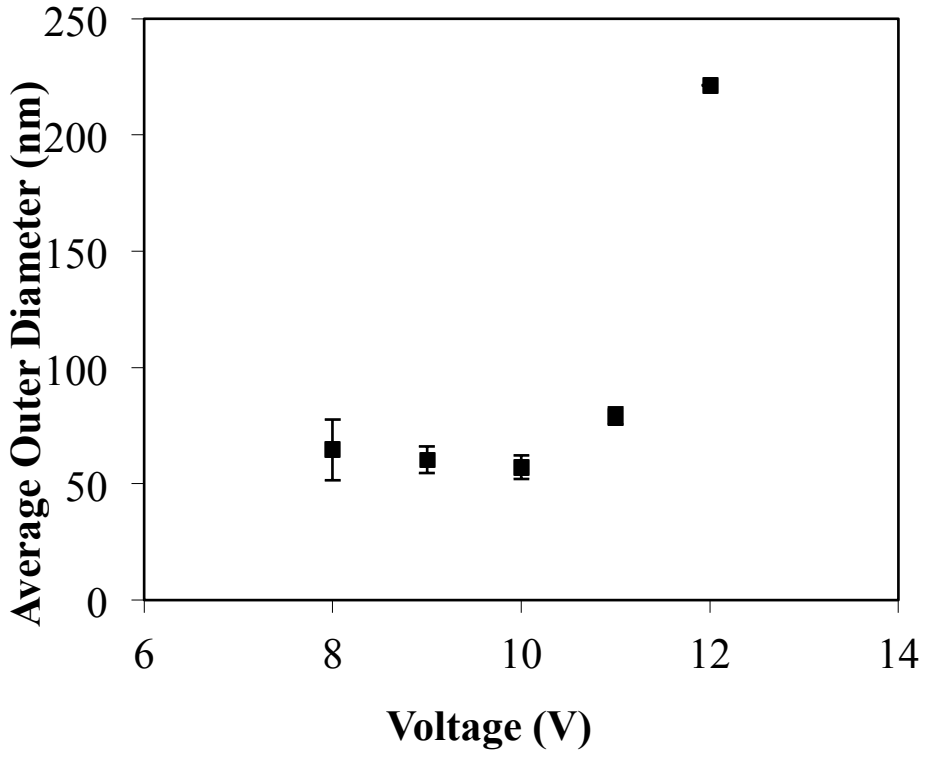

Figure 4.6: Titania nanotube outer diameter as a function of applied electrical potential and constant electrolyte fluoride content [6].

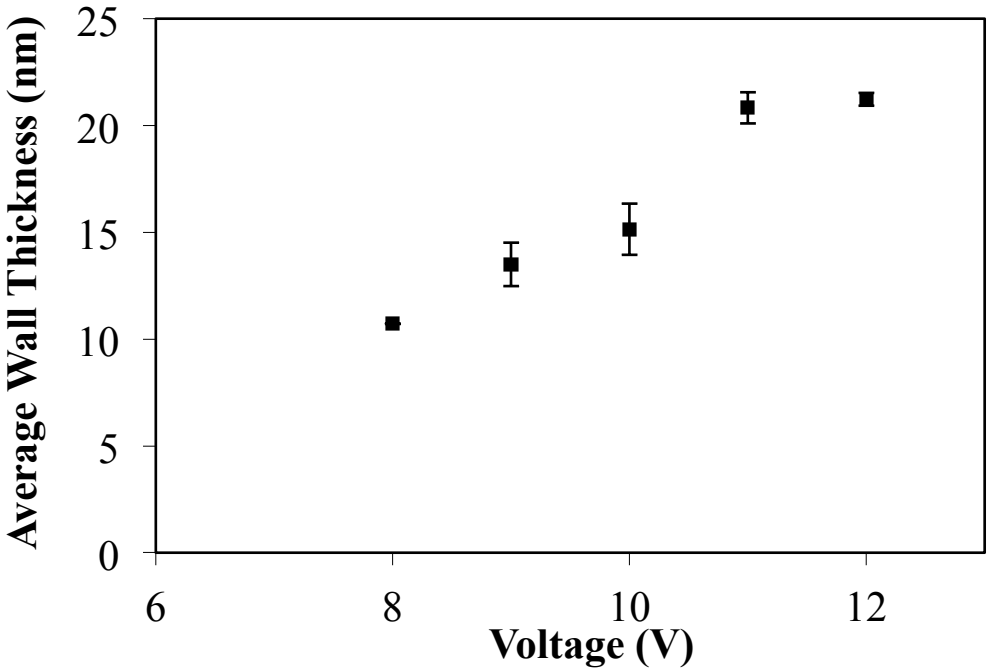

Figure 4.7: Average wall thickness as a function of applied electrical potential and constant applied electrical potential [6].

In Figure 4.8, the titania nanotube average outer diameter and wall thickness do not vary significantly with fluoride concentration in the synthesis electrolyte using a constant applied electrical potential of 10 Volts. The chemical dissolution rate is known to increase with increasing fluoride concentration, but also decreases with pH [10]. The electrolytes containing 0.35, 0.5, and 1.0 wt.% sodium fluoride have pH's of 7.07, 7.83, and 8.43, respectively. Therefore, the similarities of electrolyte pH's due to the addition of glycerol may explain the lack of variation in outer diameters and wall thicknesses.

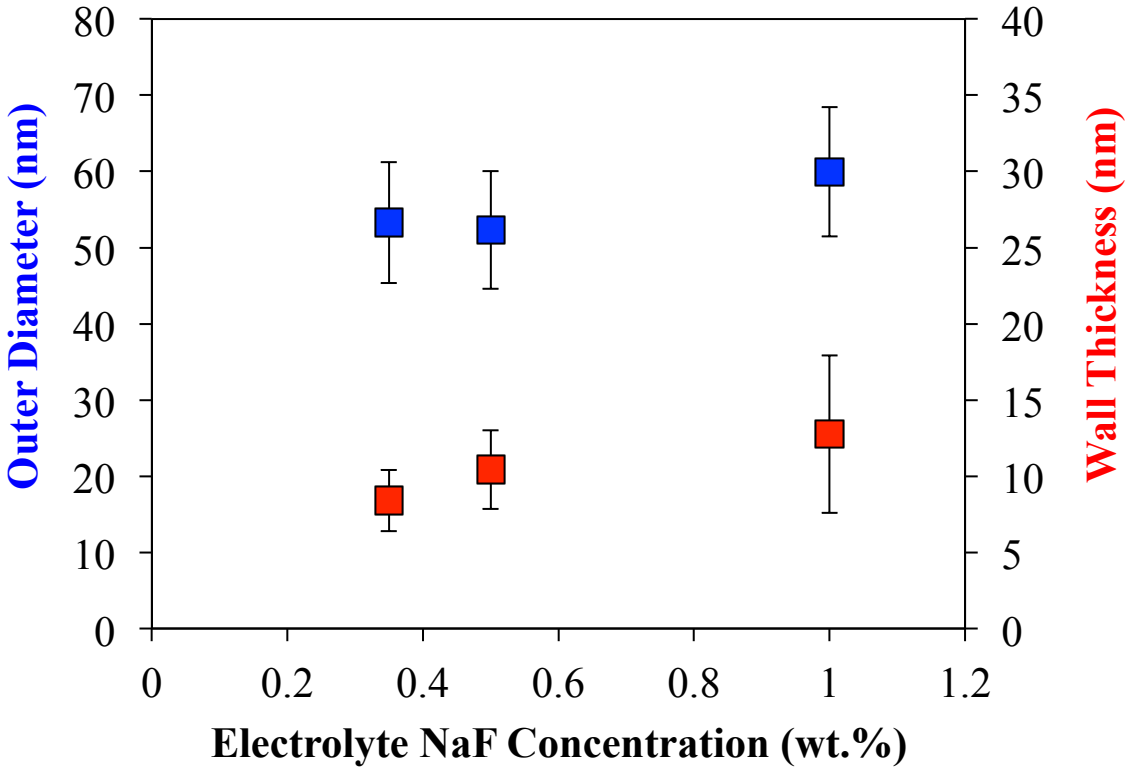

Figure 4.8: Outer diameter and wall thickness as a function of electrolyte fluoride concentration at a constant applied electrical potential.

4.3 Surface Area

The nanotube arrays degassed at 120°C and 5 μmHg were characterized by nitrogen adsorption–desorption experiments. An ASAP 2020 Surface Area and Porosity Analyzer measured the samples synthesized in 0.5 wt.% sodium fluoride electrolyte to have a BET surface area of approximately 178 m^2/g. This result indicates that the titania nanotube arrays offer a high surface area and may be a suitable metal catalyst support.

4.4 Thermal Stability and Crystal Structure

The stability of titania nanotubes in air and nitrogen at high temperatures was studied by thermogravimetric analysis using a TA Instruments thermogravimetric analyzer (TGA Q500). Samples were heated to 850^{o}C in the presence of flowing dry air by ramping the temperature at 10°C/min and holding the temperature constant for one hour. Samples were also heated to 850°C in the presence of flowing nitrogen using the same procedure. The titania nanotubes were examined by SEM to determine the durability of the nanotube structure in the chemical and thermal environments and characterized by Raman spectroscopy to determine the resulting crystal structure.

Figure 4.9 shows a titania nanotube sample heated in air at 850°C for one hour. Titania nanotubes heated in air or in pure nitrogen at 850^{o}C retained a nanotube-like structure, but did not appear to be the homogenous titania nanotubes seen in Figure 4.1. Delamination of the underlying titanium film occurred as seen in Figure 4.10. Raman spectroscopy in Figure 4.11 indicates the presence of the anatase structure with a peak at 237.1 cm^{-1} and the presence of the rutile structure with peaks at 445.5 and 609.9 cm^{-1}. Therefore, the titania nanotubes are approximately 99% rutile and 1% anatase after heating in air to 850°C. The ability of the titania nanotubes to retain the nanotube structure indicates their possible use as a metal catalyst support and suggests the possible for high surface area rutile catalyst structures.

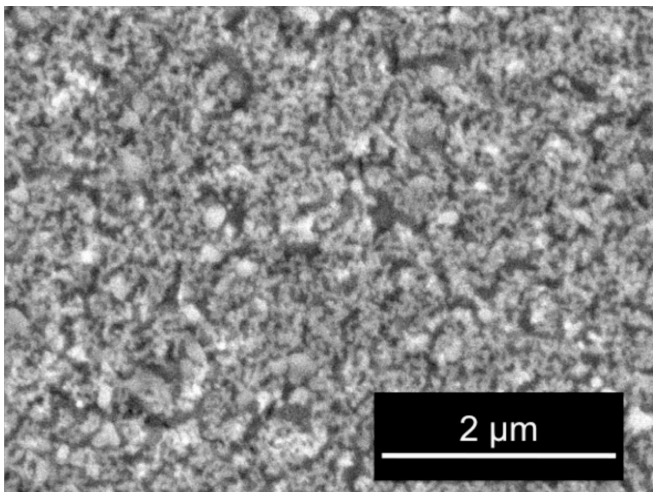

Figure 4.9: Top view SEM image of an intact titania nanotube array heated to 850°C in the presence of air [6].

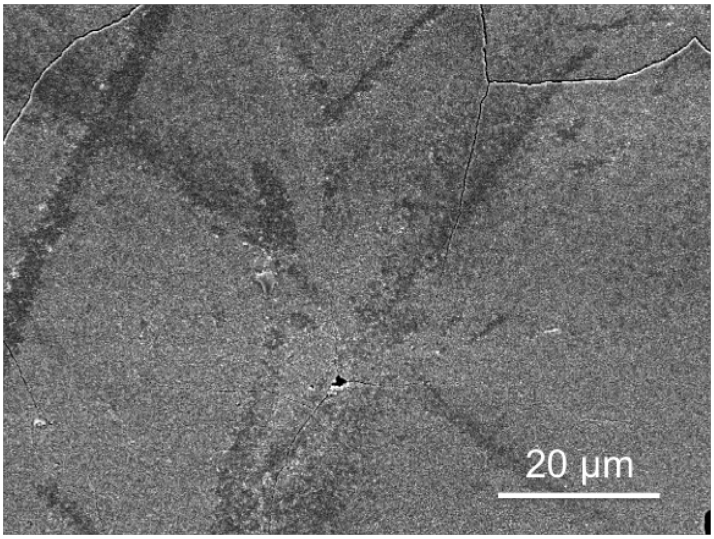

Figure 4.10: Delamination observed by scanning electron microscopy due to heating to 850°C in air.

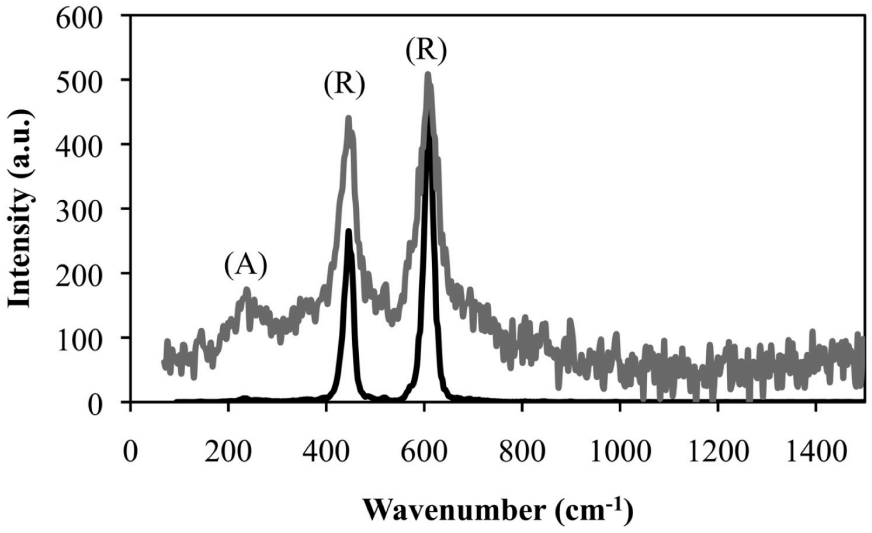

Figure 4.11: Raman spectroscopy showed that a titania nanotube array heated in air at 850°C resulted in a 99% rutile titania nanotube structure [6].

4.5 Conductivity of Titania Nanotubes

A four-terminal sensing configuration was used to study variations in the conductivity of amorphous titania nanotubes as a function of synthesis conditions. The benefit of using four-terminal sensing is that it does not measure the conductivity of the substrate below the titania nanotubes, which in this case is a silicon wafer. Amorphous titania nanotubes were synthesized using 0.35, 0.5, and 1.0 wt.% sodium fluoride-containing electrolyte using 600 nm Ti evaporated onto a Si wafer substrate as the starting material. Next, a physical mask was used to evaporate 150 nm of gold onto the surface of the titania nanotubes to act as electrodes in the four-point probe set-up. The gold was evaporated onto the titania nanotubes inside the chamber of an SJ-20 E-beam Evaporator at a pressure of approximately 1.0 X 10^{-6} torr and a deposition rate of 10 Angstroms per second measured by crystal sensor. Please refer to Appendix C for a

review of the four-point probe design for measuring the conductivity of the titania nanotube array.

Conductivity was measured along the surface of the titania nanotubes by attaching leads to the electrodes, applying an electrical potential using a DC power supply (Agilent, E3632A, 0-15V, 7A/0-30V, 4A), and measuring the resulting current through the titania nanotubes using a Data Acquisition/Switch Unit system (Agilent, 34970A) and Agilent BenchLink Data Logger software. The temperature of the titania nanotube samples was monitored by a surface temperature probe.

Figure 4.12 shows the measured current along the surface of titania nanotubes synthesized by 0.35, 0.5, and 1.0 wt.% sodium fluoride-containing electrolyte as a function of applied electric potential. Amorphous titania nanotubes synthesized in 0.35 wt.% sodium fluoride electrolyte showed reduced conductivity compared to titania nanotubes synthesized in 0.5 wt.% sodium fluoride electrolyte. Titania nanotubes synthesized in 1.0 wt.% sodium fluoride electrolyte were the most conductive. Since titania nanotubes act as excellent capacitors, hysteresis was observed when the applied electric potential was ramped up to 10 Volts and then back down to zero Volts.

The conductivity of the titania nanotubes was approximately an order of magnitude larger than the conductivity of titanium dioxide powder [12]. Possible causes for this may be fluoride impurities or the interaction of the electrical current with the titanium sub-layer underneath the nanotubes. In addition, the gold electrodes were in contact with the surface of the titania nanotubes, so the four-point sensing experiments were measuring an apparent surface conductivity. However, the gold electrodes may have diffused into the titania nanotube walls within a few nanometers of the surface.

Although the measurements were not performed under vacuum, the temperature of the samples only increased by 1-5°C as measured by temperature probe.

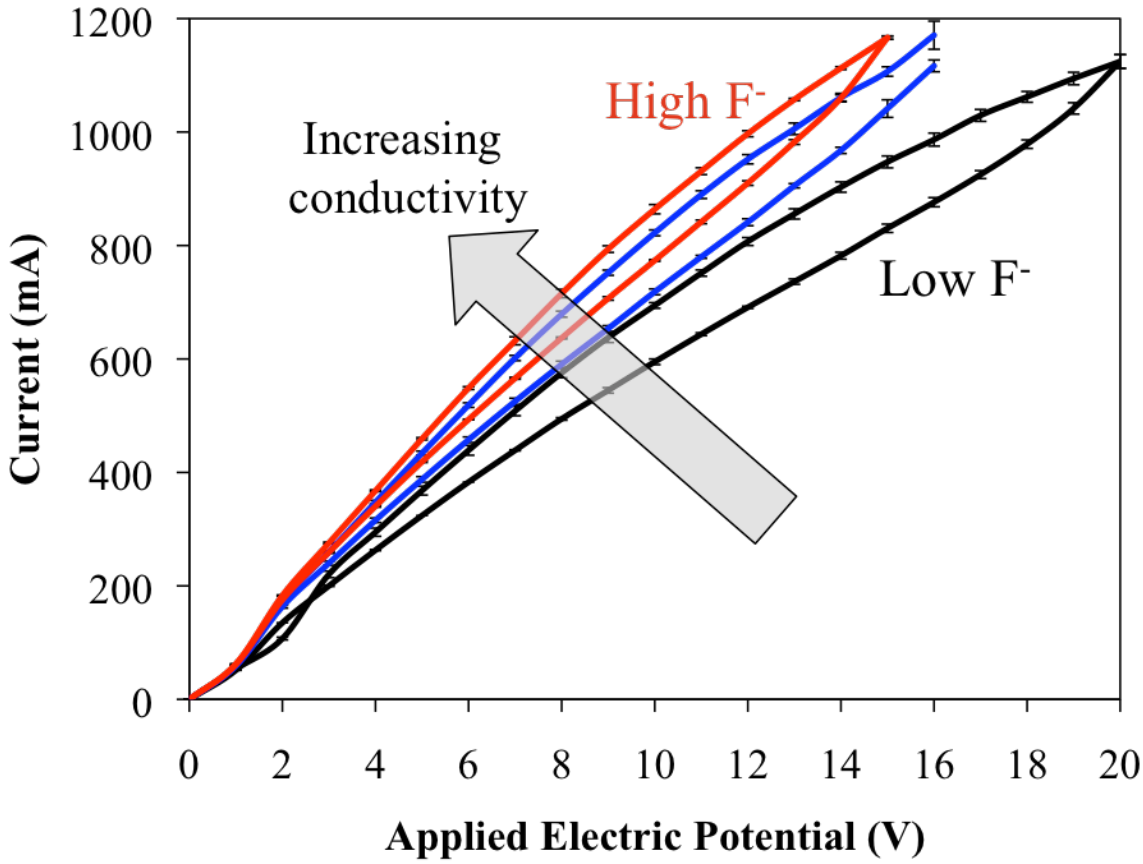

Figure 4.12: Graph of current versus applied electrical potential for titania nanotubes synthesized in electrolytes of varying fluoride contents measured by the four-point sensing system.

Despite the significantly lower resistivity of the titania nanotubes compared to bulk titanium dioxide, the four-point sensing experiments show a trend in the conductivity of the surface of titania nanotubes. The variation in conductivity between titania nanotube samples suggests that synthesis fluoride concentration influences the degree to which the nanotubes are conductive. The reduced conductivity of titania nanotubes synthesized in lower fluoride concentrations may be due to increased oxygen

content in the titania nanotubes or an increased number of adsorbed hydroxyl groups on the surface. Conversely, the increased conductivity of titania nanotubes synthesized in higher fluoride concentrations may be caused by fewer adsorbed hydroxyls and more fluoride impurities as measured by SEM and terahertz spectroscopy studies described in Section 4.1 of this chapter.

4.6 Titania Nanotube-Catalyzed Degradation of Methylene Blue

To study photocatalytic properties, the photocatalytic degradation of methylene blue was chosen as a test reaction. The photocatalytic degradation of methylene blue probe reaction is an indirect measurement of the photocatalytic water splitting reaction. Water molecules from the aqueous methylene blue solution adsorb onto the surface of the catalyst and are converted to hydroxyls, oxygen, and hydrogen, which then degrade the methylene blue molecule. The degradation of the methylene blue molecule can then be monitored as a function of time.

Titania nanotubes in thin titanium films deposited on silicon wafers were synthesized in 0.35 wt.%, 0.5 wt.%, and 1.0 wt.% sodium fluoride electrolytes. The amorphous titania nanotubes tested had a length of approximately 150 nm. Other photocatalysts tested were rutile titania nanotubes obtained from heating the amorphous titania nanotubes to 850°C in air for one hour and Degussa P25 titanium dioxide as a basis for comparison. The mass of photocatalyst remained constant for these experiments. The titania nanotubes consisted of approximately 0.12 mg of titania and

remained fixed to the silicon wafers. For the Degussa P25 experiments, 1.2 mg titanium dioxide powder was suspended in the methylene blue solution.

The samples tested were immersed in 20 mL of 72 μM methylene blue solution in a Pyrex glass batch reactor at room temperature and pre-purified air at 65 psi was bubbled into the solution. The pre-purified air agitated the methylene blue solution. The degradation of methylene blue occurred under 365 nm ultraviolet (UV) light from a 100W Hg lamp illuminating the surface of the photocatalysts tested. UV-VIS spectrometer was used to measure the molar absorbance of methylene blue as the degradation process occurred. The distance between the UV light source and the methylene blue solution remained constant for each experiment at a distance of about six inches.

The concentration of methylene blue was calculated for each of these samples based on calibration curves derived from the absorbance of methylene blue solutions of known concentrations. The standard solutions were measured at 664 nm. A linear correlation between the absorbance and the methylene blue concentration exists according to the Beer-Lambert Law. The Beer-Lambert Law is represented by the following equation:

$$A = \varepsilon \times L \times C \tag{4.1}$$

where A is the absorbance measured by photospectrometer, ε is the molar absorptivity, L is the path length, and C is the concentration of methylene blue. Since the molar

absorptivity and path length are constant in this system, a linear relationship between the measured absorbance and methylene blue concentration exists.

Houas and coworkers describe the decomposition of methylene blue in great detail using a titanium dioxide powder catalyst. The rate of decomposition is an apparent first order reaction that is dependent on the fraction of available sites occupied by adsorbed molecules. The decomposition products are ammonium, nitrate, and sulfate ions [13].

Figure 4.13 shows the degradation of 153 μM methylene blue under UV light for amorphous titania nanotubes, Degussa P25 titanium dioxide, and rutile titania nanotubes. Titania nanotubes synthesized in 0.35 wt.% sodium fluoride electrolyte degraded methylene blue at a higher rate than amorphous titania nanotubes formed using higher fluoride-containing electrolytes, Degussa P25, and rutile titania nanotubes. This indicates that amorphous titania nanotubes synthesized in lower fluoride-containing electrolytes have increased photocatalytic activity.

Titania nanotubes synthesized in the 0.5 wt.% and 1.0 wt.% sodium fluoride electrolyte did not exhibit the higher photocatalytic activity. The intermediate photocatalytic activity of titania nanotubes synthesized in electrolyte containing 1.0 wt.% sodium fluoride, instead of 0.5 wt.% sodium fluoride, is most likely due to a higher nanotube number density rather than oxygen to titanium ratio. Table 4.1 shows the titania nanotube number density measured by SEM images as a function of electrolyte concentration per square centimeter illuminated by UV light.

Table 4.1: Titania nanotube number density as a function of synthesis electrolyte fluoride concentration.

Synthesis Electrolyte Sodium Fluoride Wt.%	Nanotubes/cm^2
0.35	3.20E+10
0.5	3.52E+10
1.0	3.76E+10

Titania nanotubes synthesized in electrolytes containing greater amounts of sodium fluoride were estimated to have lower oxygen to titanium ratios compared to titania nanotubes synthesized in 0.35 wt.% sodium fluoride-containing electrolytes based on EDS measurements. The oxygen to titanium ratio in the titania nanotubes may explain the trends in conductivity of the titania nanotube surfaces since those with higher amounts of oxygen will be less conducting than titania nanotubes with lower oxygen content. As a result, the trends in conductivity further support the hypothesis that the more conducting titania nanotubes are not as photocatalytically active due to the lack of adsorbed hydroxyls or due to undesirable impurities in the nanotubes.

Titania nanotubes synthesized in electrolyte containing 0.35 wt.% sodium fluoride also photocatalytically degraded methylene blue at a higher rate than Degussa P25 titanium dioxide and rutile titania nanotubes. Degussa P25 is approximately 75% anatase and 25% rutile titanium dioxide, so this served at a baseline measurement and as a comparison of the amorphous titania nanotubes to the to the anatase structure. 1.2 mg of Degussa P25 was suspended in the methylene blue solution, which was approximately ten times the amount of titania in the titania nanotubes. The active surface area of the Degussa P25 is approximately 50 m^2/g. Therefore, the active surface area available for reactant adsorption on Degussa P25 was approximately 0.06 m^2. The active surface area

available for reactant adsorption on the titania nanotubes was approximately 0.021 m^2. Despite the larger active surface area, the Degussa P25 photocatalyst did not increase the degradation of methylene blue compared to titania nanotubes synthesized in low fluoride-containing electrolytes. Amorphous titania nanotubes also outperformed rutile titania nanotubes as a photocatalyst for methylene blue degradation, which suggests that the rutile nanotube structure is not optimal for photocatalytic applications.

In addition, the degradation of methylene blue by photolysis, meaning the oxygen is bubbled into the solution under UV light illumination without the presence of catalyst, outperforms the titania nanotubes synthesized in 0.5 and 1.0 wt.% sodium fluoride. This observation is probably due to the lack of photocatalytic activity of the titania nanotube sample as well as variability between experiments.

The deactivation of the photocatalytic degradation of methylene blue may also be due to changes in the polarity of the catalyst surface throughout the course of the reaction. In addition, the deactivation may be due to the irreversible adsorption of sulfate ions and other reaction products onto the titania surface [13].

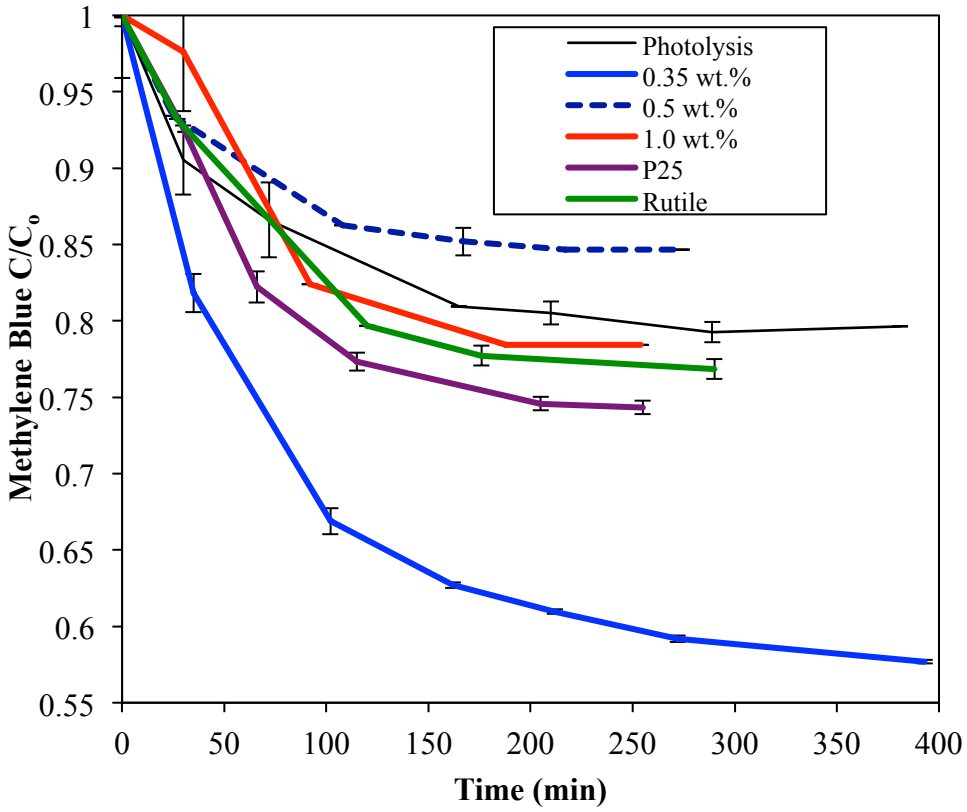

Figure 4.13: Methylene blue decomposition as a function of time for titania nanotubes synthesized in electrolyte containing 0.35, 0.5, and 1.0 wt.% sodium fluoride as well as Degussa P25 and rutile titania nanotubes [6].

The degradation of methylene blue fit first order kinetics for all of the samples tested. Table 4.2 shows the apparent rate constant and Figure 4.14 shows the first order behavior of the photocatalysts before deactivation occurs.

Table 4.2: First order reaction rate constants measured prior to deactivation for amorphous titania nanotubes as a function of synthesis electrolyte fluoride concentration.

NaF Concentration (wt.%)	Reaction Rate Constant (min^{-1})
0.35	0.00282
0.5	0.00092
1.0	0.00138

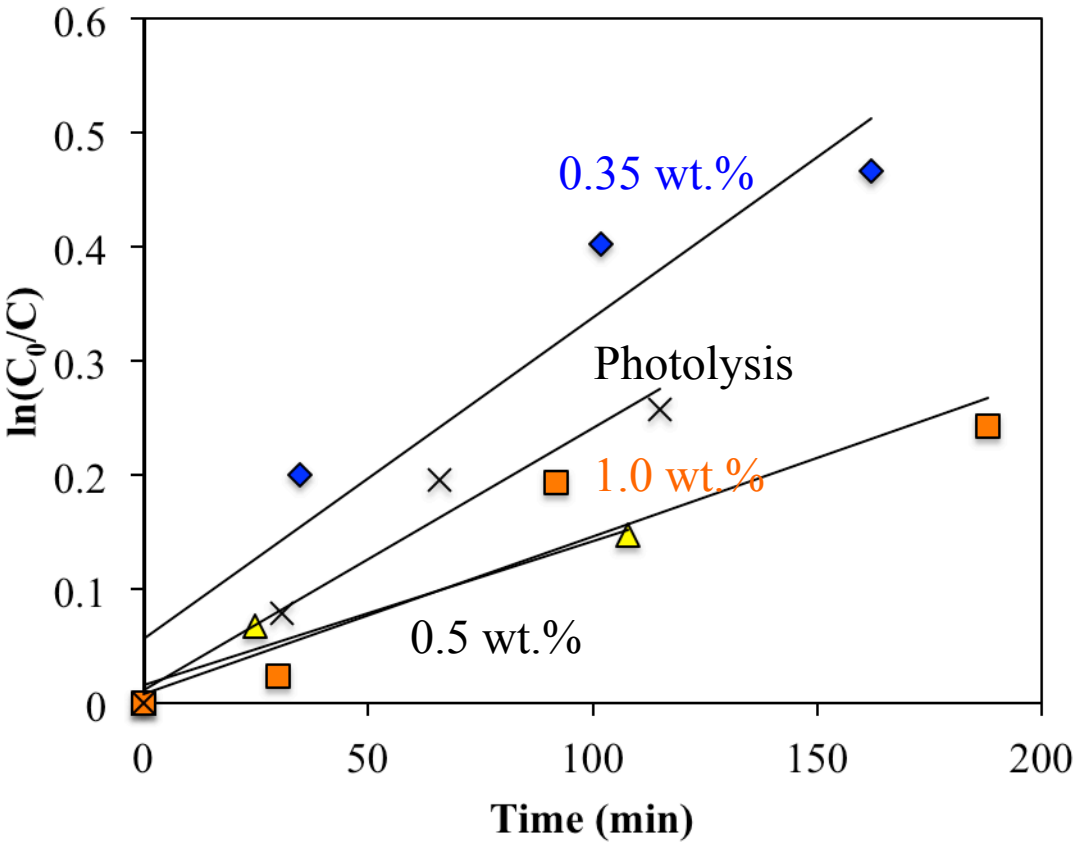

Figure 4.14: First order reaction determined by $\ln(C_0/C)$ versus time for titania nanotubes synthesized in 0.35, 0.5, and 1.0 wt.% sodium fluoride and photolysis.

The most likely cause for the increased photocatalytic activity of the amorphous titania nanotubes synthesized in low fluoride concentrations compared to Degussa P25 and rutile titania nanotubes is the increased adsorption of hydroxyls. Surface hydroxyl groups increase photocatalytic activity by preventing the recombination of electrons and holes [5] and increase the polarity of the photocatalyst surface for enhanced water adsorption [14]. The increased surface polarity allows for more water molecules from the aqueous methylene blue solution to adsorb to the surface so more of them can be split into hydrogen and oxygen. In addition, the ability of a photocatalyst to degrade methylene blue may also depend on the point of zero charge of the catalyst surface [13],

which is also dependent on the number of surface hydroxyls. The EDS data described earlier in this chapter supports the hypothesis that amorphous titania nanotubes synthesized in lower concentrations of sodium fluoride have higher concentrations of surface hydroxyls. The surface of the titania nanotubes were also less conductive, as measured by four-point sensing, which suggests increased hydroxyl group adsorption. It is also possible that the titania nanotubes synthesized in lower fluoride-containing electrolytes have fewer interstitial titanium atoms or fewer fluoride impurities; therefore, the titania nanotubes synthesized in 0.35 wt.% sodium fluoride are more photocatalytically active.

Varghese and coworkers observed that the greater the area of the nanotube rim at the surface of the array, pictured in Figure 4.1, the greater the photocurrent in titania nanotubes, which is a measure of photocatalytic activity. The titania nanotubes tested in the methylene blue degradation experiments were all synthesized with an applied electrical potential of 10 V and at varying time lengths so that the nanotubes were equal in length. However, if the rim area is calculated using the data in Figure 4.8 and the moles reacted are normalized by these areas, the resulting graph of moles reacted per area as a function of time in Figure 4.15 shows that the titania nanotubes synthesized in lower fluoride-containing electrolytes are more photocatalytically active than the nanotubes synthesized in higher sodium fluoride-containing electrolytes. The nanotubes synthesized in 0.5 and 1.0 wt.% sodium fluoride electrolyte show comparable activity to each other. Therefore, it can be concluded that a factor other than rim surface area is causing the increased photocatalytic activity of the titania nanotubes in lower fluoride-

containing electrolytes. This observation supports the hypothesis that the stoichiometry and number of adsorbed hydroxyl groups may cause the increased photocatalytic activity.

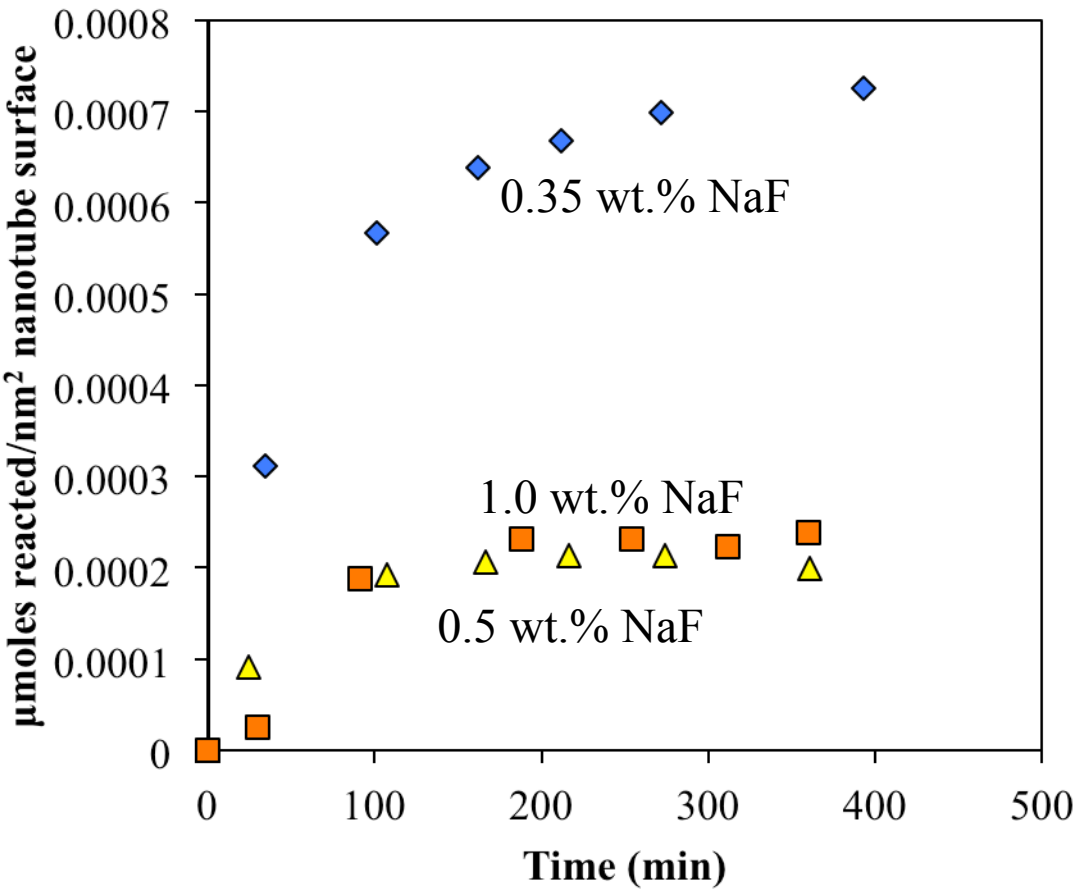

Figure 4.15: µmoles of methylene blue reacted normalized by titania nanotube rim surface area for nanotubes synthesized in 0.35, 0.5, and 1.0 wt.% sodium fluoride electrolyte.

4.7 Conclusions

Titania nanotubes offer a high surface area and dimensions that are tunable based on synthesis conditions. Oxygen content of amorphous nanotubes affects the properties of titania nanotubes, such as the conductivity of the nanotube array and the photocatalytic

activity. Titania nanotubes retain a nanotube structure at high temperatures allowing for the possibility of high surface area rutile catalyst supports. Lower fluoride concentrations in the synthesis electrolyte can be correlated to an apparent high oxygen to titanium ratio, which may be a measure of increased adsorbed hydroxyl groups. Titania nanotubes with high oxygen to titanium ratios were less conducting than titania nanotubes synthesized in higher fluoride concentrations. Titania nanotubes with a low oxygen to titanium ratio were synthesized in high fluoride-containing electrolytes may exhibit high conductivity due to titanium interstitials or due to fluoride substitutions.

References

[1] Gopal K. Mor, Oomman K. Varghese, Maggie Paulose, Karthik Shankar, Craig A. Grimes, A review on highly ordered, vertically oriented TiO_2 nanotube arrays: Fabrication, material properties, and solar energy applications, *Solar Energy Materials and Solar Cells* 90 (2006) 2011-2075.

[2] Jan M. Macak, Patrik Schmuki, Anodic growth of self-organized anodic TiO2 nanotubes in viscous electrolytes, *Electrochimica Acta* 52 (2006) 1258-1264.

[3] Gopal K. Mor, Karthik Shankar, Maggie Paulose, Oomman K. Varghese, and Craig A. Grimes, Enhanced Photocleavage of Water Using Titania Nanotube Arrays, *Nano Letters* 5 (2005) 191-195.

[4] A.N. Enyashin, A.L. Ivanovskii, Theoretical study of the structure and electronic properties of TiO nanotubes and nanowires, *Journal of Molecular Science* 766 (2006) 15-18.

[5] Masatoshi Nakamura, Shinichi Kato, Toru Aoki, Lucel Sirghi, and Yoshinori Hatanaka, Role of terminal OH groups on the electrical and hydrophilic properties of hydro-oxygenated amorphous TiOx :OH thin films, *Journal of Applied Physics* 90 (2001) 3391-3395.

[6] E. Ranney, J. Mansfield, K. Sun, and Johannes W. Schwank, Effects of synthesis conditions on dimensions, structure, and oxygen content of photocatalytically active titania nanotubes, *Journal of Materials Research* 25 (2010) 89-95.

[7] Christiaan Richter and Charles A. Schmuttenmaer, Exciton-like trap states limit electron mobility in TiO2 nanotubes, *Nature Nanotechnology* 5 (2010) 769-772.

[8] G. K. Mor, O. K. Varghese, M. Paulose, N. Mukherjee, and C.A. Grimes, Fabrication of tapered, conical-shaped titania nanotubes, *Journal of Materials Research* 18 (2003) 2588-2593.

[9] D. Gong, C. A. Grimes, O. K. Varghese, W. Hu, R. S. Singh, Z. Chen, and E.C. Dickey, Titanium oxide nanotube arrays prepared by anodic oxidation*, Journal of Materials Research* 16 (2001) 3331-3334.

[10] Qingyun Cai, Maggie Paulose, Oomman K. Varghese, and Craig A. Grimes, The effect of electrolyte composition on the fabrication of self-organized titanium oxide nanotube arrays by anodic oxidation, *Journal of Materials Research* 20 (2005) 230-236.

[11] J. Zhao, X. Wang, and L. Li, Electrochemical fabrication of well-ordered titania nanotubes in H3PO4/HF electrolytes, *Electronics Letters* 41 (2005) 771-772.

[12] Marshall D. Earle, The Electrical Conductivity of Titanium Dioxide, *Physical Review* 61 (1942) 56-62.

[13] Ammar Houas , Hinda Lachheb, Mohamed Ksibi, Elimame Elaloui, Chantal Guillard, Jean-Marie Herrmann, Photocatalytic degradation pathway of methylene blue in water, *Applied Catalysis B: Environmental* 31 (2001) 145–157.

[14] Masatoshi Nakamura, Toru Aoki, Yoshinori Hatanaka, Dariusz Korzec, and Jurgen Engemann, Comparison of hydrophilic properties of amorphous TiOx films obtained by radio frequency sputtering and plasma-enhanced chemical vapor deposition, *Journal of Materials Research* 16 (2001) 621-626.

Chapter 5

Sabatier Reaction and *in-situ* DRIFTS using Ru-Doped Titania Nanotube Photocatalyst

In this chapter, ruthenium-doped titania nanotubes for thermally catalyzing the Sabatier reaction are compared to Ru-impregnated Degussa P25 titanium dioxide and 0.5 wt.% Ru on alumina. Diffuse Reflectance Infrared Fourier Transform Spectrometry (DRIFTS) is used to investigate the mechanism by which the simultaneous water splitting and carbon dioxide methanation reactions occur under UV-illumination by Ru-doped titania nanotube photocatalyst. The mechanism developed based on this study is then compared to the Sabatier reaction using hydrogen as a reactant instead of water vapor with and without UV light illumination over Ru-doped titania nanotubes.

5.1 Characterization of Ruthenium-Doped Samples

X-ray photoelectron (XPS) spectra were recorded by a Kratos Axis Ultra XPS using a monochromatic Al source. Charge neutralization was provided by an AXIS Charge Balance System. Ti2p and O1s core levels were observed, and in the case of the Ru-doped titania nanotubes, Ru3p and Ru3d core levels were observed.

XPS verified that the ruthenium (III) chloride hydrate was reduced to metallic ruthenium. SEM equipped with EDS measured a loading of 2.3±0.3% ruthenium by

weight for doped titania nanotubes and a loading of 4.8±0.3% ruthenium by weight for impregnated Degussa P25.

The Ru-doped titania nanotubes had a BET surface area of 99±1 m^2/g and the Degussa P25 had a BET surface area of 46±1 m^2/g. Figure 5.1 shows an SEM image of doped anatase titania nanotubes. No large particles of ruthenium were observed on the surface of the titania nanotube array. Hydrogen and carbon monoxide chemisorption measurements were unsuccessful for measuring particle ruthenium particle size in titania nanotubes since the amount of ruthenium was below operating limits. X-ray Diffraction measurements were also unsuccessful for determining particle size indicating that the ruthenium particles in titania nanotubes were less than 10 nm in diameter. Carbon monoxide chemisorption measurements of Ru-impregnated Degussa P25 indicated that the ruthenium particle size was 9.9±0.1 nm with 14.5% dispersion with a metal surface area of approximately 49.5 m^2/g.

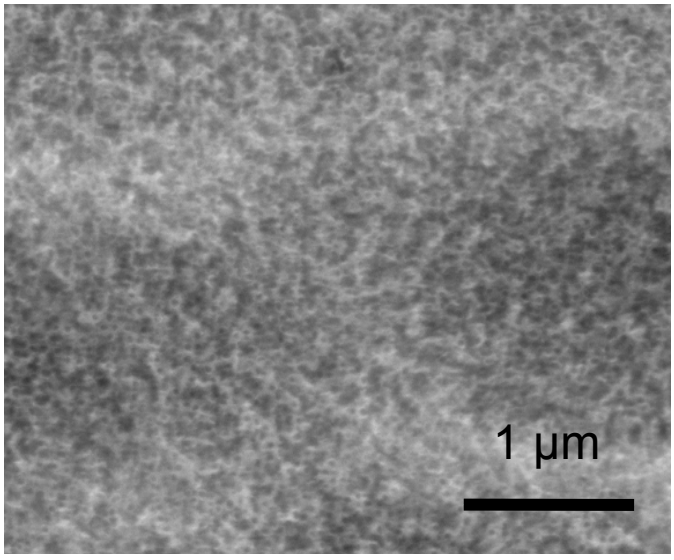

Figure 5.1: SEM image of the top view of a Ru-doped titania nanotube array. No large ruthenium particles are observed.

5.2 The Sabatier Reaction

The Sabatier reaction was conducted in the tubular stainless steel reactor described in Chapter 3. Catalysts tested were 3.5 grams of 0.5 wt.% Ru-alumina pellets, 13.5 mg (geometric area of 16 cm^2) anatase titania nanotubes, 13.5 mg (geometric area of 16 cm^2) Ru-doped titania nanotubes, 0.4 grams Degussa P25 Titanium Dioxide, and 0.4 grams Ru-impregnated Degussa P25 titanium dioxide. The reactions took place at 200-600°C. The catalysts were added to the tubular reactor with quartz wool to increase mixing of gases. Pre-purified nitrogen flowed through the reactor until the reactor jacket reached the temperature set-point. Once the set-point was reached, the reaction gases were added.

The reactor feed consisted of 28.6% carbon dioxide by volume (20 sccm), 57.1% hydrogen by volume (40 sccm), and the balance nitrogen (10 sccm) as an internal gas standard. The H_2:CO_2 ratio in the gas feed was 2:1, which is sub-stoichiometric (a stoichiometric H_2:CO_2 gas feed would be 4:1). The hydrogen generated from water would also be sub-stoichiometric (assuming 45% conversion of water to hydrogen, the H_2:CO_2 ratio for the simultaneously occurring Sabatier reaction would be approximately 0.4:1), so the sub-stoichiometric feed was chosen to better predict the outcome of the concurrent reactions. The approximate space time velocity was 1.5 min^{-1}.

Carbon dioxide methanation was performed in a tubular flow reactor and in the absence of UV light and water feed using 0.5 wt% Ru on alumina pellet catalyst as a baseline as well as Ru-doped titania nanotube catalyst and Ru-impregnated Degussa P25 titanium dioxide catalyst. Figure 5.2 shows that the 0.5 wt.% Ru on alumina catalyst

allowed for equilibrium conversion of carbon dioxide to methane between 200-600°C. Ruthenium-doped titania nanotubes successfully converted carbon dioxide to methane between 200-600°C, but equilibrium conversion was not achieved except at 450°C. This result indicates that Ru-doped titania nanotubes can act as a catalyst for the thermal Sabatier reaction. Ruthenium-impregnated Degussa P25 acted as a poor Sabatier catalyst compared to Ru-alumina and Ru-doped titania nanotube catalysts. The Ru-doped titania nanotube arrays acted as a more effective Sabatier catalyst most likely because it has approximately double the surface area of the Ru-impregnated Degussa P25. Reactions that took place with only the quartz wool and no catalyst inside the plate reactor did not generate hydrogen; therefore, the stainless steel reactor tube did not play a role in catalyzing the Sabatier reaction.

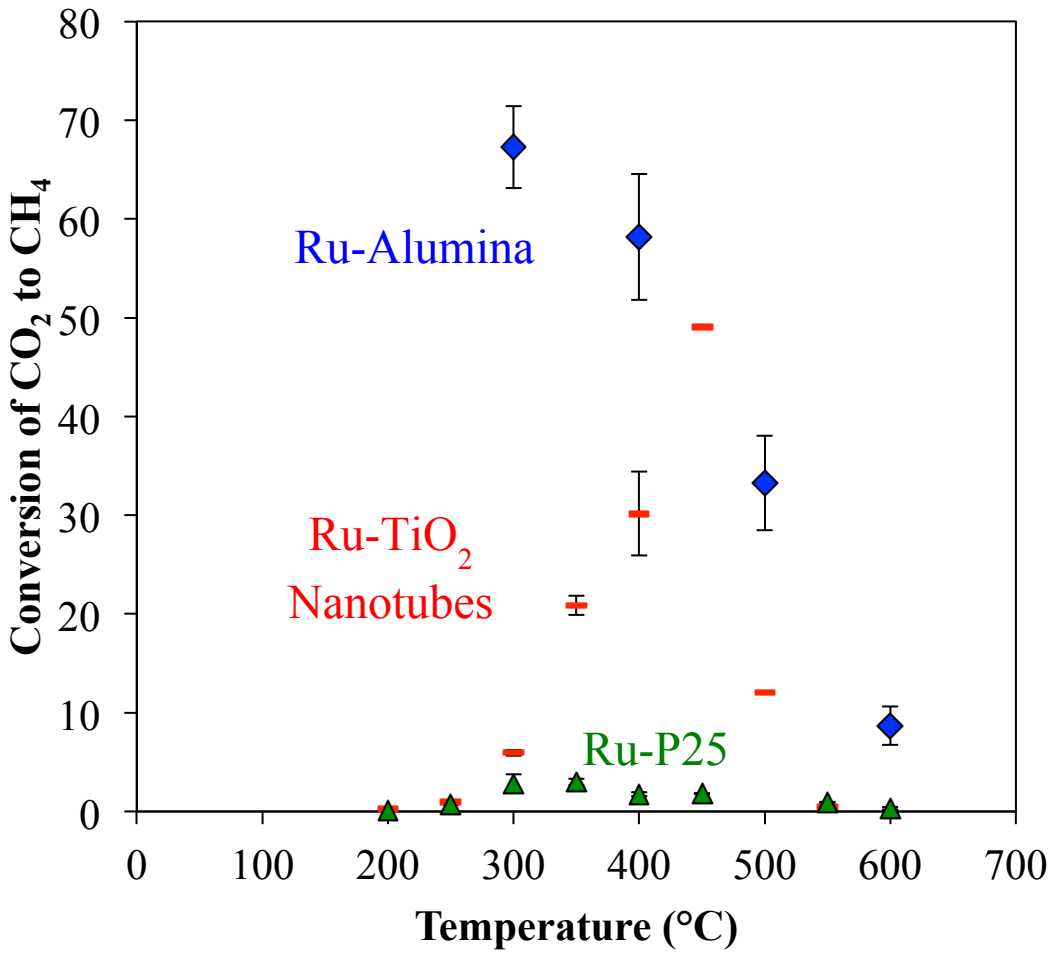

Figure 5.2: Percent conversion of carbon dioxide to methane as a function of reactor temperature for 0.5 wt.% ruthenium on alumina pellets, Ru-doped titania nanotubes, and Ru-impregnated Degussa P25.

The difference in the behavior of Ru-doped titania nanotubes and 0.5 wt.% Ru on alumina pellets as Sabatier catalysts can be explained mostly by the mechanisms by which they catalyze carbon dioxide methanation. Formic acid is an intermediate product and reactant when using Ru-doped titania nanotubes as a Sabatier catalyst. Adsorbed carbon dioxide directly reacts with two adsorbed protons to form the formic acid intermediate. The formic acid further reacts with adsorbed protons to form carbon monoxide and water. Adsorbed protons can also reduce the formic acid to formate on the

surface of the Ru-doped titania nanotube array. This undesired product can inhibit the methanation reaction. The following reaction scheme was suggested by Prairie, et al. [1]:

$$CO_2(g) \rightarrow CO_{2ad} \quad (5.1)$$

$$H_2(g) \rightarrow 2H_{ad} \quad (5.2)$$

$$CO_{2ad} + 2H \rightarrow HCOOH_{ad} \quad (5.3)$$

$$HCOOH \rightarrow H_{ad} + HCOO^-_{ad} \quad (5.4)$$

$$HCOOH_{ad} \rightarrow CO_{ad} + H_2O_{ad} \quad (5.5)$$

$$H_2O_{ad} \rightarrow H_2O(g) \quad (5.6)$$

$$2CO_{ad} \rightarrow C_{ad} + CO_2(g) \quad (5.7)$$

$$C_{ad} + H_{ad} \rightarrow CH_{ad} \quad (5.8)$$

$$CH_{ad} + H_{ad} \rightarrow CH_{2ad} \quad (5.9)$$

$$CH_{2ad} + H_{ad} \rightarrow CH_{3ad} \quad (5.10)$$

$$CH_{3ad} + H_{ad} \rightarrow CH_4(g) \quad (5.11)$$

First, carbon dioxide is adsorbed onto the surface of the Ru-doped titania nanotubes. Hydrogen adsorbs and dissociates onto the surface of the Ru-doped titania nanotubes. The adsorbed carbon dioxide then reacts with the adsorbed protons to form formic acid. The formic acid dissociates to adsorbed formate and adsorbed protons or to adsorbed carbon monoxide and water. The water desorbs from the surface and the carbon monoxide reacts with another adsorbed carbon monoxide to form adsorbed carbon and gaseous carbon dioxide. The adsorbed carbon then reacts with the adsorbed protons to form CH, CH_2, and CH_3 intermediates and finally forms methane.

Formic acid and formate, however, are not formed when using 0.5 wt.% Ru on alumina pellets as a carbon dioxide methanation catalyst. Instead of using a formic acid intermediate, the Ru on alumina catalyst catalyzes the direct reduction of carbon dioxide to the carbon monoxide intermediate. The following mechanism for carbon dioxide methanation over Ru-alumina catalyst is suggested [2]:

$$CO_2(g) \rightarrow CO_{2ad} \quad (5.1)$$

$$CO_{2ad} \rightarrow CO_{ad} + O_{ad} \quad (5.12)$$

$$H_2(g) + O_{ad} \rightarrow H_2O_{ad} \quad (5.13)$$

$$H_2O_{ad} \rightarrow H_2O(g) \quad (5.6)$$

$$CO_{ad} \rightarrow CO(g) \quad (5.14)$$

$$2CO_{ad} \rightarrow C_{ad} + CO_2(g) \quad (5.7)$$

$$C_{ad} + H_{ad} \rightarrow CH_{ad} \quad (5.8)$$

$$CH_{ad} + H_{ad} \rightarrow CH_{2ad} \quad (5.9)$$

$$CH_{2ad} + H_{ad} \rightarrow CH_{3ad} \quad (5.10)$$

$$CH_{3ad} + H_{ad} \rightarrow CH_4(g) \quad (5.11)$$

First, carbon dioxide adsorbs onto the Ru-doped titania nanotube surface and dissociates to adsorbed carbon monoxide and oxygen. The adsorbed carbon monoxide was also observed during the DRIFTS studies. The carbon monoxide can desorb from the catalyst surface or it can react with another adsorbed carbon monoxide to form adsorbed carbon and carbon dioxide gas. The adsorbed carbon then reacts with the adsorbed protons to form CH, CH_2, and CH_3 intermediates and finally forms methane.

Post-reaction SEM imaging of the Ru-doped titania nanotubes showed large depositions of carbon for nanotubes that catalyzed the Sabatier reaction above 450°C. Figure 5.3 shows a large carbon deposition on top of the Ru-doped titania nanotube array, which indicates that carbon deposition may also inhibit the Sabatier reaction at high temperatures. Figure 5.4 shows large ruthenium particles on the surface of the titania nanotube array after participating in reactions above 500°C. This suggests possible sintering of the ruthenium due to high reaction temperatures.

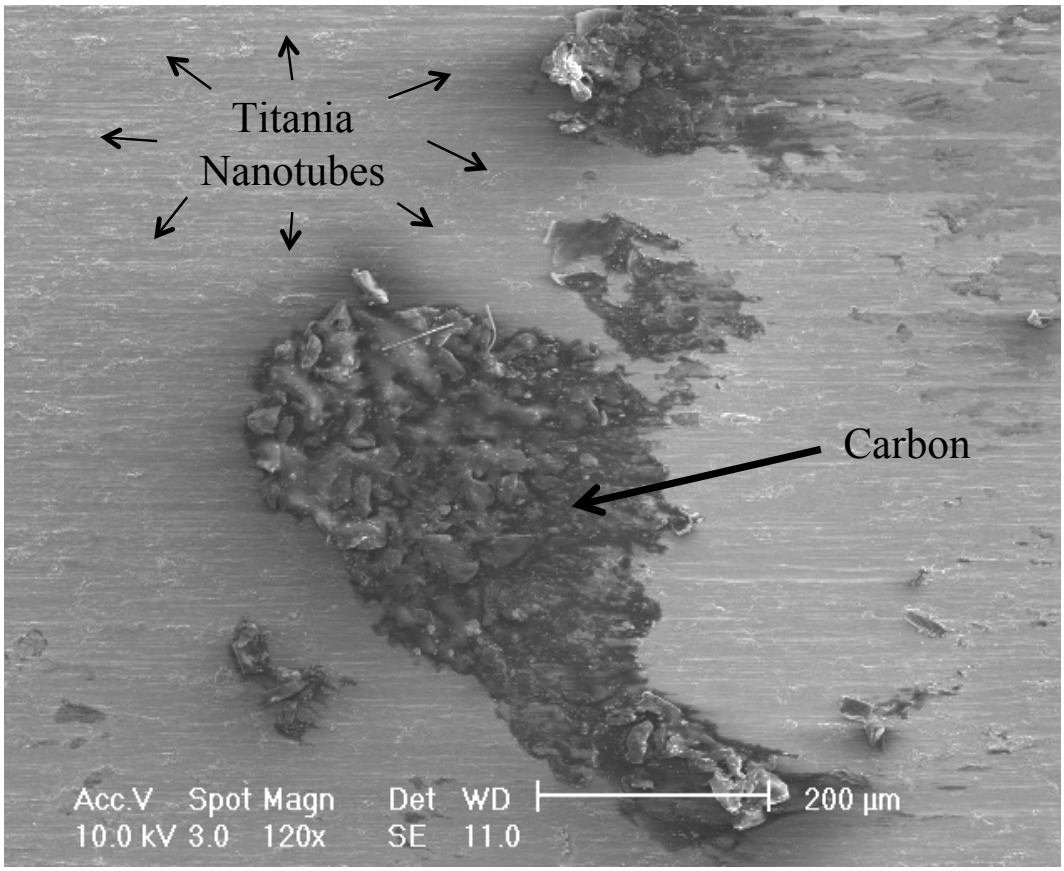

Figure 5.3: SEM image of the solid carbon deposition on the surface of a titania nantoube array resulting from the Sabatier reaction at 500°C.

In addition, the catalyst shape may influence the gas flow characteristics in the tubular reactor, which could also impact catalyst performance. The Ru-doped titania nanotube arrays were placed in the tubular reactor parallel to the direction of gas flow. The Ru-alumina catalyst, however, was in pellet form, so the active sites may have been more accessible to the reactants.

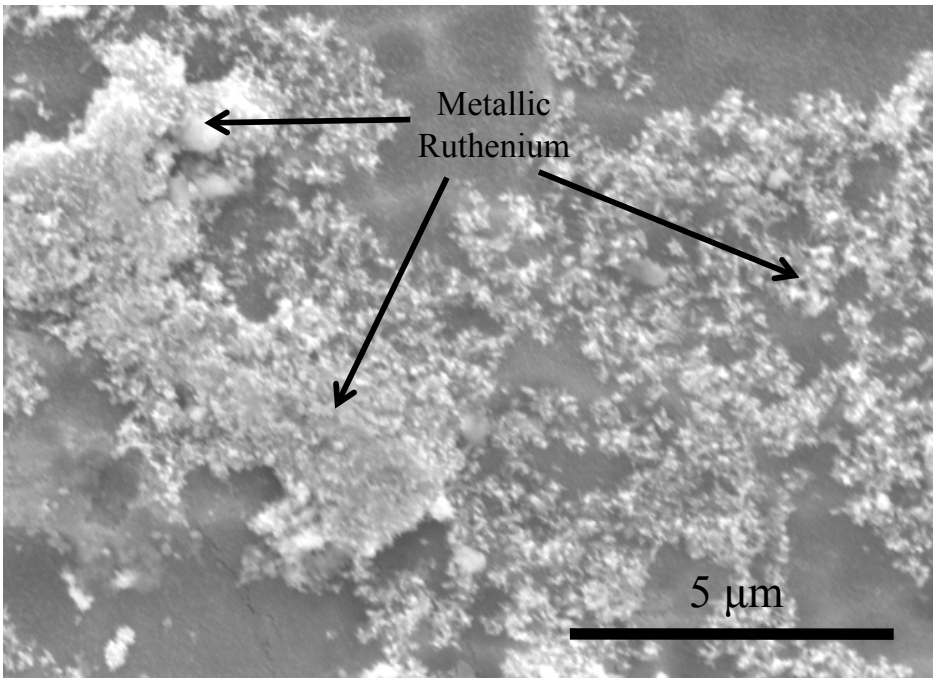

Figure 5.4: Metallic ruthenium particles on the surface of the titania nanotube array after use as a catalyst for the Sabatier reaction at 500°C. The agglomeration of these particles suggests sintering.

The accessibility of the ruthenium sites may also explain the difference in catalyst behavior. The titania nanotubes could be considered "doped" because the small ruthenium particles were dispersed within the length of the nanotubes. As a result, not all of the ruthenium particles were on the surface of the arrays. The 0.5 wt.% Ru-alumina pellets consisted of large ruthenium particles on the surface of the alumina, but not within the alumina. As a result, the Ru-doped titania nanotubes did not perform as well as Ru-

alumina pellets for the Sabatier reaction. However, the titania nanotubes can still be used as a thermal methanation catalyst and the "doped" nature of the nanotubes could improve their photocatalytic ability when UV light is introduced.

5.3 Diffuse Reflectance Infrared Fourier Transform Spectrometry of Simultaneous Water Splitting and Carbon Dioxide Methanation

Diffuse Reflectance Infrared Fourier Transform Spectrometry (DRIFTS) experiments were performed to study simultaneous water splitting and carbon dioxide methanation *in situ*. The reaction chamber equipped with two ZnSe windows and one quartz window described in Chapter 3 was evacuated to 1 X 10^{-4} torr while containing catalyst. Argon was introduced into the reaction chamber followed by background gas phase subtraction. After the background was subtracted, the reaction chamber was again evacuated before the reaction gases were introduced. Reactions over Ru-doped anatase titania nanotubes with added activated carbon were studied in the presence of 365 nm UV light and in the dark. The geometric surface area of titania nanotubes studied was 1 cm^2, which was approximately 0.85 mg of titania. About 2 mg of activated carbon was added to the reaction chamber as an absorbant for oxygen to reduce the recombination of hydrogen and oxygen in the water splitting reaction. The goal was to prevent the combustion of methane back to carbon dioxide so that greater amounts of methane can be measured. The motivation behind adding activated carbon will be discussed in greater detail in Chapter 6.

In the case of simultaneous water splitting and carbon dioxide methanation, 150 torr carbon dioxide and 590 torr nitrogen that contained saturated water vapor (20 torr at

25°C) at atmospheric pressure was introduced into the reaction chamber under UV light. The reaction intermediates and products were measured at temperatures between 25 and 100°C.

After filling the reaction chamber with 20 torr water vapor, 150 torr carbon dioxide, and 590 torr nitrogen, no adsorption of carbon dioxide onto the surface of Ru-doped titania nanotubes was observed at 25°C and in the absence of UV light. Upon introduction of UV light, the absorption of carbon dioxide onto the Ru-titania nanotube surface was observed as seen in Figure 5.5. Adsorption of water vapor was also observed at 1595 cm^{-1}.

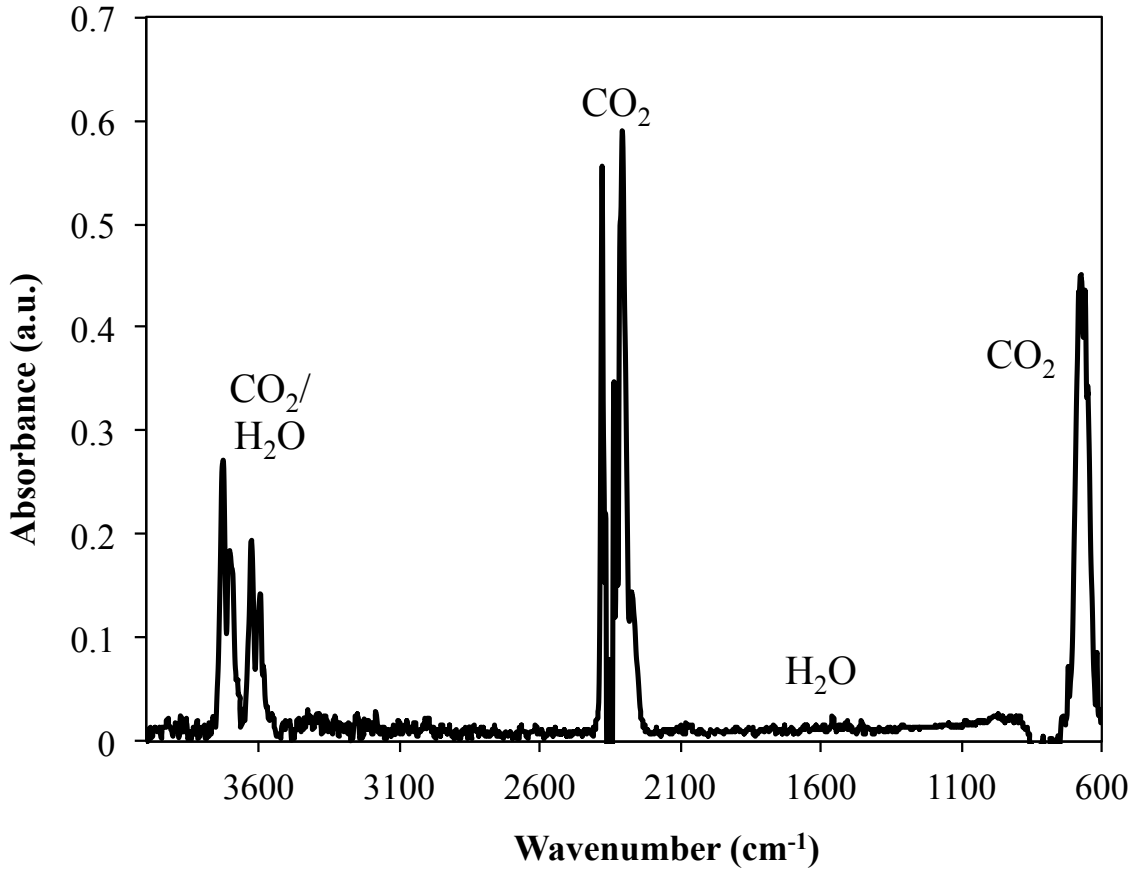

Figure 5.5: Absorbance as a function of wavelength shows the adsorption of carbon dioxide and water vapor onto the Ru-doped titania nanotubes at 25°C under UV light illumination.

When the Ru-doped titania nanotube catalyst temperature was increased to 50°C under UV light, the broad O-H stretch band appeared between 3200-3400 cm^{-1}, the amide C=O stretch band appeared at 1650 cm^{-1}, and the carbon dioxide adsorption bands remained as seen in Figure 5.6. The formation of the O-H stretch indicates that water was successfully converted to hydrogen and adsorbed hydroxyls. The amide C=O stretch band may indicate that nitrogen may be adsorbed to the surface of the Ru-doped titania nanotubes since it was one of the gases in the reaction chamber and that nitrogen aids the reduction of carbon dioxide on the surface.

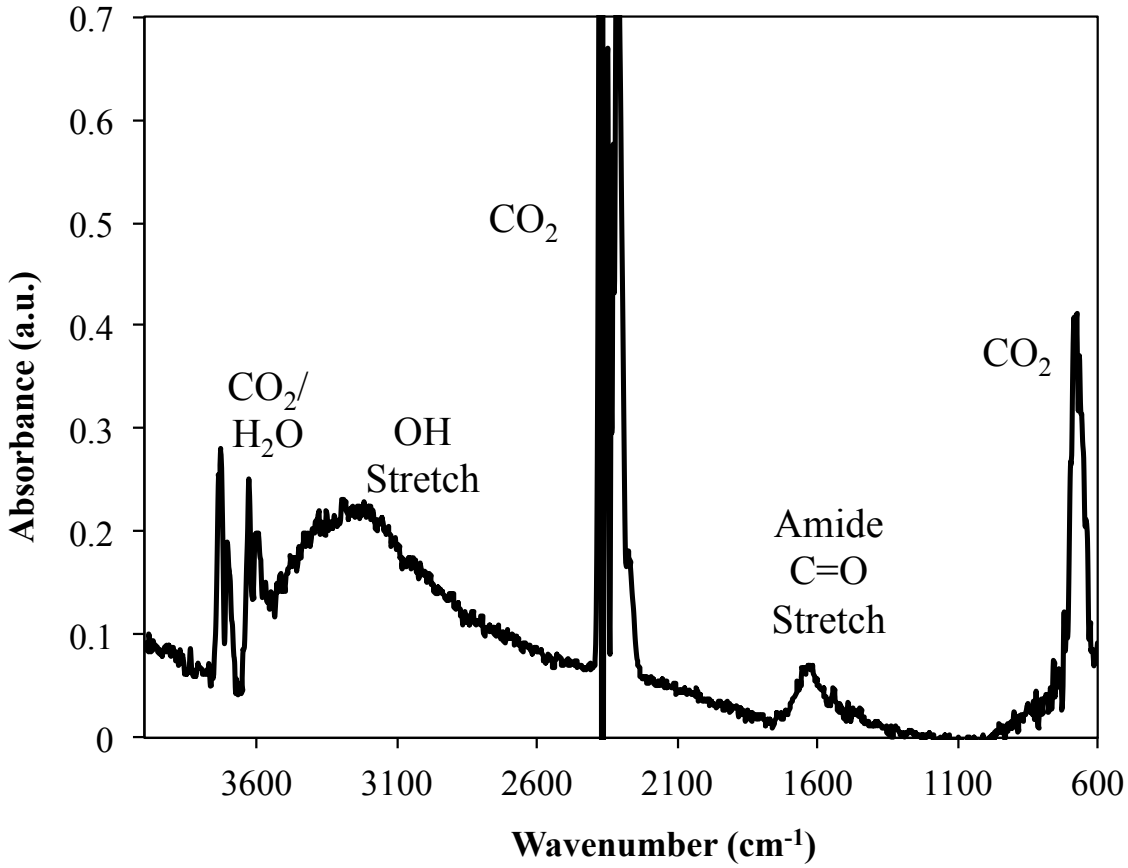

Figure 5.6: Absorbance as a function of wavelength shows the adsorption of carbon dioxide onto the Ru-doped titania nanotubes at 50°C under UV light illumination. The amide stretch and O-H stretch can also be observed.

The amide C=O stretch may also suggest that the Ru-doped titania nanotubes are "doped" with nitrogen. The presence of nitrogen in the titania nanotubes has been observed during EDS and XPS studies. Varghese and coworkers observed nitrogen doping in titania nanotubes as a result of nitrogen present during synthesis. Varghese also hypothesizes that nitrogen can be adsorbed by titania nanotubes during exposure to air [3]. In addition, the ruthenium was reduced in nitrogen at high temperatures, so it is possible that nitrogen was incorporated into the titania structure. The peak at approximately 1650 cm^{-1} suggests that the nitrogen was in an amide form; however, it is

unclear how the nitrogen became an amide. This could suggest that there is a chemical interaction between the activated carbon and the active sites of the catalyst. Nitrogen could also be adsorbed by the ruthenium itself.

When the Ru-doped titania nanotube catalyst temperature was increased to 65°C in the presence of UV light, the O-H and amide C=O stretch bands disappeared and the formation of methane was observed at ~1300 cm^{-1} as seen in Figure 5.7. The methane band continued to be present when the catalyst temperature was increased to 75°C and 100°C.

It is important to note that in the absence of UV light at 50°C and 65°C, the Ru-doped titania nanotube catalyst only adsorbed carbon dioxide and water. Carbon monoxide and methane were not observed until the reactor chamber was heated to 200°C in the absence of UV light, which is consistent with the Sabatier experiments using the tubular reactor described in Section 5.2 of this chapter.

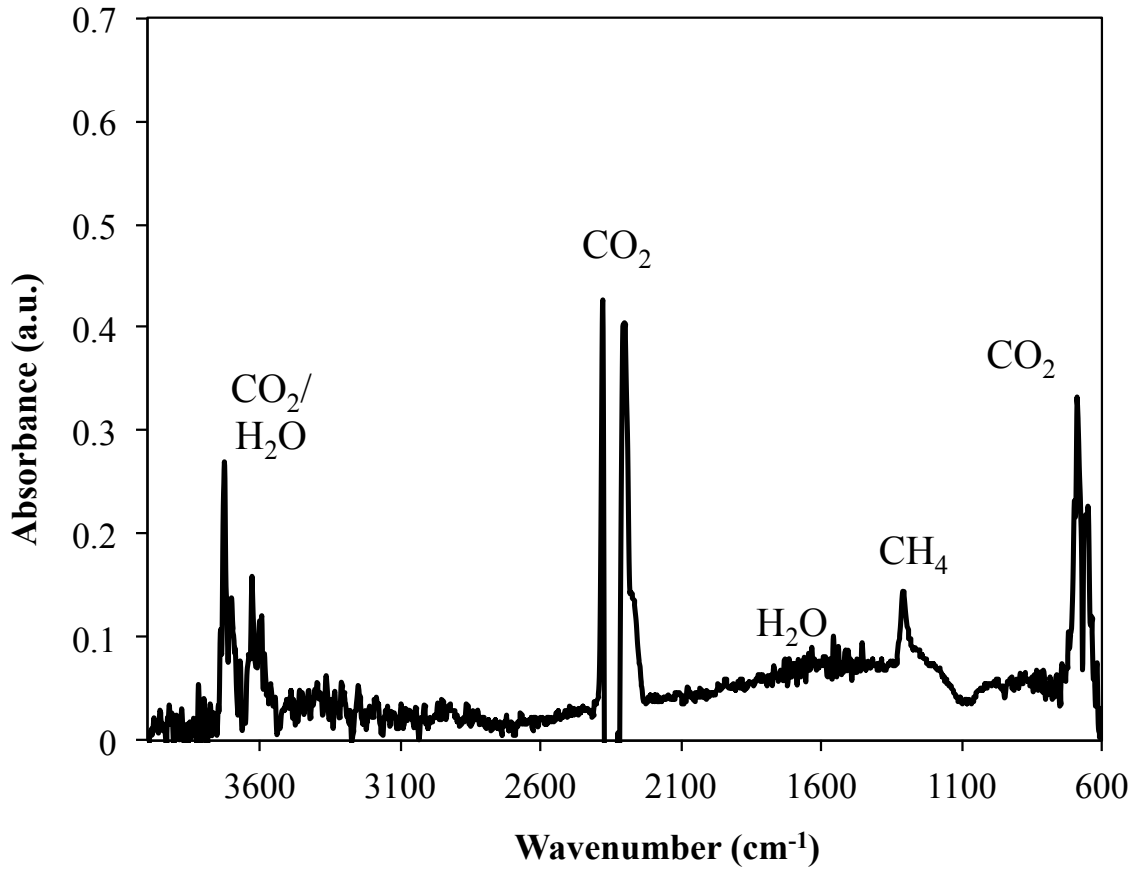

Figure 5.7: Absorbance as a function of wavelength shows the adsorption of carbon dioxide and methane onto the Ru-doped titania nanotubes at 65°C under UV light illumination.

The DRIFTS study of simultaneous water splitting and carbon dioxide methanation using Ru-doped titania nanotubes under UV light suggests that the mechanism involves a carbon monoxide intermediate. As discussed in previously in this chapter, the Sabatier reaction involves a formic acid intermediate when using a Ru-doped titania nanotube catalyst in the absence of UV light. Ru-alumina catalyst, in contrast, reduces carbon dioxide directly to carbon monoxide without a formic acid intermediate and as a result, the Ru-alumina catalyst is more effective for the Sabatier reaction.

The DRIFTS studies suggest that introducing UV light to the water splitting and Sabatier reaction over Ru-doped titania nanotubes allows for the direct reduction of carbon dioxide to carbon monoxide without a formic acid intermediate since formic acid was not observed. This result is significant because it demonstrates how a chemical reaction pathway can be altered by UV light exposure and shows the successful simultaneous water splitting and carbon methanation reaction using Ru-doped titania photocatalyst. Since DRIFTS experiments measured adsorbants on a small area of Ru-doped titania nanotube catalyst surface, they may not have captured the surface chemistry of the activated carbon. As a result, the measurements only describe the reaction mechanisms on the surface of the Ru-doped titania nanotubes.

In addition, methane can be formed at 65°C, which is a significantly lower temperature than the typical Sabatier reaction range of 200-600°C. The gas chromatography studies previously in this chapter showed that only a small amount of methane was formed at 200°C and no methane was observed below 200°C. This observation could suggest that the methane does not readily desorb from the Ru-doped titania nanotube surface at lower temperatures since the methane band did not disappear upon increasing the surface temperature to 100°C.

The formation of methanol from carbon dioxide and water has been documented in previous work [4-5] using titania-based catalysts under UV light illumination. A methanol IR band was not observed between 1400-1500 cm^{-1}, which indicates that the water splitting and Sabatier reaction does not include a methanol intermediate when using Ru-doped titania nanotube photocatalyst. The proposed reaction mechanism of

simultaneous water splitting and carbon dioxide methanation over Ru-doped titania nanotubes in the presence of UV light is the following:

$$[Ti^{4+}—O^{2-}]+h\nu \rightarrow h^{+} + e^{-} + [Ti^{3+}—O^{-}] \quad (5.15)$$

$$H_2O(g) \rightarrow H_2O_{ad} \quad (5.16)$$

$$H_2O_{ad} + h^{+} \rightarrow OH_{ad} + H_{ad} \quad (5.17)$$

$$OH_{ad} + H_2O_{ad} + 3h^{+} \rightarrow O_2 + 3H_{ad} \quad (5.18)$$

$$CO_2(g) \rightarrow CO_{2ad} \quad (5.1)$$

$$CO_{2ad} \rightarrow CO_{ad} + O_{ad} \quad (5.12)$$

$$CO_{ad} \rightarrow CO(g) \quad (5.14)$$

$$2CO_{ad} \rightarrow C_{ad} + CO_2(g) \quad (5.7)$$

$$C_{ad} + H_{ad} \rightarrow CH_{ad} \quad (5.8)$$

$$CH_{ad} + H_{ad} \rightarrow CH_{2ad} \quad (5.9)$$

$$CH_{2ad} + H_{ad} \rightarrow CH_{3ad} \quad (5.10)$$

$$CH_{3ad} + H_{ad} \rightarrow CH_4(g) \quad (5.11)$$

The first step is the dissociation of electrons and holes in the titania due to UV light exposure. Water vapor is adsorbed onto the titania surface and reacts with a hole to form adsorbed hydroxyls and protons. The adsorbed hydroxyls were observed during the DRIFTS studies. The adsorbed hydroxyl reacts with adsorbed water and holes to form oxygen and adsorbed hydrogen. Simultaneously, carbon dioxide adsorbs onto the Ru-doped titania nanotube surface and dissociates to adsorbed carbon monoxide and oxygen. The adsorbed carbon monoxide was also observed during the DRIFTS studies. The carbon monoxide can desorb from the catalyst surface or it can react with another

adsorbed carbon monoxide to form adsorbed carbon and carbon dioxide gas. The adsorbed carbon then reacts with the adsorbed protons to form CH, CH_2, and CH_3 intermediates and then finally forms methane.

To further study the reaction mechanism, a DRIFTS study was performed on the Sabatier reaction using hydrogen as a reactant instead of water vapor. To study the Sabatier reaction mechanism without water splitting over Ru-doped titania nanotubes with and without UV light, the reaction chamber was filled with 220 torr carbon dioxide, 440 torr hydrogen, and 100 torr nitrogen. Without UV light, carbon monoxide intermediate forms at 250°C and methane appears at 300°C. Only adsorbed carbon dioxide was observed at temperatures below 200°C. When UV light wa introduced to the ZnSe reaction chamber containing fresh reactant gases, methane was observed at 150°C. The carbon monoxide reaction intermediate was observed at approximately 1560 cm^{-1} in addition to a O-H stretch band at 100°C. This indicates that the UV light converts the water formed from the Sabatier reaction into hydrogen and hydroxyls on the Ru-doped titania nanotube surface. Formic acid was not observed, suggesting that UV illumination of the Ru-titania nanotube catalyst prevented the formation of formic acid intermediates thus altering the reaction mechanism by promoting the direct reduction of carbon dioxide to carbon monoxide.

In addition, the adsorption of CO_2 from the air was measured in the presence and absence of UV light. In these experiments, the reaction chamber was removed allowing the Ru-doped titania nanotube catalyst to be exposed air in the room. The adsorption of carbon dioxide from the air was measured in the absence and presence of UV light illumination. The room was at a temperature of approximately 20°C.

The DRIFTS study provides evidence that carbon dioxide adsorption onto the surface of Ru-doped titania nanotubes is enhanced by exposure to UV light. Figure 5.8 shows the carbon dioxide adsorption band when exposed to carbon dioxide in the atmosphere in the absence of UV light. Figure 5.8 also shows an increase in carbon dioxide adsorption when exposed to the atmosphere under UV light. This result, although not quantitative, indicates that UV light can assist the adsorption of carbon dioxide onto the surface of Ru-doped titania nanotubes, which suggests that UV light can impact reaction mechanisms.

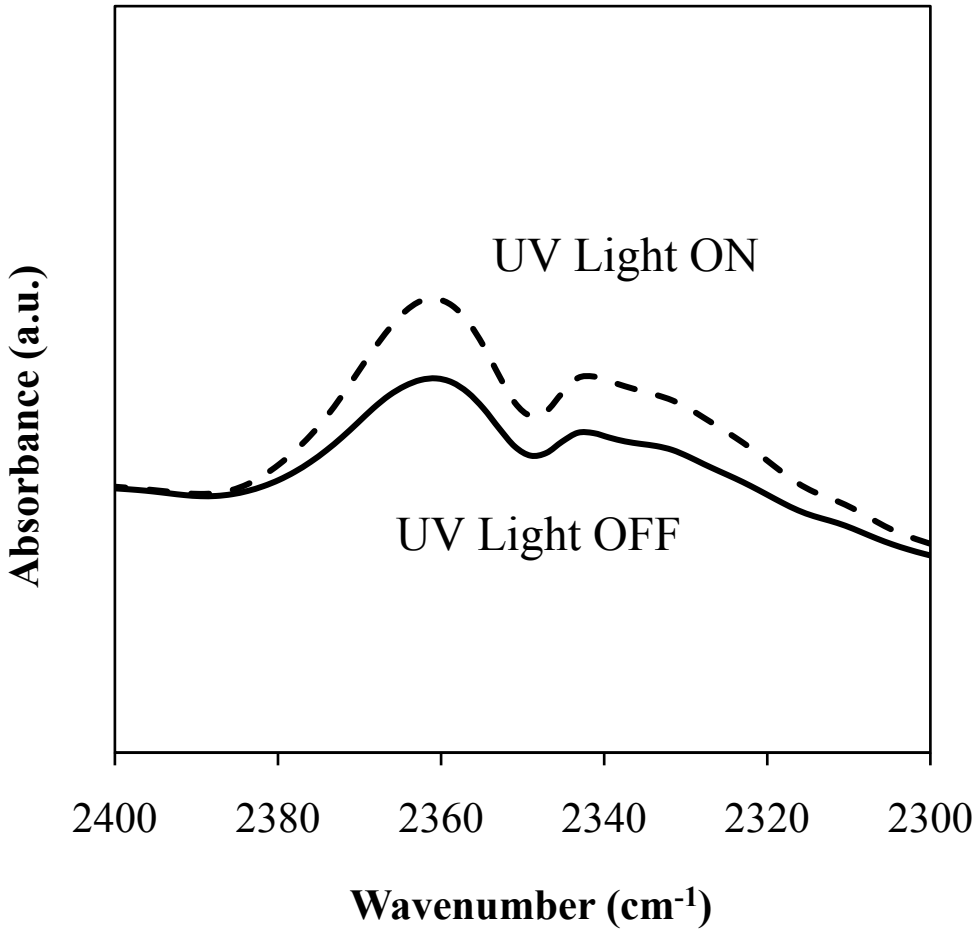

Figure 5.8: Increased adsorption of carbon dioxide on Ru-doped titania nanotubes when exposed to air under UV light illumination.

Since the enhanced adsorption of carbon dioxide onto the Ru-doped titania nanotube surface was not done in a controlled environment, further studies should be done using the reaction chamber to better quantify these data. Performing these reactions in a controlled environment would also eliminate variable room temperatures and humidity.

5.4 Conclusions

Titania nanotubes were doped with metallic ruthenium. Titania nanotubes can be used as a metal support for ruthenium for the catalysis of the Sabatier reaction in the absence of UV light between 200-600°C. *In-situ* DRIFTS studies proved that the simultaneous water splitting and carbon dioxide methanation reaction occurs using Ru-doped titania nanotubes and activated carbon when illuminated by UV light. Methane formed via a CO intermediate bonded to a nitrogen atom, suggesting that nitrogen adsorption is an important step in the mechanism or that the titania nanotubes are also doped with nitrogen. The amide CO intermediate formed at 50°C and methane formed at 65°C, which is below the temperature at which methane was measured by GC during the Sabatier reaction.

References

[1] M.R. Prairie, A. Renken, J.G. Highfield, K.R. Thampi, M. Grätzel, A Fourier Transform Infrared Spectroscopic Study of CO_2 Methanation on Supported Ruthenium, *Journal of Catalysis* 129 (1991) 130-144.

[2] Yvonne Traa and Jens Weitkamp, Kinetics of the Methanation of Carbon Dioxide over Ruthenium on Titania, *Chemical Engineering and Technology* 21 (1999) 4 291-293.

[3] Oomman K. Varghese, Maggie Paulose, Thomas J. LaTempa, and Craig A. Grimes, High-Rate Solar Photocatalytic Conversion of CO_2 and Water Vapor to Hydrocarbon Fuels, *Nano Letters* 9 (2009) 731-737.

[4] B. Aurian-Blajeni, M. Halmann, and J. Manassen, Photoreduction of carbon dioxide and water into formaldehyde and methanol on semiconductor materials, *Solar Energy* 25 (1980) 165-170.

[5] Yoshiumi Kohno, Hiroki Hayashi, Sakae Takenaka, Tsunehiro Tanaka, Photo-enhanced reduction of carbon dioxide with hydrogen over Rh/TiO_2, *Journal of Photochemistry and Photobiology A: Chemistry* 126 (1999) 117-123.

Chapter 6

Photocatalytic Water Splitting

Titania nanotubes doped with ruthenium were chosen for the water splitting and possible carbon dioxide methanation simultaneous reactions. In this Chapter, hydrogen generation by photocatalytic water splitting is discussed using Ru-doped anatase titania nanotubes, Ru-doped amorphous titania nanotubes, un-doped anatase titania nanotubes, Ru-impregnated Degussa P25 titanium dioxide, and Degussa P25 titanium dioxide. Significant improvements to hydrogen generation are made to the water splitting reaction by the physical addition of activated carbon to the two-dimensional quartz plate reactor discussed in Chapter 3. Finally, a mechanism for the deactivation of the water splitting reaction as well as the limitations of the activated carbon/Ru-doped titania nanotube system are discussed.

6.1 Photocatalytic Water Splitting

The quartz plate reactor described in Chapter 3 was used for photocatalytic water splitting experiments. Photocatalysts tested were Ru-doped anatase nanotube samples with a geometric surface area of 7 cm^2 (6 mg), Ru-doped amorphous titania nanotubes with a geometric surface area of 7 cm^2 (6 mg), un-doped anatase nanotubes with a geometric surface area of 7 cm^2 (6 mg), 0.4 g Ru-impregnated Degussa P25 titanium

dioxide, and 0.4 g Degussa P25 titanium dioxide. Mass flow controllers regulated the feed gases except for water vapor. Quartz wool was placed near the internal inlet and outlet of the quartz plate reactor to promote mixing. Pre-purified nitrogen flowed through the reactor until the reactor reached the temperature set-point. Approximately thirty minutes after the set-point was reached, the reaction gases were added. A stream of 20% carbon dioxide by volume (10 sccm) and the balance nitrogen (40 sccm) flowed through a saturator at 25°C so that the feed stream into the plate reactor contained 20 torr water vapor, 150 torr carbon dioxide, and the 590 torr nitrogen. The approximate space time velocity was 2 min^{-1}. After twenty minutes, the UV light was incorporated perpendicular to the catalyst surface. The reactions took place at 25-150°C.

Ruthenium-doped anatase titania nanotube arrays were found to be the most effective photocatalyst for the water splitting reaction under UV light. This material produced hydrogen at a maximum rate of 27.1±1.3 μmol/h•cm^2 at 75°C. The rate translates to approximately 2.5±0.1% conversion of water to hydrogen. This percentage conversion is consistent with most photocatalytic water splitting work to date. Ru-doped amorphous nanotubes also acted as a photocatalyst, but could not produce hydrogen at a rate higher than 6.4±1.5 μmol/h•cm^2 at a temperatures between 50°C and 75°C. This rate translates to approximately 0.6% conversion of water to hydrogen. Anatase titania nanotubes without ruthenium also demonstrated little photocatalytic activity between 25°C and 150°C. The maximum hydrogen production rate was approximately 5.3±4.6 μmol/h•cm^2 at 25°C, which represents approximately 0.5±0.4% conversion of water to hydrogen. The high error associated with these measurements indicates that the low measurements of hydrogen were barely above the detection limits of the gas

chromatograph and that un-doped anatase nanotube arrays are poor photocatalysts. It is also important to note that the rates reported are normalized by the geometric area of the titania nanotube array illuminated by UV light. Finally, Ru-impregnated Degussa P25 converted 0.3±0.03% of water vapor to hydrogen. Reactions that took place with only the quartz wool and no catalyst inside the plate reactor did not generate hydrogen.

Figure 6.1 compares the percentage conversions of water to hydrogen on a per-gram of ruthenium basis for Ru-doped titania nanotubes to Ru-impregnated Degussa P25 as a function of reactor temperature. Figure 6.2 shows the rates of hydrogen production from water as a function of reactor temperature for Ru-doped anatase nanotubes, Ru-doped amorphous nanotubes, and unaltered anatase nanotubes.

Ruthenium-doped amorphous titania nanotubes showed photocatalytic activity similar to that of un-doped anatase nanotubes and Ru-impregnated Degussa P25. However, the amorphous titania nanotubes showed increased photocatalytic activity in the methylene blue probe reactions discussed in Chapter 4. The process of reducing the ruthenium (III) chloride hydrate most likely also de-oxygenated the amorphous titania nanotubes and removed adsorbed hydroxyls to a greater extent, so the effect of pre-reaction surface hydroxyl groups was negated. In addition, all photocatalysts in the plate reactor were hydroxylated by the water vapor in the feed stream. As a result, the Ru-doped anatase titania nanotubes were more effective water splitting photocatalysts compared to Ru-doped amorphous titania nanotubes due to its increased crystallinity.

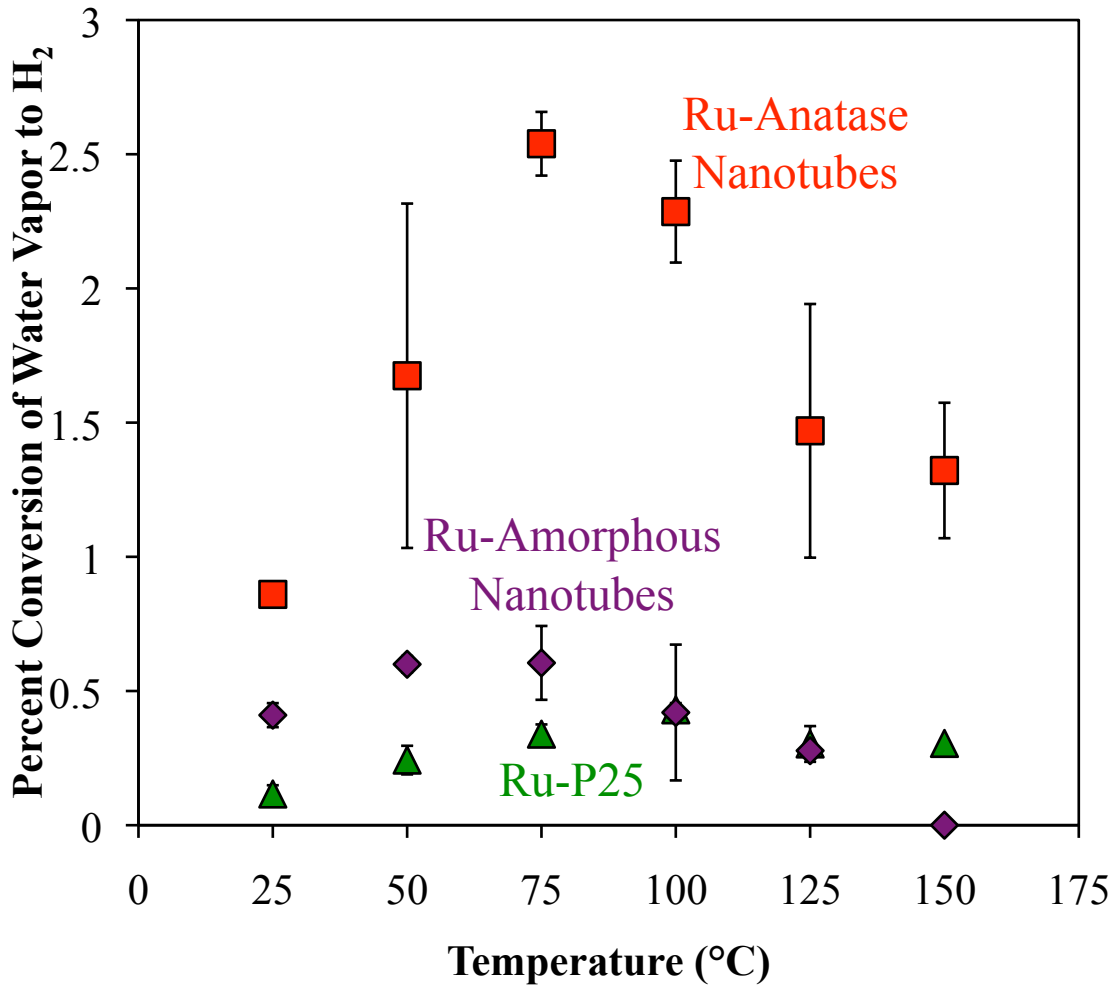

Figure 6.1: Percent conversion of water vapor to hydrogen by Ru-doped anatase titania nanotubes, Ru-doped amorphous nanotubes, and Ru-impregnated Degussa P25.

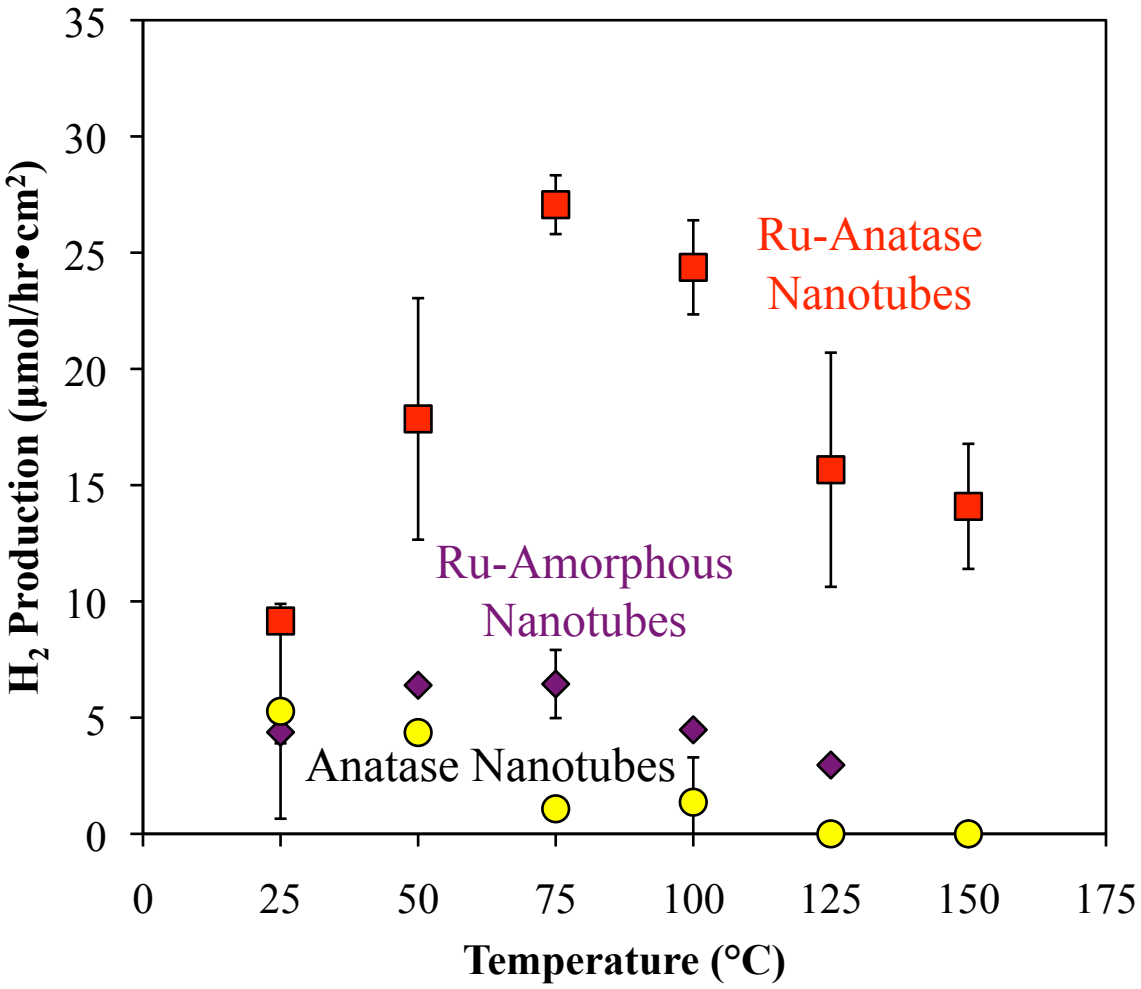

Figure 6.2: Rate of hydrogen generation from water vapor by Ru-doped anatase titania nanotubes, Ru-doped amorphous nanotubes, and undoped anatase titania nanotubes in µmoles per hour per area illuminated by UV light.

The limited photocatalytic activity of the anatase titania nanotubes compared to Ru-doped anatase titania nanotubes may be due to the altered band-gap caused by ruthenium doping. In addition, the differences in hydrogen production rates are most likely due to ruthenium's ability to localize protons for increased hydrogen formation. The limited ability of Ru-impregnated P25 is most likely due to large ruthenium particles on the surface of the P25 particles. These large ruthenium particles probably did not alter to the band gap and may have prevented UV light from reaching the surface of the

Degussa P25 powder resulting in little photocatalytic activity of the catalyst compared to Ru-doped materials. Oxygen also resulted from the water splitting reaction. Small amounts were measured by gas chromatography; however, the amount measured did not fulfill the material balance suggesting that the ruthenium-titania catalyst itself may have adsorbed some oxygen. Even though hydrogen and oxygen were formed from water in the presence of nitrogen and carbon dioxide, no methane was measured by the FID. However, due to the low water to hydrogen conversions, methane may have been formed in amounts outside the operating limits of the gas chromatograph.

6.2 Addition of Activated Carbon

Activated carbon has been considered as a possible support for photocatalytic materials due to its high surface area and wide range of porosities [1]. The use of activated carbon as a support for TiO_2 particles has been examined due to a resulting high adsorption of reactants and access to the TiO_2 particles. Several authors have studied the use of TiO_2 particles on activated carbon support for the photocatalytic degradation of phenol. The Velasco group suggests that the activated carbon enhances the photocatalytic activity of the TiO_2 particles due to greater adsorption of reactants [1-2]. The Velasco group also suggests that the activated carbon itself may be photocatalytically active for the degradation of phenol. Carbon nanotubes as a support for TiO_2 particles have also been investigated since it would provide similar benefits as activated carbon [1][3]. In addition, previous work has focused on carbon-doping to modify the band gap of TiO_2 for increased photocatalytic activity [1][4]. In the following studies, activated

carbon is not used as a support, but it is used as an oxygen absorbant to prevent the recombination of hydrogen and oxygen and to prevent subsequent combustion of methane.

Figure 6.3 is an AspenTech Aspen Plus® computer simulation showing the resulting increase in possible methane formation as a function of the percentage of oxygen gathered. The computer simulation modeled the methane production assuming a 50% conversion of water to hydrogen. The simulated gas feed stream of 10 sccm nitrogen, 40 sscm water, and 20 sccm carbon dioxide reacted at 75°C in a flow reactor. The Aspen simulation was performed using the Peng-Robinson property method and the RGibbs reactor model to minimize Gibbs free energy to predict reaction products. The simulation shows that the methane production increases as oxygen, which results from water splitting, is removed from the reactor system. If no oxygen is removed, methane will not be measured because the oxygen liberated from water will combust with methane to form carbon dioxide.

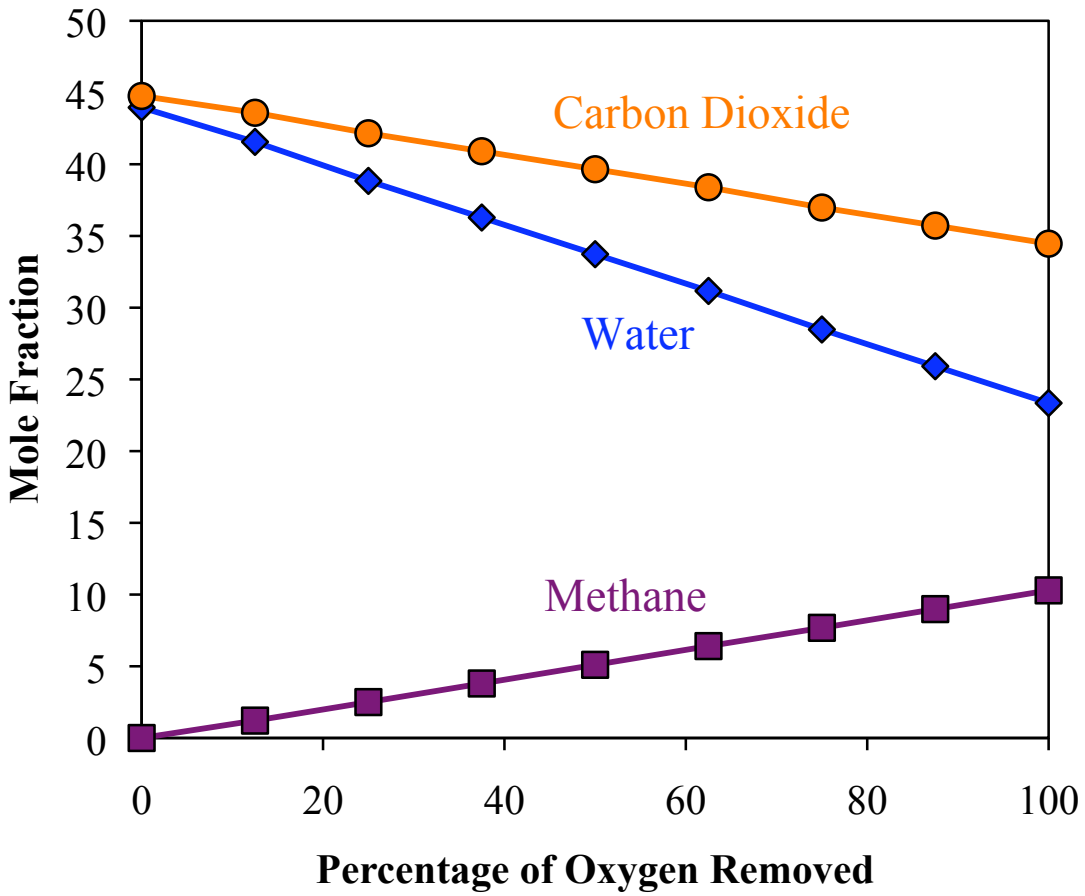

Figure 6.3: Aspen model prediction of methane generation by the simultaneous water splitting and Sabatier reaction as a function of oxygen adsorbed by activated carbon.

To study the effect of adding an "oxygen-getter" to the reaction, approximately 0.125-0.250 g activated carbon pellets (NORIT® RO 0.8, pellets) were physically placed on the surface of the catalyst. An individual activated carbon pellet was cylindrical in shape with a diameter of 0.8 mm and length of 3-5 mm. When using 250 mg of the activated carbon in the quartz plate reactor, the ratio of carbon to titania in the titania nanotubes was 42:1 by mass. When comparing the performance of titania nanotubes to titanium dioxide powder, the ratio of carbon to Degussa P25 was 5:8 by mass. The reactions took place at 25-150°C and products were measured by a Varian CP-3800 Gas

Chromatograph equipped with two thermal conductivity detectors and a flame ionization detector.

Addition of activated carbon to the flow reactor containing titania catalyst resulted in improved hydrogen generation from water splitting under UV light. The physical addition of 250 mg of activated carbon to Ru-doped anatase titania nanotubes resulted in a 44% conversion of water to hydrogen for approximately 13 hours in a flow system at 25°C under UV light (Figure 6.4). This represents record hydrogen generation from photocatalytic water splitting in a titania-based system. After approximately 13 hours, the Ru-doped anatase nanotube catalyst deactivated, which will be discussed in more detail. Dionigi and coworkers fabricated a microreactor and a GaN:ZnO powder loaded with $Rh_{2-y}Cr_yO3$ co-catalyst to convert 43% of water vapor to hydrogen and oxygen under high intensity simulated solar light [5]. This conversion is also remarkable, but a larger system would be more industrially feasible.

Figure 6.5 shows the trends in water vapor to hydrogen conversion for Ru-doped anatase nanotubes, Ru-doped amorphous titania nanotubes, and Degussa P25 between 25°C and 125°C. In the presence of activated carbon, Ru-doped amorphous titania nanotubes converted 13.5% of water vapor to hydrogen at 50°C. Also in the presence of activated carbon, Degussa P25 without ruthenium converted 5.7% of water vapor to hydrogen. Reactions that took place with only 250 mg of activated carbon on quartz wool and no catalyst inside the plate reactor did not generate hydrogen; therefore, the activated carbon was not photocatalytically active for the water splitting reaction.

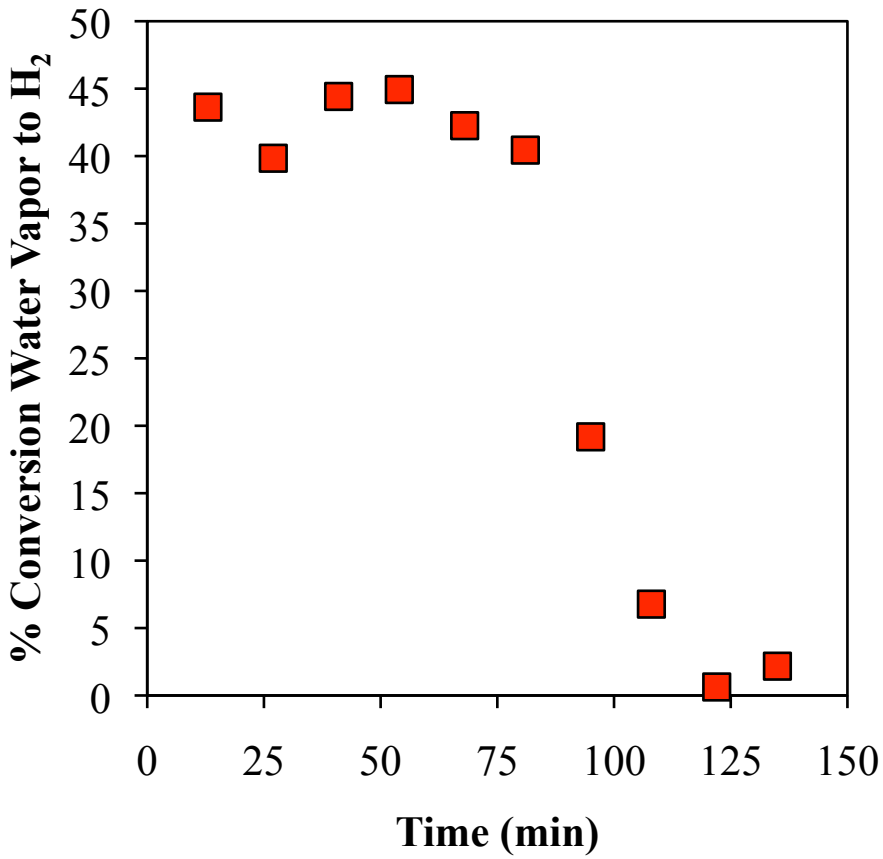

Figure 6.4: Percent conversion of water vapor to hydrogen as a function of time under UV light using Ru-doped anatase nanotubes with 250 mg of activated carbon.

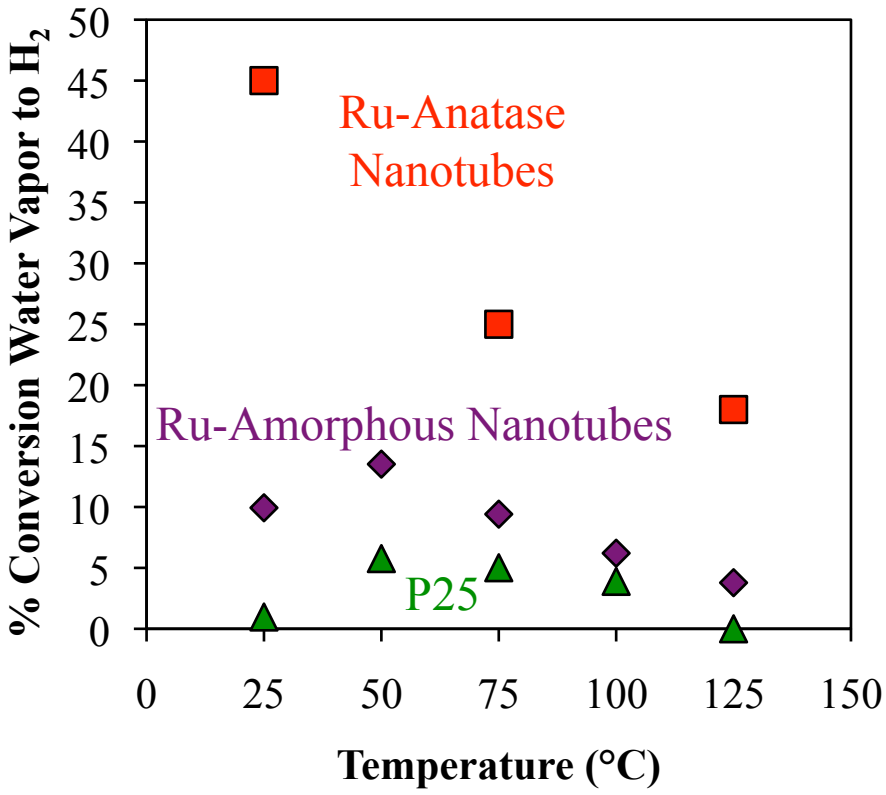

Figure 6.5: Steady state percent conversion of water vapor to hydrogen as a function of temperature under UV light for Ru-doped anatase titania nanotubes, Ru-doped amorphouse titania nanotubes, and un-doped Degussa P25, each with 250 mg activated carbon.

Figure 6.6 is a graph of turnover frequency as a function of reaction temperature for the experiments described by Figure 6.5. The turnover frequency assumes that the active sites for water splitting are located on the surface of the titania nanotubes since the ruthenium is not in large particle form on the surface of the array.

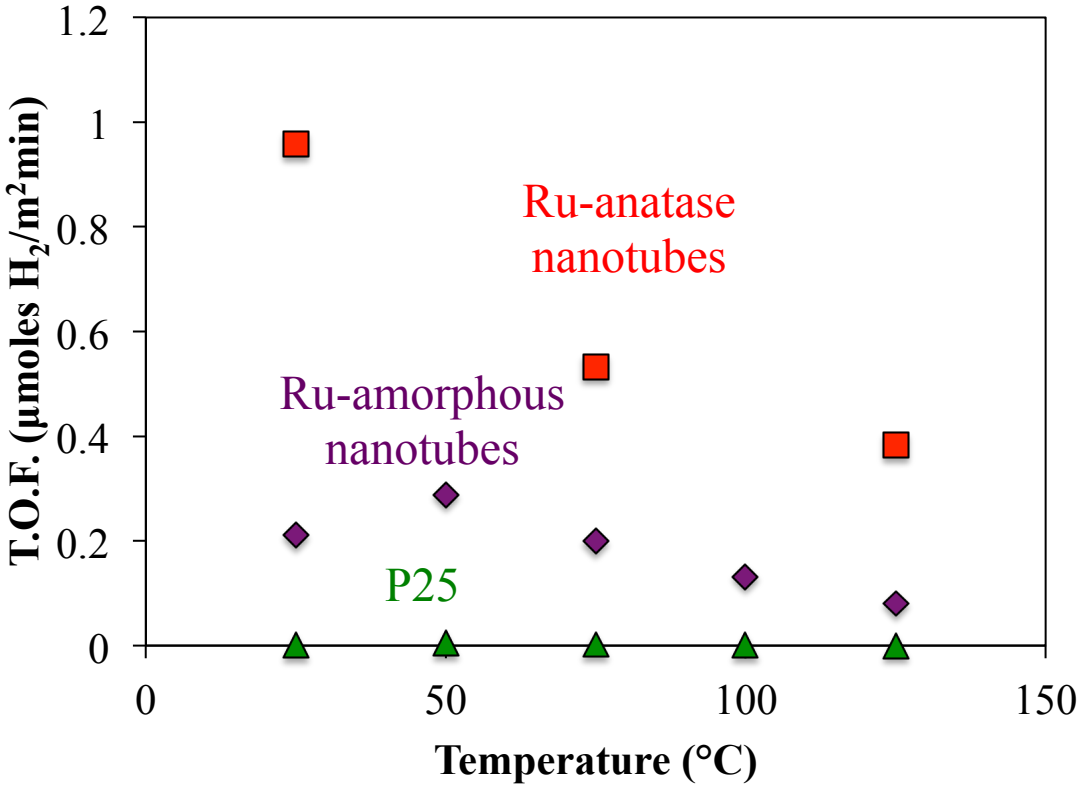

Figure 6.6: T.O.F. for hydrogen generation over Ru-doped anatase titania nanotubes, Ru-doped amorphous titania nanotubes, and Degussa P25 (undoped) as a function of temperature.

To prove that the water splitting reaction was photocatalytic, instead of thermal or otherwise, the UV light was turned on and off while measuring hydrogen production over Ru-doped anatase nanotubes with activated carbon and Degussa P25 with activated carbon. Figure 6.7 shows the cessation of hydrogen production over Ru-doped anatase nanotubes with activated carbon at 125°C as a result of turning off the UV lamp. When the UV light is turned off, the hydrogen production diminishes slowly. Titania nanotubes store hydrogen effectively and have been considered for hydrogen sensing. The diminishing hydrogen production is most likely due to the release of stored hydrogen from the nanotubes. Figure 6.8 shows hydrogen production with UV light and no

hydrogen production in the absence of UV light using Degussa P25 with activated carbon at 50°C.

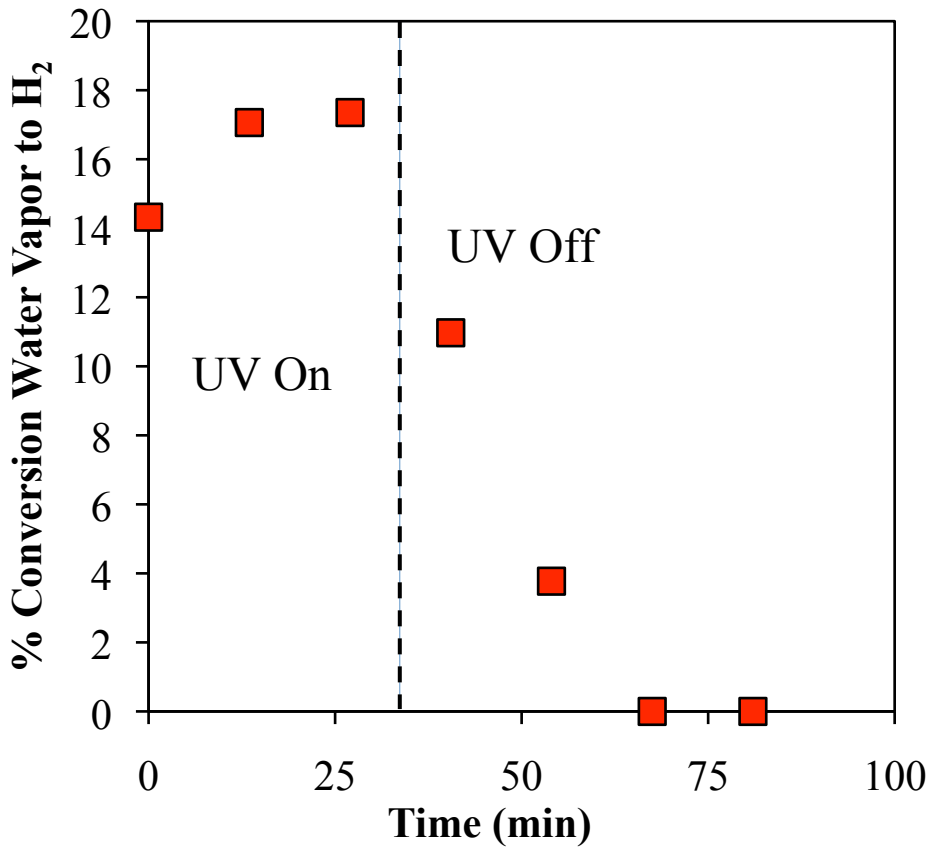

Figure 6.7: Percent conversion of water vapor to hydrogen as a function of UV light illumination for Ru-doped anatase titania nanotubes with 250 mg activated carbon at 125°C.

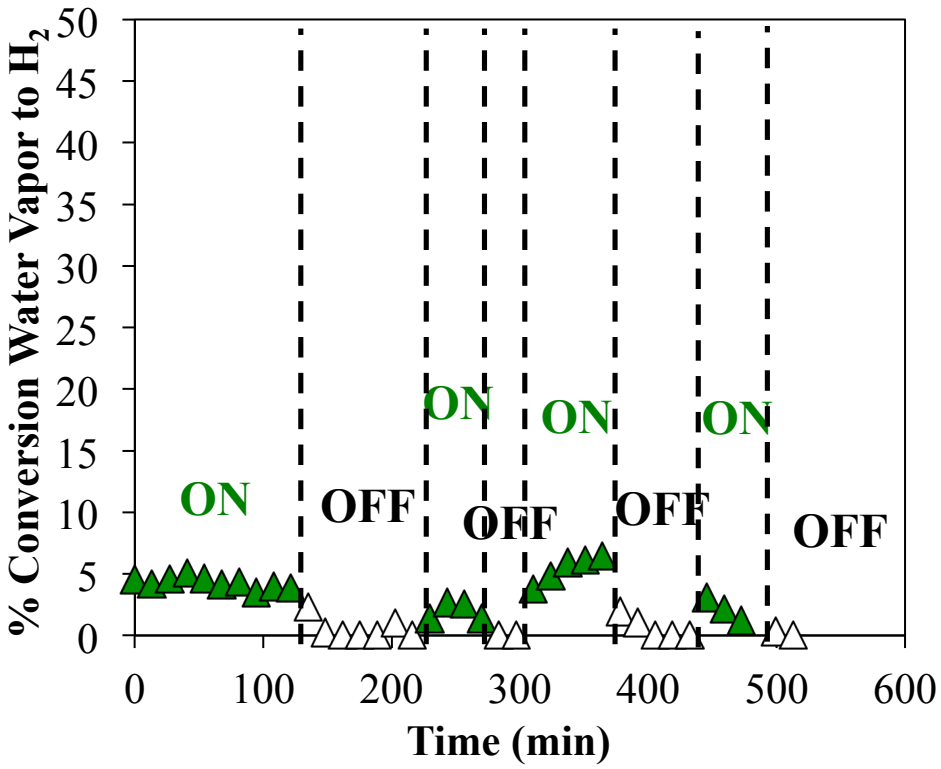

Figure 6.8: Percent conversion of water vapor to hydrogen as a function of UV light illumination on Degussa P25 with 250 mg activated carbon.

6.3 Deactivation Mechanism

The deactivation of the water splitting reaction could have been caused by the adsorption capacity of the added activated carbon resulting in the cessation of oxygen gathering. The deactivation could have also been caused by the oxidation of ruthenium in the titania nanotubes, which would alter the photocatalyst's ability to perform the water splitting reaction itself. To test these hypotheses, a water splitting reaction was carried out using Ru-doped anatase nanotubes with added activated carbon under UV light at 25°C. After deactivation, the used activated carbon was replaced with fresh

activated carbon. Figure 6.9 indicates that the water splitting reaction did not resume, which suggests that the activated carbon did not cause the deactivation.

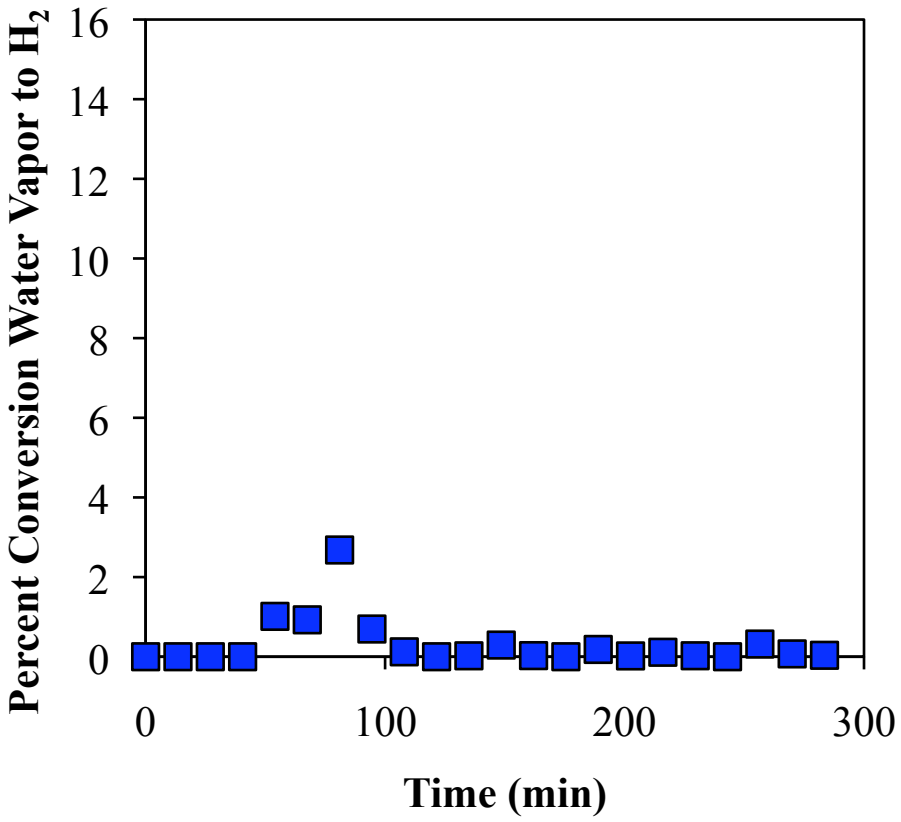

Figure 6.9: Percent conversion of water vapor to hydrogen as a function of time under UV light illumination for used Ru-doped titania nanotubes and fresh 250 mg activated carbon.

Figure 6.9 shows a slight increase in hydrogen production after 81 minutes followed by deactivation. This temporary increase is most likely due to *in situ* reduction of the Ru-doped titania nanotube catalyst due to the 590 torr nitrogen in the feed stream. Deactivation occurred once the reduced sites were quickly reoxidized.

To determine if oxidation of the Ru-doped titania nanotubes caused the water splitting reaction deactivation, a water splitting reaction was again carried out using Ru-

doped anatase nanotubes with added activated carbon under UV light at 25°C. The water splitting reaction converted 35% of the water vapor to hydrogen on a per mole basis.

After deactivation, the used Ru-doped anatase nanotubes mixed with the used activated carbon were removed from the plate reactor. The Ru-doped nanotubes were then reduced in 5% hydrogen in nitrogen for 2.5 hours at 250°C. The Ru-doped titania nanotubes were reloaded into the plate reactor with the used activated carbon. Figure 6.10 indicates that the water splitting reaction resumed at a 35% conversion of water vapor to hydrogen until it deactivated again after six hours.

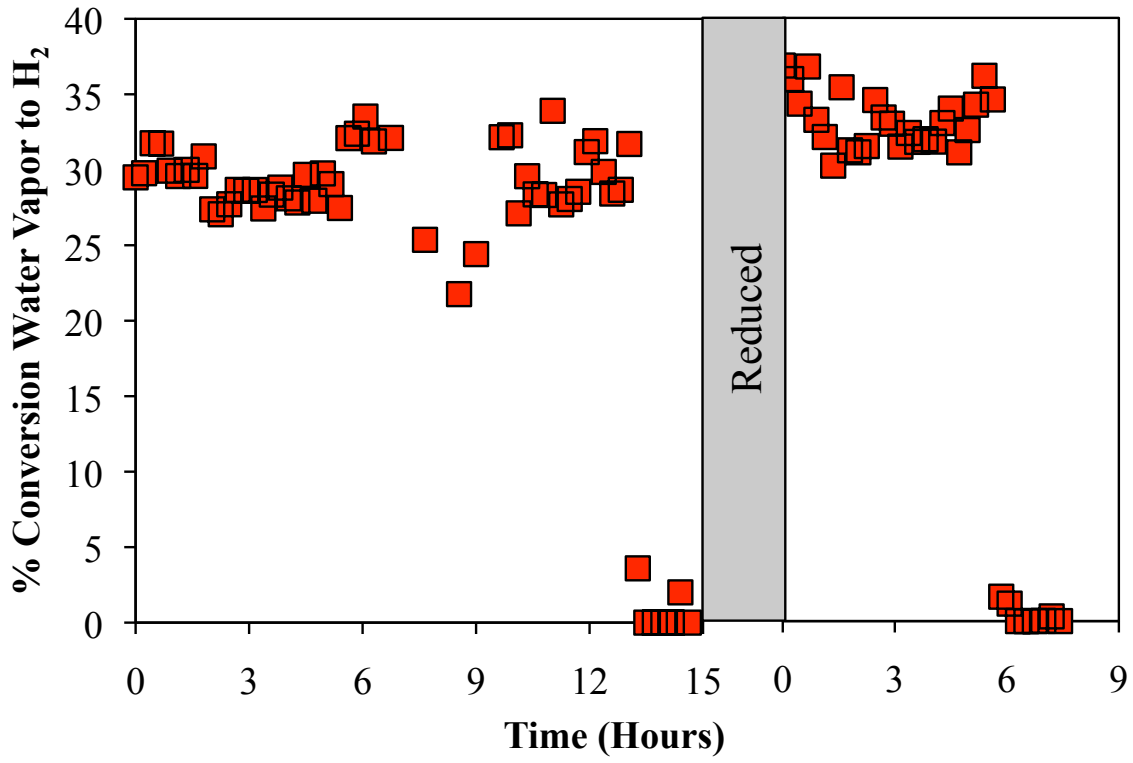

Figure 6.10: Percent conversion of water vapor to hydrogen on Ru-doped anatase titania nanotubes with activated carbon as a function of time showing the deactivation and the reactivation by reduction in 5% H_2 at 250°C.

An XPS study of the Ru-doped anatase nanotubes also showed that the deactivation was caused by the oxidation of ruthenium. A Ru-doped anatase nanotube

sample reduced in 5% hydrogen in nitrogen for 2.5 hours at 250°C showed a ruthenium binding energy of 280.1 eV, characteristic of metallic ruthenium. A Ru-doped anatase sample that was used in a water splitting reaction that had deactivated showed a Ru binding energy of 281.1 eV, which indicated that the catalyst surface was oxidized and suggested the presence of $RuOCO_3$ or $RuO_2 \bullet H_2O$ surface species. Finally, a Ru-doped anatase nanotube sample was reduced in 5% hydrogen in nitrogen for 2.5 hours was then oxidized in air for 12 hours at 250°C. This sample showed a Ru binding energy of 281.8 eV, which indicated that the ruthenium was also oxidized. Table 6.1 summarizes the findings from XPS and Figure 6.11 shows the XPS spectra. This study shows that the ruthenium and the overall surface of the titania nanotubes are oxidized as a result of the water splitting reaction. This result helps to explain the fate of the oxygen resulting from water splitting as well as the cause for deactivation of the Ru-doped titania nanotube photocatalyst.

Table 6.1 XPS results comparing a fresh, used, and purposely oxided Ru-doped titania nanotube photocatalyst.

Sample	Ru 3d (eV)	O 1s (eV)	Species
Reduced	280.1	530	Ru(0)
Post-Reaction	281.1	530.4	$RuOCO_3/RuO_2 \bullet XH_2O$
Oxidized	281.8	530.3	$RuO_2 \bullet XH_2O$

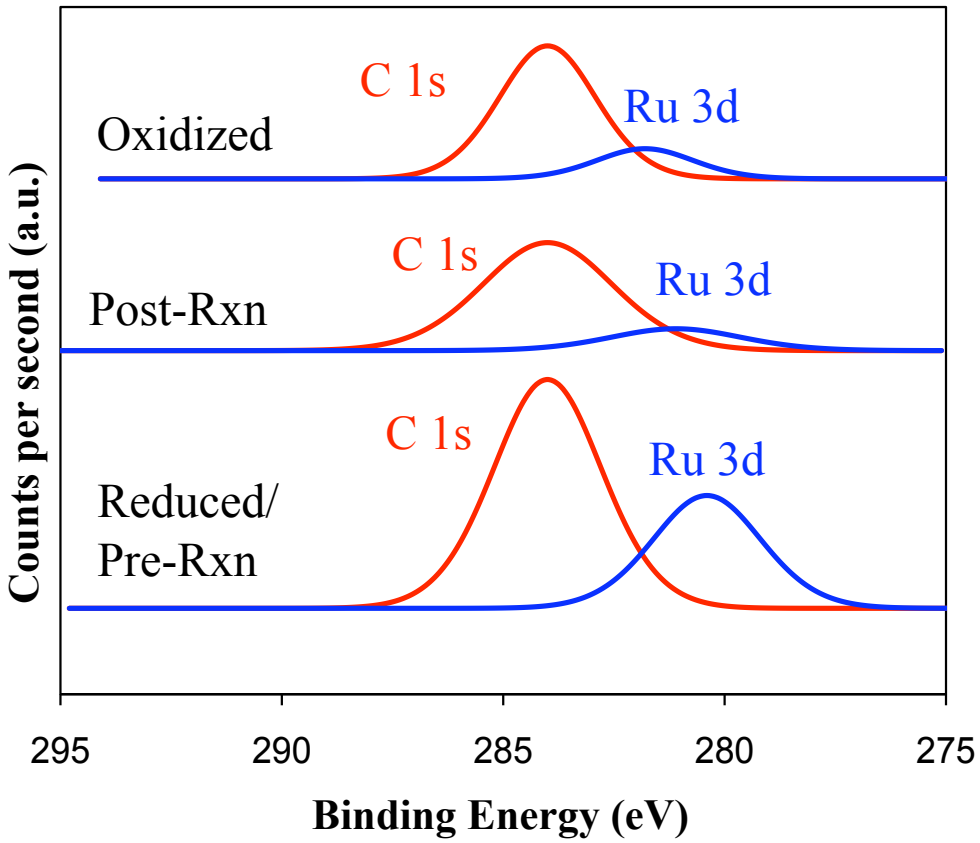

Figure 6.11: XPS spectra of the fresh, post-reaction, and purposely oxidized Ru-doped titania nanotube photocatalyst.

6.4 Limitations of Photocatalytic Water Splitting in the Presence of Activated Carbon

Since the water splitting reaction under UV light using Ru-doped titania nanotubes in the presence of activated carbon has not yet been optimized, reproducibility issues still remain. The performance of the Ru-doped titania nanotubes depend on the degree to which they are reduced prior to the water splitting reaction. In addition, the location of the activated carbon relative to the nanotube arrays strongly impact the ability of the activated carbon to gather oxygen to prevent the oxygen-hydrogen recombination. The mean-free path between the liberated oxygen and hydrogen is short; therefore, the

activated carbon must also be close to the active sites in order to intercept the oxygen before recombination. In addition, the activated carbon may also act as an absorbant of water vapor and carbon dioxide, so close proximity to the titania nanotubes would be required to allow for subsequent mass transfer to the photocatalytically active titania sites.

To determine the effect of the activated carbon's proximity to the photocatalyst, 250 mg of activated carbon was placed next to the Ru-doped titania nanotubes, but they were not in physical contact. As a result, the conversion of water vapor to hydrogen was less than 2.5%, which was the same as if there were no activated carbon in the reactor at all. During the water splitting reactions that showed 35-44% maximum conversions, the activated carbon was placed on the surface of the Ru-doped titania nanotube array. The drawback to placing carbon on the titania nanotube array surface, however, is that too much activated carbon can block UV light from reaching the titania surface, which would reduce the ability of the titania to split water. As a result, the use of activated carbon in the water splitting reaction should be optimized. Figure 6.12 is a schematic of the placement of the activated carbon relative to the photocatalyst.

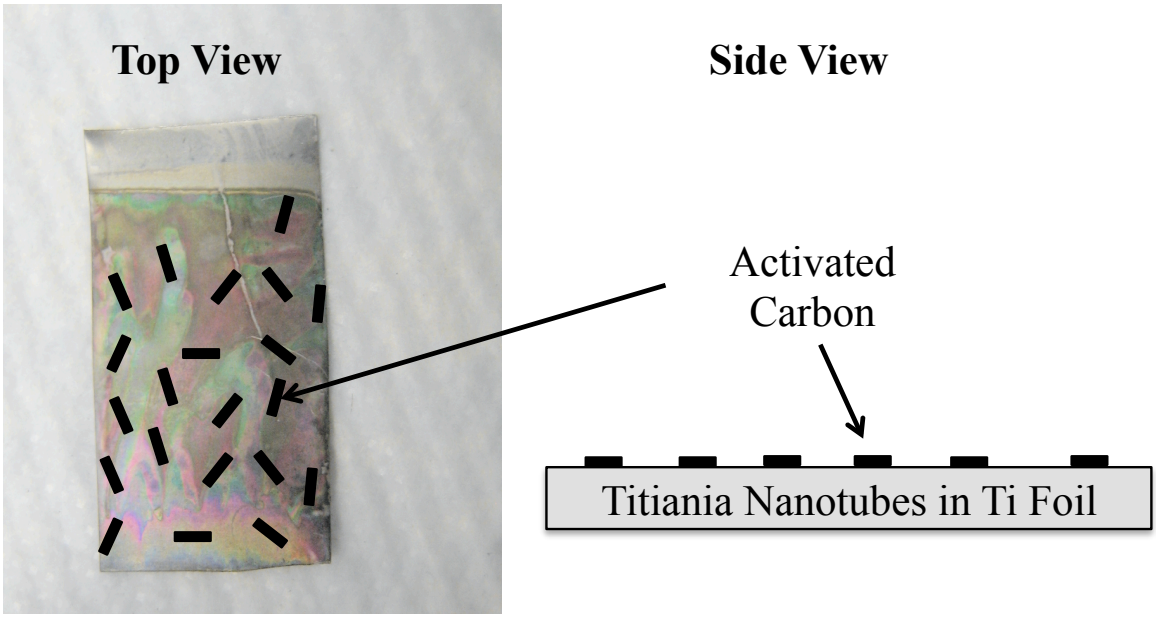

Figure 6.12: Top-view and side view schematics of the placement of activated on the top of a titania nanotube array on a Ti foil substrate.

Figure 6.13 shows the result of varying the amount of activated carbon inside the plate reactor. The water splitting reaction took place over Ru-doped anatase nanotubes in the presence of 125 mg activated carbon and 250 mg activated carbon. The conversion of water vapor to hydrogen in this particular experiment was most likely due to the degree to which the ruthenium was reduced and the lack of system optimization. However, this study does indicate that the water vapor to hydrogen conversion was a function of the amount of activated carbon in the system and scaled with the number of sites available for oxygen adsorption.

During the water splitting reactions, methane was not measured by the FID. This may again be due to the sub-stoichiometric amount of hydrogen available to react with carbon dioxide; thus, the amount of methane formed would be below the FID's detection limits. Secondly, the methane may also have been adsorbed too strongly by the Ru-doped titania nanotubes or the activated carbon during the water splitting reaction.

Thirdly, partial oxidation of methane may have also occurred causing the increased amount of hydrogen measured and the production of some carbon monoxide. Carbon monoxide was not measured by the TCD, however.

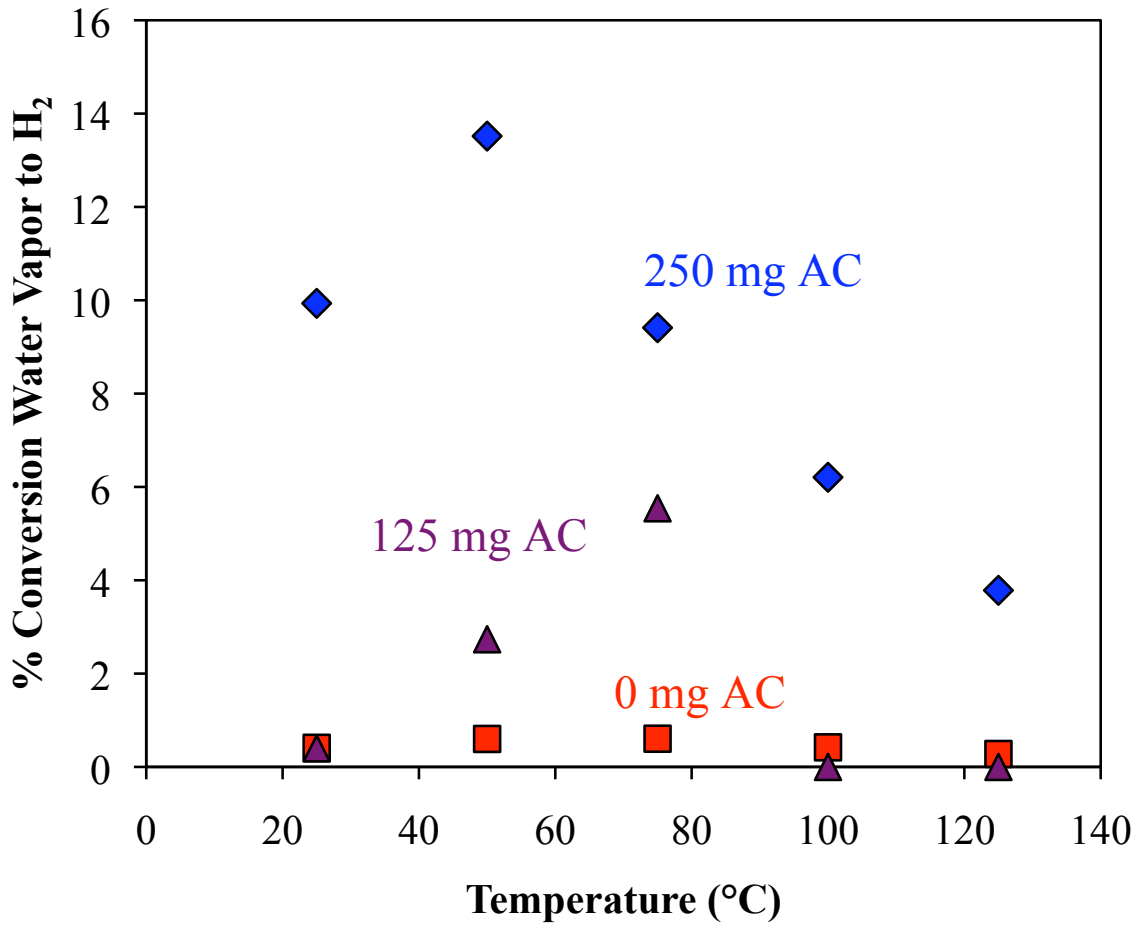

Figure 6.13: Steady state percent conversion of water vapor to hydrogen versus temperature as a function of varying activated carbon amounts.

In an attempt to increase the amount of hydrogen produced so that methane may be measured, a syringe pump and heated tubing was used to form a super-saturated water vapor stream. The resulting feed stream to the quartz plate reactor was composed of 365 torr water vapor, 80 torr carbon dioxide, and 315 torr nitrogen and experiments were carried out at 110°C to prevent condensation. Figure 6.14 shows the low conversion of

water vapor to hydrogen using Degussa P25 and added activated carbon as well as the lack of hydrogen generation using Degussa P25 in the absence of activated carbon. The most likely cause for the significantly reduced water vapor to hydrogen conversion was an excess of physisorbed water on the surface of the Ru-doped titania nanotubes, which hindered the water splitting reaction.

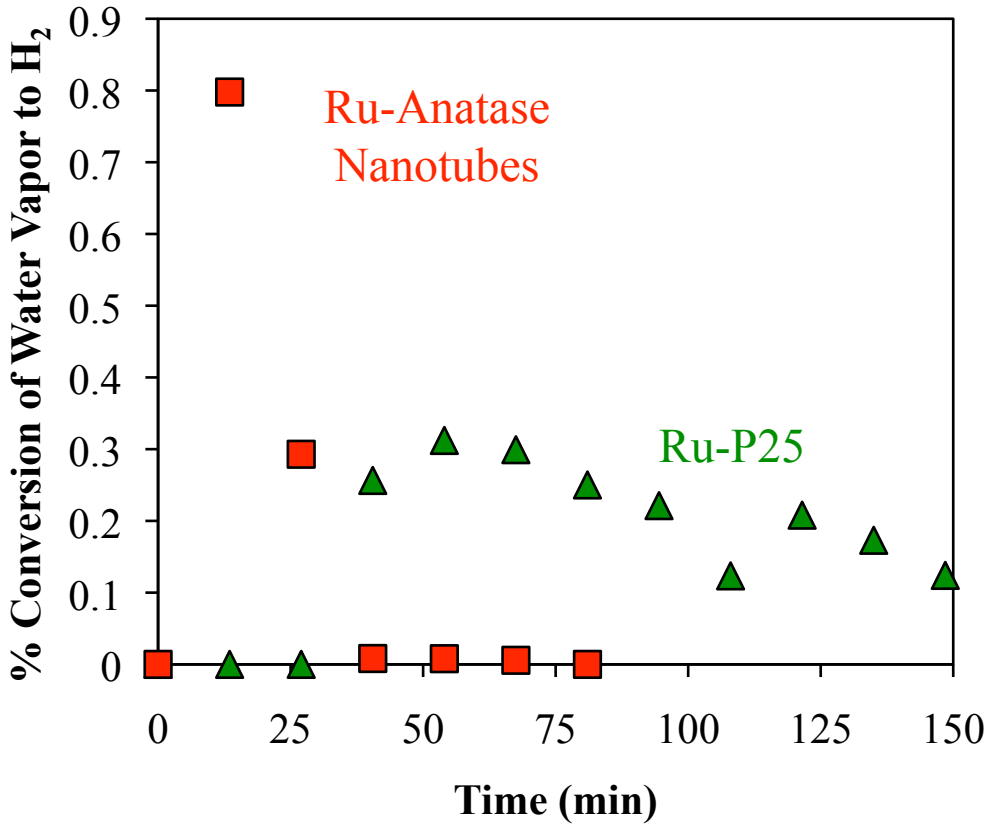

Figure 6.14: Percent conversion of water vapor to hydrogen as a function of time for Ru-doped anatase titania nanotubes and Ru-impregnated Degussa P25 using an increased water vapor input stream.

6.5 Conclusions

Ruthenium-doped titania nanotubes were found to be active for photocatalytic water splitting. Ruthenium-doped anatase titania nanotubes were more active compared to Ru-doped amorphous titania nanotubes, undoped anatase titania nanotubes, Ru-impregnated Degussa P25, and undoped Degussa P25. Addition of activated carbon increased the hydrogen production from photocatalytic water splitting by an order of magnitude by adding 250 mg to the surface of Ru-doped anatase titania nanotube arrays. The deactivation of the photocatalytic water splitting reaction was caused by the oxidation of the metallic ruthenium. The process requires further optimization to maximize hydrogen production and to produce methane in measurable quantities.

References

[1] Rowan Leary, Aidan Westwood, Carbonaceous nanomaterials for the enhancement of TiO_2 photocatalysis, *Carbon* 49 (2011) 741-742.

[2] Velasco LF, Parra JB, Ania CO. Role of activated carbon features on the photocatalytic degradation of phenol. *Applied Surface Science* 256 (2010) 5254–5258.

[3] S. Iijima, Helical microtubules of graphitic carbon, *Nature* 354 (1991) 56–58.

[4] S.U.M. Khan, M. Al-Shahry, W.B. Ingler, Jr., Efficient photochemical water splitting by a chemically modified n-TiO_2. *Science* 297 (2002) 2243–2245.

[5] Fabio Dionigi, Peter C. K. Vesborg, Thomas Pedersen, Ole Hansen, Søren Dahl, Anke Xiong, Kazuhiko Maeda, Kazunari Domen, and Ib Chorkendorff, Gas phase photocatalytic water splitting with $Rh_{2-y}Cr_yO_3$/GaN:ZnO in μ-reactors, *Energy and Environmental Science* (2011).

Chapter 7

Conclusions and Recommendations for Future Work

7.1 Conclusions

The properties of titania nanotubes as a function of synthesis conditions and the possibility of incorporating Ru-doped titania nanotubes into simultaneous water splitting and carbon dioxide methanation processes were studied in this work. The results presented in Chapter 4 show that the amount of fluoride in the synthesis electrolyte not only affects the dimensions of titania nanotubes, but the fluoride amount may also determine the ratio of oxygen to titanium in the titania nanotube prior to annealing. Amorphous titania nanotubes with a high oxygen to titanium ratio were found to be photocatalytically active in methylene blue decomposition probe reactions and outperformed the standard Degussa P25. The high oxygen to titanium ratio may be due to an increased number of adsorbed hydroxyl groups, which suggested that these nanotubes may be active for photocatalytic water splitting.

The titania nanotubes also exhibited changes in conductivity as a function of electrolyte composition. This finding further supported the hypothesis that synthesis conditions affect the oxygen to titanium ratio and suggested the possibility of titania nanotube arrays with tunable conductivities. Titania nanotubes with low oxygen to titanium ratios and higher conductivities were synthesized by electrolytes containing high

amounts of sodium fluoride. Based on recent terahertz spectroscopy studies, the observed low oxygen to titanium ratios and higher conductivities in Chapter 4 may be due to excess interstitial titanium and substitutional fluoride.

Finally, nitrogen adsorption-desorption experiments measured a high surface area for titania nanotubes and after heating to 850°C, rutile and intact titania nanotubes were observed. These measurements showed that titania nanotubes can be used as a catalyst support due to their high surface area for adsorption of reactants and can withstand high reaction temperatures.

The results presented in Chapter 5 indicated that titania nanotubes can be used as a support for ruthenium, which resulted in an effective Sabatier catalyst. The Ru-doped titania nanotubes did not produce as much methane as 0.5 wt.% ruthenium on alumina pellets between 200-600°C, except at 450°C. Above a reaction temperature of 450°C, carbon deposition and ruthenium sintering most likely occurred. Diffuse Reflectance Infrared Fourier Transform Spectrometry experiments revealed that the simultaneous water splitting and carbon dioxide methanation reaction occurred using Ru-doped anatase titania nanotubes under UV light illumination above 50°C. The mechanisms of the simultaneous reaction and the Sabatier reaction were discussed in Chapter 5.

The results presented in Chapter 6 showed that Ru-doped anatase titania nanotubes were the most effect photocatalyst for the water splitting reaction in a two-dimensional quartz plate flow reactor under UV light illumination with a water vapor, carbon dioxide, and nitrogen feed stream. To reduce the recombination of hydrogen and oxygen, activated carbon was physically placed on the top of the titania nanotube array to act as an oxygen adsorbant. As a result, 44% of the water vapor was converted to

hydrogen using the Ru-doped anatase titania nanotube photocatalyst. This was a record conversion of water vapor to hydrogen in a non-microreactor, titania-based system.

The limitations of the activated carbon/photocatalyst system were also investigated. Experiments revealed the oxidation of ruthenium as a cause for the deactivation of the water splitting reaction under UV light. In addition, the lack of optimization of the system was demonstrated by experiments that showed a correlation between hydrogen generation and proximity of activated carbon to the Ru-doped titania nanotube photocatalyst.

Overall, the work presented in this thesis showed that simultaneous photocatalytic water splitting and the Sabatier reaction can occur over a Ru-doped titania nanotube catalyst with a high oxygen to titanium ratio. The recombination of oxygen and hydrogen as well as the combustion of methane can be reduced by adding activated carbon to the flow reactor. Record hydrogen generation from the photocatalytic water splitting reaction occurred after adding activated carbon as an adsorbant. This work demonstrated that hydrogen can be generated from a non-fossil fuel source for the subsequent reduction of carbon dioxide.

7.2 Recommendations for Future Work

Significant research is required before the Ru-doped titania nanotube/activated carbon system is industrially feasible. First, optimization of the ruthenium weight-loading in the titania nanotube arrays should take place in order to improve hydrogen and methane generation and to adjust the band gap of the titania nanotubes. The experiments

done in this work used UV light as an energy source, but the process would be much more energetically and economically viable if the titania nanotubes were sensitive to visible light, which represents more of the solar spectrum. Using sunlight, instead of a UV lamp, would reduce the need for extra electricity generation, which would then reduce the amount of carbon dioxide emitted from coal-based electrical plants. The hydrogen generation as a function of light intensity should also be studied and optimized.

The design of the two-dimensional quartz plate reactor must also be improved and optimized. For example, placing the titania nanotubes at an angle in the reactor to create a zig-zag pattern may increase the path length of the reacting gases to allow for greater adsorption onto the photocatalyst and higher hydrogen and methane production. Also, the shape of the quartz-plate reactor is currently rectangular, which does not allow for the maximum gas flow over the catalyst. In addition, the dead space between the surface of the titania nanotube catalyst and the quartz plate should be reduced to minimize the amount of reacting gases that flow through the reactor without coming into contact with the active sites of the photocatalyst.

Next, optimization of the placement of activated carbon on the top of the Ru-doped titania nanotube array should be done. The activated carbon must be in physical contact with the titania nanotube array, but it can also block UV light from reaching the surface of the titania. This optimization of the activated carbon placement should allow for the maximum amount of oxygen absorbed from the system while allowing for maximum UV illumination of the titania nanotube array.

Another area of research should be the incorporation of activated carbon into the titania nanotube array. The use of activated carbon-doped or activated carbon-

impregnated titania nanotubes would allow the carbon to be closer to the oxygen evolved from the water splitting process. A high loading of activated carbon into the titania nanotube array would allow for maximal oxygen absorption, but special consideration should be made to changes in the titania nanotube band gap that the addition of activated carbon into the nanotube framework may cause.

To make this work more industrially feasible, studies should be done to determine if water splitting and carbon dioxide methanation should be conducted in separate reactors. A reaction scheme could be devised to allow for water splitting and oxygen removal in one reactor at lower temperature to generate hydrogen for carbon dioxide methanation in a close-coupled reactor at higher temperature over a conventional Sabatier catalyst. This method may increase methane production since the water splitting and Sabatier reactions occur in different temperature regimes. Secondly, photocatalytic water splitting for ammonia synthesis should be examined. Ammonia is a chemical that is also in demand for use in fertilizers and as a potential alternative fuel for internal combustion engines. Activated carbon addition for the removal of oxygen could increase ammonia production without using a fossil fuel-based hydrogen source.

APPENDICES

APPENDIX A

Titania Nanotube Synthesis Standard Operating Procedure

HAZARDS

- Sodium fluoride (99.9%)
- Chloroplatinic acid solution (8 wt. % in H2O)

ENGINEERING CONTROLS

- Chemical fume hood
- Chemical spill kit

PROTECTIVE EQUIPMENT

- Safety glasses
- Latex gloves
- Respirator

WASTE DISPOSAL

- Dispose of materials in appropriate waste containers.

ACCIDENTAL SPILL

- In the case of accidental spill of aforementioned hazardous chemicals, use chemical spill kit to clean spill. Dispose of cleaning materials in compliance with appropriate hazardous waste disposal procedures.

PROCEDURE

Electrolyte Synthesis Procedure

1. Measure 0-1 gram of sodium fluoride (depending on the desired concentration). Wear a respirator
2. Mix sodium fluoride with 50 mL of deionized water in a polypropylene bottle. Stir until sodium fluoride dissolves completely.
3. Add 40 mL of glycerol to the solution. Stir until the glycerol and water are well-mixed.
4. Pour ~40 mL of solution into a polypropylene cup.

Anodization Procedure:

1. Attach the titanium substrate to one of the alligator clips on the plastic alligator clip holder.
2. Attach the platinum substrate to one of the alligator clips on the plastic alligator clip holder.
3. Turn on the DC power supply, computer, and data acquisition unit. Turn on the DC power by hitting the "Output On/Off" button. Set the DC power supply to the

desired voltage (0-30V). Turn the DC power off by hitting the "Output On/Off" button again.

4. Attach the alligator clip holder to the DC power supply.
5. Place the alligator clip holder over the polypropylene cup so that the titanium and platinum substrates are immersed in the electrolyte. Place the apparatus inside the chemical fume hood.
6. Open Agilent BenchLink Data Logger software from the computer desktop. Select "Open an existing setup" and then select "Liz May 2007." Once the program opens, select from the file menu Instrument→Download Setup. When ready, press the start button.
7. Press the "Output On/Off" button on the DC power supply to begin anodization. Allow about 5-30 minutes for the anodization to complete.
8. When finished, press the "Output On/Off" button again, turn off the DC power supply, and turn off data acquisition unit. Save data on the computer and shut the computer down.
9. Remove the alligator clip holder from the polypropylene cup. Remove the titanium and platinum substrates from the holder and rinse both with deionized water.
10. Dispose of the electrolyte in an appropriate waste container.

APPENDIX B

Beer-Lambert Calibration for UV-VIS Measurements of Methylene Blue Composition

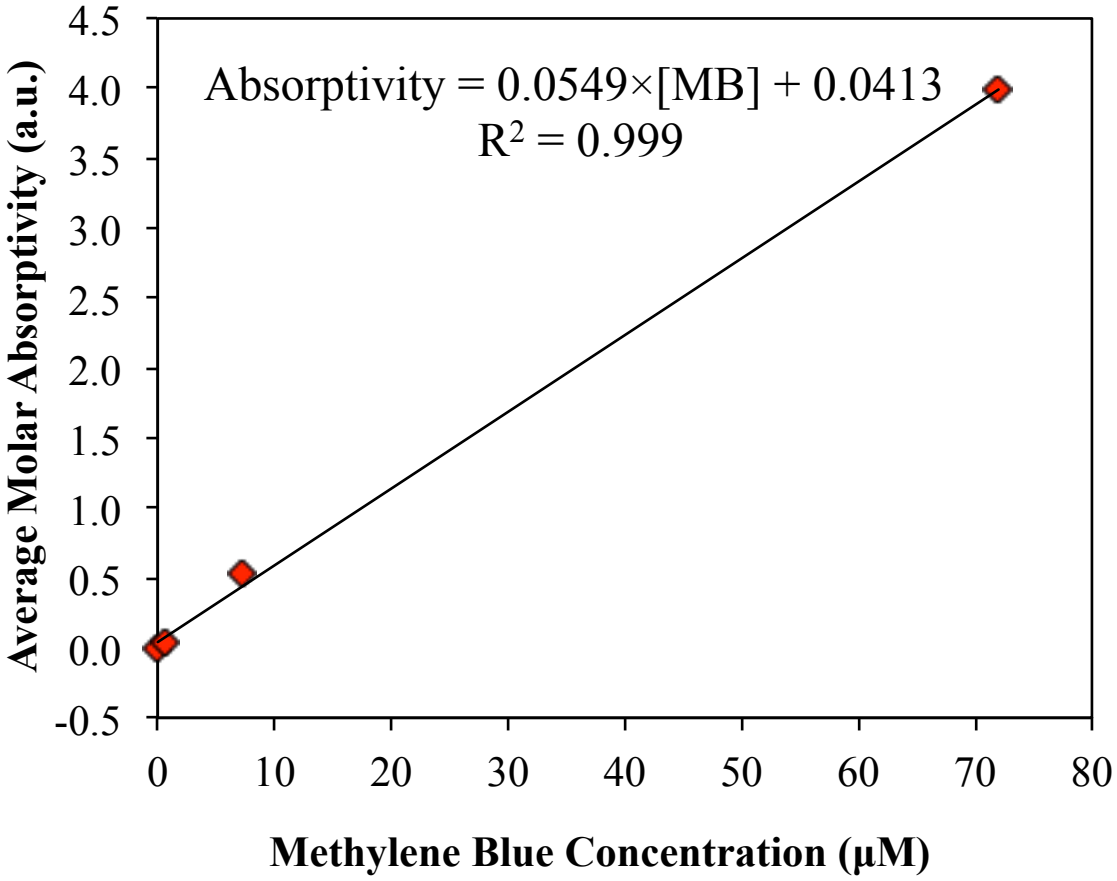

*Calibration taken at 664 nm by UV-Vis Spectrometer

APPENDIX C

Four Point Sensing Design

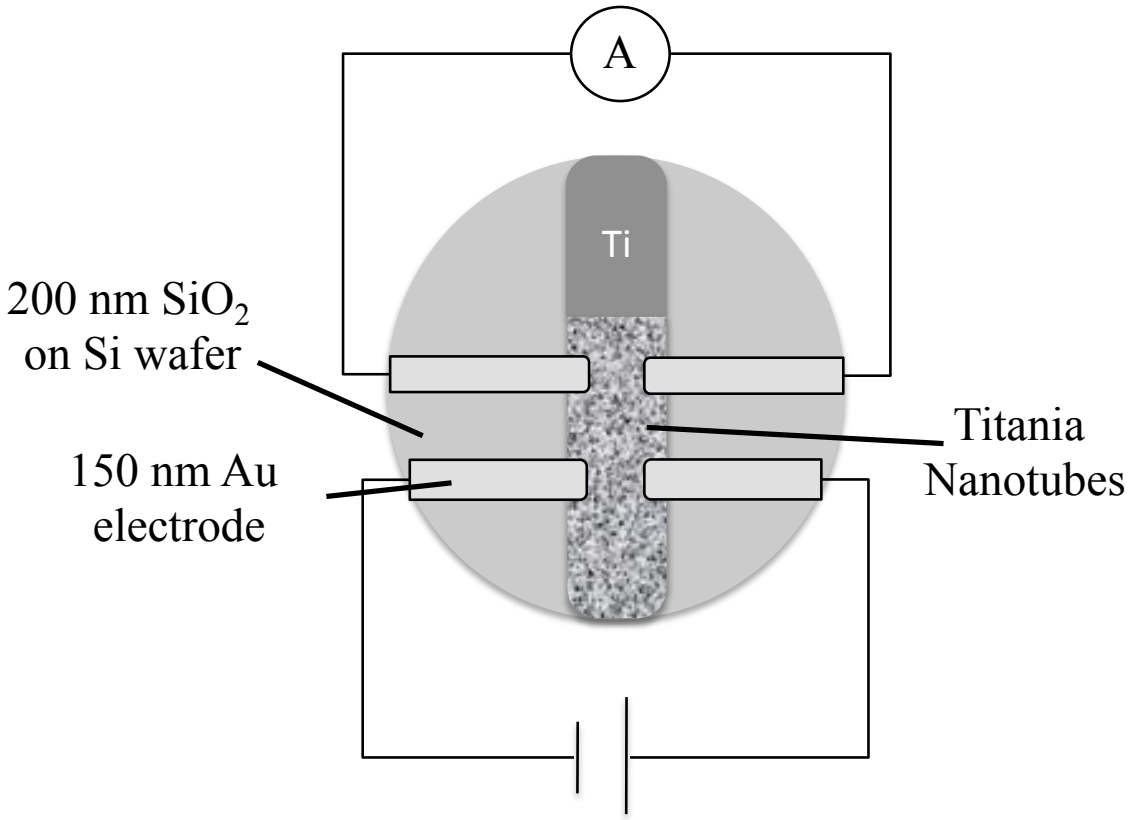

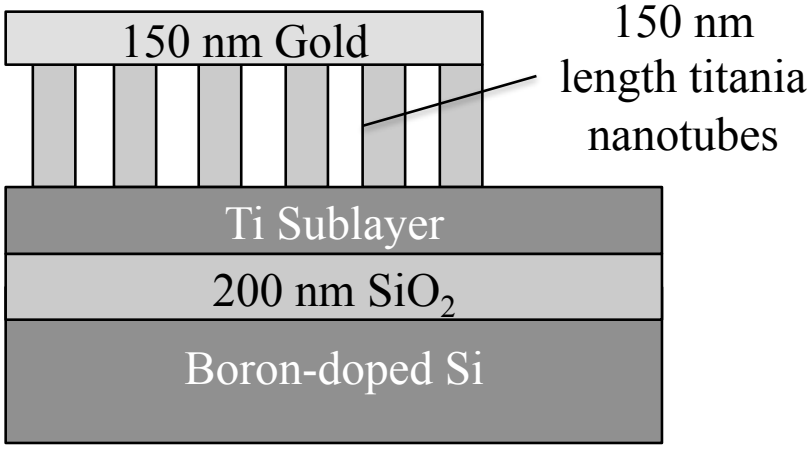

APPENDIX D

2-D Quartz Plate Reactor Design

Top View

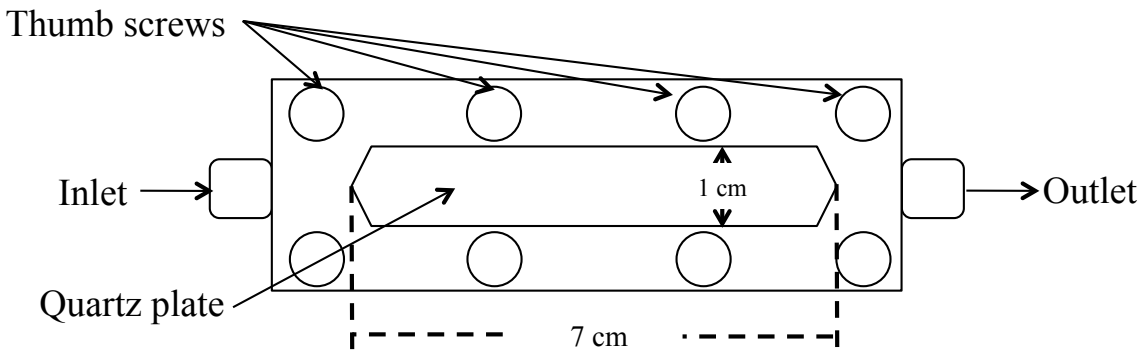

Side View

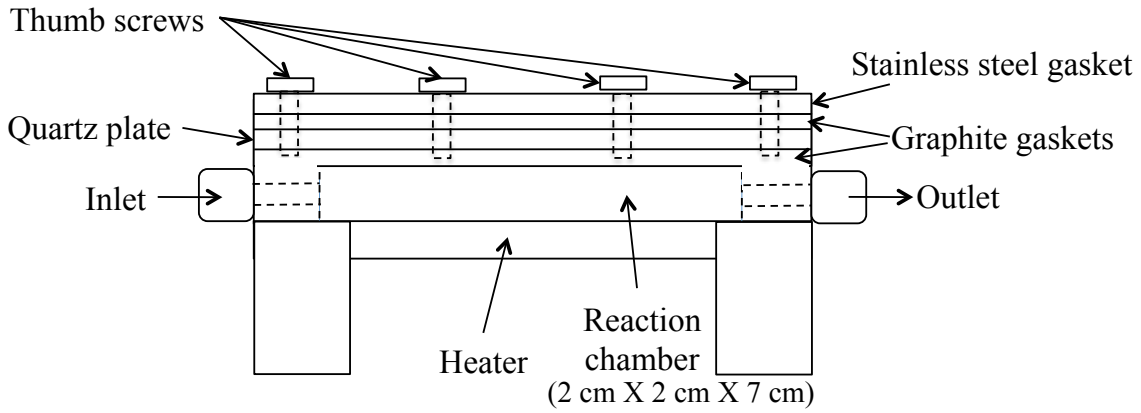

APPENDIX E

Procedure for Operating UV Plate Reactor System

HAZARDS

- Hot surfaces
- Compressed gases – carbon dioxide, nitrogen, hydrogen, air, argon, and helium
- Vessels and piping pressurized to 150 pounds per square inch
- Exposure to electric current
- UV Light

ENGINEERING CONTROLS

- Fume hood
- Flammable gas detectors

PROTECTIVE EQUIPMENT

- UV-Protective Safety glasses
- Heat resistant gloves to handle furnaces or backpressure regulator while system is in operation
- Latex gloves to handle catalyst
- Lab Coat

WASTE DISPOSAL

- Waste water

ACCIDENTAL SPILL INSTRUCTIONS

- If flammable gas alarms sound, immediately close valves on the appropriate cylinders by turning the valve atop the cylinder in a clockwise direction until it stops.
- If there has been a significant release of gases and/or alarms continue to sound after the valves atop the compressed gas cylinders are closed, immediately evacuate the laboratory. Inform building management and workers in neighboring laboratories. Take appropriate action according to the MSDS of the gas that has been released.

DESCRIPTION OF PROCEDURE:

- Start-Up
    1. Open GC hydrogen and air gas cylinders.
    2. Turn on heat tape between reactor outlet and GC inlet.
    3. Open lizmethodco2.mth in the GC software and wait for the status to read "ready."
    4. Open reactor carrier gas (nitrogen or carbon dioxide) cylinder and valves.
    5. Set reactor carrier gas flow rate at the mass flow controller.
    6. Plug in temperature controller and set temperature.
    7. Turn on UV lamp.
    8. Start appropriate sequence in GC software (lizsequence3.seq)

- Shut-down

    1. End sequence in GC software.
    2. Open valvebakeout.mth in GC software and wait for the status to read "ready."
    3. Turn off UV lamp.
    4. Unplug temperature controller.
    5. Turn off reactor carrier gas at the mass flow controller.
    6. Turn off reactor carrier gas at the valves and at the cylinder valve.
    7. Start valvebackout.mth in the GC software by pressing the "Start" button.
    8. After three minutes, close the GC hydrogen and air gas cylinders.

APPENDIX F

Calibration for the Varian CP-3800 Gas Chromatograph

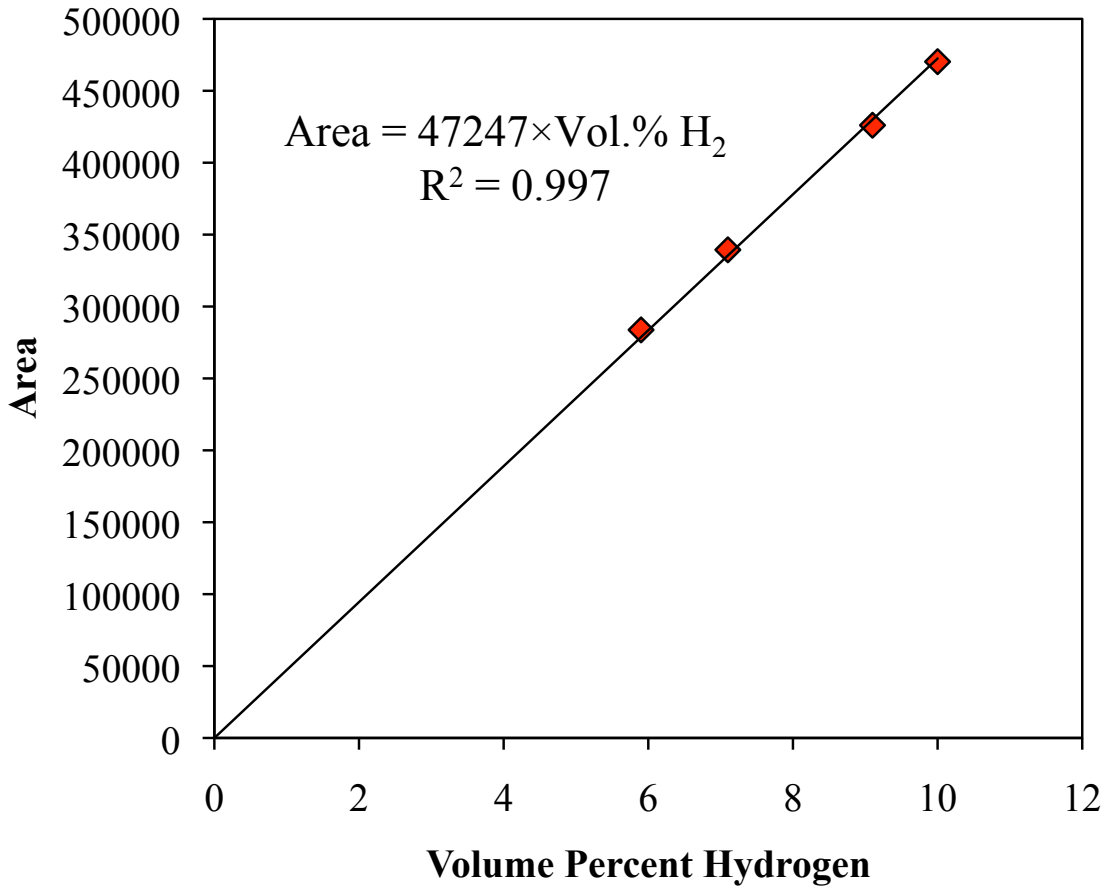

Calibration curve for hydrogen using the TCD.

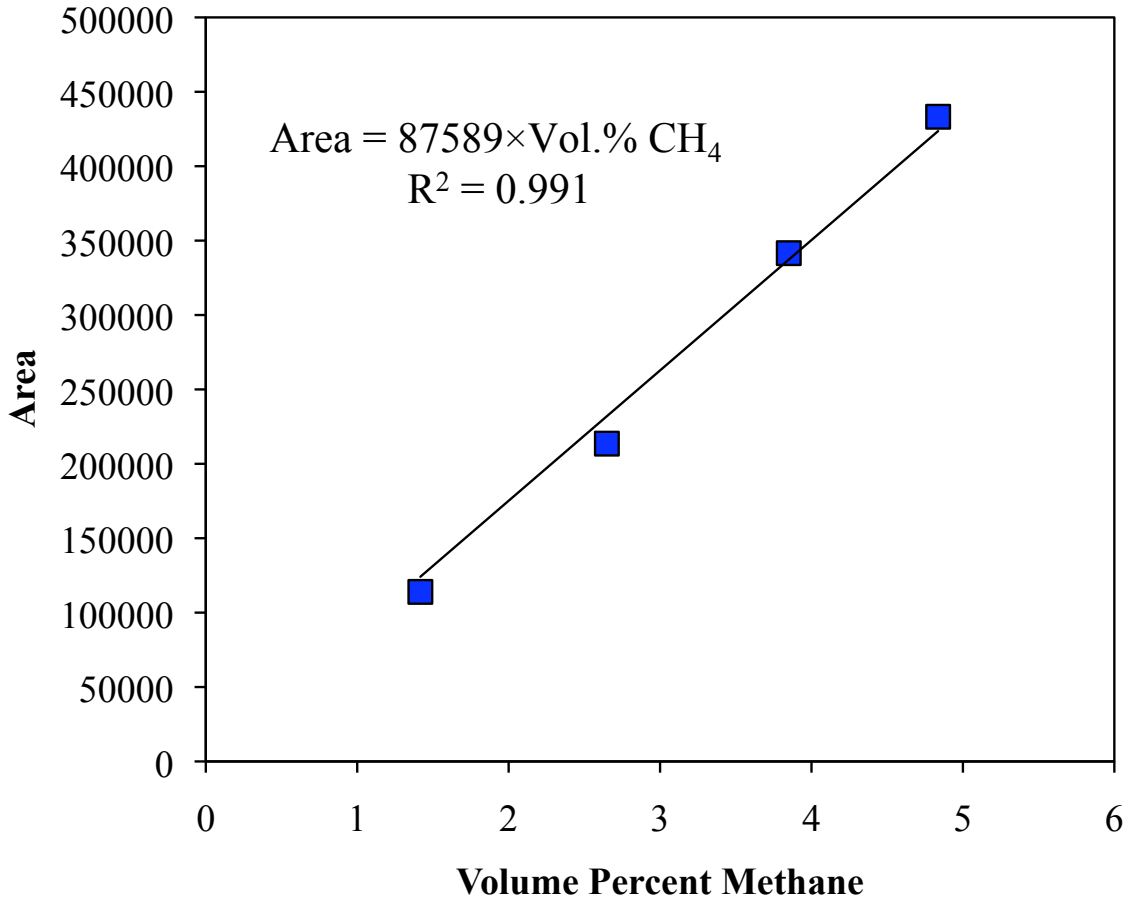

Calibration curve for methane using the FID.

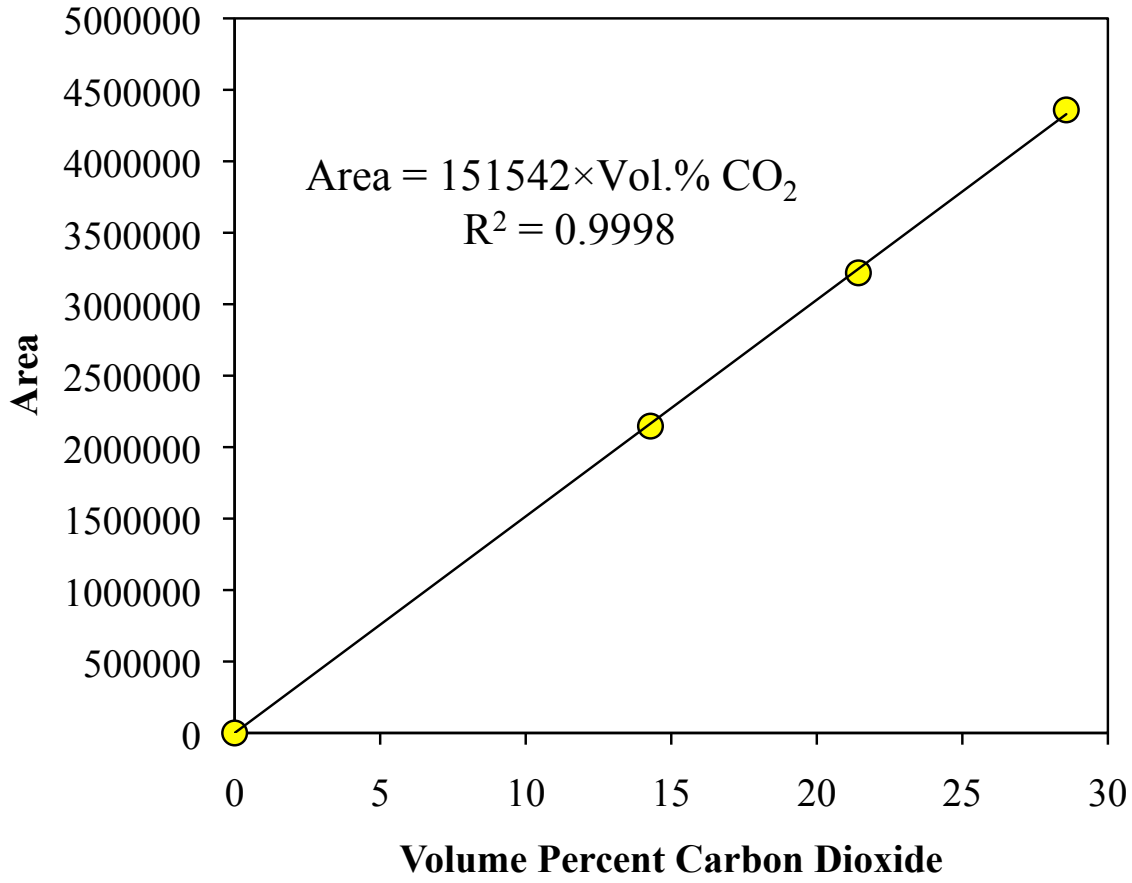

Calibration curve for carbon dioxide using the TCD.

APPENDIX G

GC Method for Measuring Sabatier and Water Splitting Reaction Products

Reaction products were introduced into the Varian CP-3800 gas chromatograph by three parallel ports. The first port analyzed gases using the "front" thermal conductivity detector (TCD) to detect carbon dioxide, carbon monoxide, and nitrogen and used a zero-grade helium carrier gas flowing at 1 mL/min at 19.6 psig. The second port analyzed gases using the "middle" TCD to detect hydrogen using a zero-grade argon carrier gas flowing at 60 mL/min at 35.0 psig. The third port detected methane using a "rear" flame ionization detector (FID) with a stoichiometric mixture of zero-grade hydrogen and zero-grade air flowing at 60 mL/min at 31.8 psig.

Method for Varian CP-3800:

Time	Valve 1	Valve 2	Valve 3	Valve 4	Valve 5	Valve 6	Valve 7
	Inject + Backflush to Vent	Series Bypass	Inject + Backflush to Vent	Gas Sampling	Sample	Sample	Sample
Initial	Fill + Backflush	Bypass	Fill + Backflush	Fill	ON	ON	ON
0.10	Fill + Backflush	Bypass	Fill + Backflush	Inject	ON	ON	ON
0.80	Fill + Backflush	Bypass	Fill + Backflush	Fill	ON	ON	ON
1.00	Inject	Bypass	Inject	Fill	ON	ON	ON
2.25	Inject	Bypass	Fill + Backflush	Fill	ON	ON	ON
7.50	Fill + Backflush	Bypass	Fill + Backflush	Fill	ON	ON	ON

Front Injector = 220°C

MIDDLE EFC:

Pressure (psi)	Rate (psi/min)	Hold (min)	Total (min)
35.0		0	0
35.0	2.00	23.5	23.5

Time	Total Flow
Initial	60 mL/min

REAR EFC:

Pressure (psi)	Rate (psi/min)	Hold (min)	Total (min)
31.8		0	0
31.8	2.00	23.5	23.5

Column Oven = 45°C, Hold = 12 minutes

DETECTOR

Front TCD: 200°C, Filament Temp = 200°C

Time	Range	Autozero	Polarity
Initial	0.5	Yes	Positive

Middle TCD: 201°C, Filament Temp = 280°C

Time	Range	Autozero	Polarity
Initial	0.5	Yes	Negative

Rear FID: 300°C

Time	Range	Autozero	Polarity
Initial	12	Yes	Positive

OUTPUT:

Port	Time	Signal Source	Attenuation
A	Initial	Front	1
B	Initial	Middle	1
C	Initial	Rear	1

DATA ACQUISITION:

Detector Bunch Rate = 4 points (10 Hz)

Noise Monitor Length = 64 bunched points (6.4 s)

FID/TCD Detector Full Scale

Front = 1V

Middle = 1V

Rear = 1000V

Front TCD:

Signal/Noise Ratio = 5

Peak Width = 45

Initial Tangent Height% = 10

Monitor Noise: Before every run

Measure: Peak area

Report unidentified peaks: yes

Middle TCD:

Signal/Noise Ratio = 15

Peak Width = 45

Initial Tangent Height% = 10

Monitor Noise: Fixed value = 15 μVolts

Measure: Peak area

Report unidentified peaks: yes

Rear FID:

Signal/Noise Ratio = 15

Peak Width = 45

Initial Tangent Height% = 10

Monitor Noise: Before every run

Measure: Peak area

Report unidentified peaks: yes